Longitudinal Modulational Instabilities

by

Ming Yu

Submitted in Partial Fulfillment
of the
Requirements for the Degree
Doctor of Philosophy

Supervised by
Professor Colin J. McKinstrie

Department of Mechanical Engineering
The College
School of Engineering and Applied Sciences

Reviewed for Classification 1/19/96
(Date)
UNCLASSIFIED
R. L. McCRORY, JR.
Authorized Derivative Classifier

University of Rochester

Rochester, New York

1996

Curriculum Vitae

The author was born on November 5, 1962, in Beijing, China. He attended Xiamen University, Xiamen, China, in 1980 and graduated with a Bachelor of Science degree in Physics in 1984. He continued his education at the Graduate School of University of Science and Technology of China and obtained a Master of Science degree in Physics in 1987. He then worked for the Institute of Physics of the Chinese Academy of Science for two years.

In September, 1989, he entered the graduate program in Mechanical Engineering at the University of Rochester and received Master of Science degrees in Mechanical Engineering and Optics in 1991 and 1994, respectively. His doctoral thesis was supervised by Professor Colin J. McKinstrie.

Thesis related publications

M. Yu, C. J. McKinstrie, and G. P. Agrawal, "Instability due to cross-phase modulation in the normal dispersion regime," *Phys. Rev. E* **48**, 2178 (1993).

M. Yu, C. J. McKinstrie, and G. P. Agrawal, "Modulational instabilities in dispersion-flattened fibers," *Phys. Rev. E* **52**, 1072 (1995).

M. Yu, G. P. Agrawal, and C. J. McKinstrie, "Pump-wave effects on the propagation of noisy signals in nonlinear dispersive media," *J. Opt. Soc. Am. B* **12**, 1126 (1995).

M. Yu, G. P. Agrawal, and C. J. McKinstrie, "Effect of residual dispersion in the phase-conjugation fiber on dispersion compensation in optical communication systems," *IEEE Photon. Tech. Lett.* **7**, 932 (1995).

S. B. Cavalcanti, G. P. Agrawal, and M. Yu, "Noise amplification in dispersive nonlinear media," *Phys. Rev. A* **51**, 4086 (1995).

M. Yu and C. J. McKinstrie, "Impulse-response of a nonlinear dispersive wave," *Phys. Rev. E* **52**, 6826 (1995).

M. Yu, C. J. McKinstrie, and G. P. Agrawal, "Temporal modulational instabilities of counterpropagating waves in a finite dispersive Kerr medium, Part I: Theoretical model and analysis," submitted to *J. Opt. Soc. Am. B*.

M. Yu, C. J. McKinstrie, and G. P. Agrawal, "Temporal modulational instabilities of counterpropagating waves in a finite dispersive Kerr medium. Part II: Application to Fabry-Perot cavities," submitted to *J. Opt. Soc. Am. B*.

Acknowledgments

The author wishes to express his sincere gratitude to his thesis advisor, Professor Colin J. McKinstrie for his support, encouragement and advice throughout the course of this research. He also would like to make special thanks to Professor Govind P. Agrawal, who has continuously shared his expertise and provided insightful guidance on every aspect of this thesis. The author greatly appreciates the help and friendship of his colleagues Gregory Luther, Jingsong Li, Rodolfo Giacone, Liyue Mu, Lily Zheng, Xiangdong Cao and Zhong Ding in the Mechanical Engineering Department, and Lisa Liou, Cliff Headley, Takayuki Yoshino, Andrew Ryan, John Marciante, Stojan Radic, Sujatha Ramanujan and and Zhengwu Li in the Institute of Optics. For the understanding and enduring support of his parents, he is deeply grateful. Finally, the author would like to thank Hongyu Meng for her friendship.

This work was supported by the National Science Foundation under Contract No. PHY-9057093, the U. S. Department of Energy (DOE) Office of Inertial Confinement Fusion under Cooperative Agreement No. DE-FC03-92SF19460, the University of Rochester, and the New York State Energy Research and Development Authority. The support of DOE does not constitute an endorsement by DOE of the views expressed in this thesis.

Abstract

This thesis is a report on several aspects of the modulational instability of a wave propagating in a nonlinear dispersive medium.

An impulse-response analysis is performed analytically to study the spatiotemporal instability of a nonlinear dispersive wave. The asymptotic Green function is obtained for both modulationally stable and unstable cases. The conditions for absolute and convective instability are found, as are the frequency region for amplification, and the spatial and temporal growth rates.

The nonlinear Schrödinger equation does not describe fast modulations adequately because it is based on a Taylor expansion in the frequency domain. Here, harmonic analysis is used to study the effects of the entire modal dispersion curve and the frequency dependence of the nonlinear coefficients on the properties of modulational instabilities. New regions of instability for dispersion-flattened fibers are found and characterized by this approach.

The interaction of two light waves, having different frequencies and propagating in a dispersive nonlinear medium, is studied using the method of Zakharov [Sov. Phys. JETP **24**, 740 (1967)]. It is shown that cross-phase modulation does not necessarily lead to instability of the incident waves. Different configurations leading to instabilities are discussed.

A comprehensive analytical study of temporal modulational instabilities in a finite nonlinear dispersive medium is presented. The use of a perturbation method results in the physically transparent model of a doubly-resonant optical parametric oscillator that allows simplification and characterization of the complicated system in familiar language. The general results can be interpreted by using an analogy to a detuned distributed-feedback structure. The effects of boundary reflections and dispersion are shown to be important.

Stochastic aspects of nonlinear dispersive wave are also investigated. For small-amplitude noise, stochastic field propagation in nonlinear dispersive media is studied analytically in the undepleted-pump approximation. Power spectrum and relative-intensity-noise spectrum is obtained. A statistical description of modulational instability is given in the anomalous dispersion regime. For large-amplitude noise, the spectral transformation of stationary noise (Gaussian and diffusing-phase processes at the input) going through a nonlinear dispersive medium is studied numerically. The results indicate different power-spectrum evolutions depending on the sign of the dispersion coefficients and the kind of stochastic processes.

Contents

Curriculum Vitae ii

Acknowledgments iv

Abstract v

Table of Contents vii

List of Figures x

1 Introduction 1

1.1 Introduction 1

1.2 Physical mechanism 2

1.3 Overview 9

1.3.1 Impulse response of a nonlinear dispersive wave 9

1.3.2 Broadband modulational instabilities 10

1.3.3 Effects of a copropagating wave 11

1.3.4 Effects of a counterpropagating pump wave and a finite medium 13

1.3.5 Effects of incoherence 14

2 Impulse-Response of a Nonlinear Dispersive Wave 16

2.1 Introduction 16

2.2 Impulse response 17

2.3 Time-asymptotic pulse evolution 19

2.4 Spatial amplification 27

2.5 Conclusions 34

3 Modulational Instabilities in Dispersion-Flattened Fibers 36

3.1 Introduction 36

3.2 Harmonic analysis 37

3.3 Dispersion-flattened fiber 47

3.3.1 $\beta_{2e} < 0$ case 47

3.3.2 $\beta_{2e} > 0$ case 53

3.3.3 Frequency-dependent nonlinearity 58

3.4 Conclusions 61

4 Instability from Cross-Phase Modulation in the Normal Dispersion Region 64

4.1 Introduction 64

4.2 Harmonic analysis 66

4.3 Results and discussion 72

4.4 Conclusions 87

4.5 Appendix: Unequal pump-wave powers 88

5 Modulational Instabilities of Counterpropagating Waves in a Finite Dispersive Kerr Medium 90

5.1 Introduction 90

5.2 General solution 93

5.3 Boundary reflections 104

5.4 Weakly reflecting and anti-reflecting boundaries 107

5.5 Strongly reflecting boundaries 114

5.6 Probe transmissivity and reflectivity 121

5.7 Conclusions 126

6 Incoherence Aspects of Nonlinear Dispersive Waves **129**

6.1 Introduction 129

6.2 Pump-wave effects on the propagation of noisy signals in nonlinear dispersive media 132

6.2.1 Noise propagation 132

6.2.2 Power spectrum of the field 134

6.2.3 Relative intensity noise 138

6.2.4 Noise-induced four-wave mixing 143

6.3 Spectral evolution of large-amplitude noise 147

6.3.1 Classification of the parameter regions 148

6.3.2 Numerical simulation and discussion 151

6.4 Conclusions 156

Bibliography **159**

List of Figures

1-1 Schematic illustration of temporal modulational instability. 4

1-2 Wavelet trajectories for the development of an intensity perturbation. 5

1-3 Four-wave mixing picture of modulational instability. 7

1-4 Temporal growth rate of modulational instability versus wave number. 8

2-1 The asymptotic Green function for the modulationally stable system. 23

2-2 The real and imaginary part of the exponential factor $s(v)$ from the saddle point integration. 26

2-3 The asymptotic Green function for the modulationally unstable system. 27

2-4 Complex-plane picture of the four branches of the dispersion relation for modulational instability. 30

2-5 The spatial growth rate and corresponding wavenumber versus modulational frequency. 31

2-6 The amplification frequency range, the maximum spatial growth rate and corresponding frequency versus group velocity. 32

3-1 Instability analysis by the diagram of wavenumber mismatch. . . . 46

3-2 Group-velocity dispersion versus frequency for a dispersion-flattened fiber. 48

3-3 Instability analysis for a dispersion-flattened fiber with $\beta_{2e} < 0$. . 49

3-4 Contour plot of growth rate of modulational instability for a dispersion-flattened fiber with $\beta_{2e} < 0$. 52

3-5 Peak growth rate of instability versus pump power. 54

3-6 Growth rate versus frequency at different pump powers for a dispersion-flattened fiber with $\beta_{2e} < 0$. 55

3-7 Instability analysis for a dispersion-flattened fiber with $\beta_{2e} > 0$. . 56

3-8 Contour plot of growth rate of modulational instability for a dispersion-flattened fiber with $\beta_{2e} > 0$. 57

3-9 Growth rate versus frequency at different pump powers for a dispersion-flattened fiber with $\beta_{2e} > 0$. 58

3-10 Raman effect on the instability growth rate. 61

3-11 Raman effect on the amplitude ratio of the anti-Stokes and Stokes waves for the unstable mode. 62

4-1 Fourier spectrum of the electric field in four-sideband coupling. . . 70

4-2 Pump wave positions on the dispersion curve of a conventional fiber. 73

4-3 Spatial growth rate at different values of group-velocity dispersion plotted as a function of the modulational frequency for the case in which one pump frequency is in the normal dispersion regime and the other pump frequency is in the anomalous dispersion regime. . 76

4-4 Illustration of the wavenumber matching condition. 78

4-5 Spatial growth rate at different pump power ratios plotted as a function of the modulational frequency for the case in which one pump frequency is in the normal dispersion regime and the other pump frequency is in the anomalous dispersion regime. 81

4-6 Pump wave positions on the dispersion curve of a dispersion-flattened fiber. 83

4-7 Spatial growth rate plotted as a function of the modulational frequency for the case in which the two pump frequencies are in separate normal dispersion regimes and the pump-wave group velocities are equal. 84

4-8 Spatial growth rate plotted as a function of the modulational frequency for the case in which the two pump frequencies are in separate normal dispersion regimes and the pump-wave group velocities are unequal. 86

5-1 Schematic illustration of counterpropagating pump waves in a finite dispersive Kerr medium. 93

5-2 Temporal growth rate versus frequency for antireflection boundaries. 111

5-3 Threshold instability condition for antireflection boundaries. . . . 112

5-4 Temporal growth rate and threshold condition for weakly reflecting boundaries. 113

5-5 Temporal growth rate versus frequency for anomalous dispersion and strong boundary reflections. 117

5-6 Temporal growth rate versus frequency for normal dispersion and strong boundary reflections. 120

5-7 Frequency response of a nonlinear dispersive Fabry-Perot cavity. . 125

6-1 Analytical result for spectral evolution in the normal dispersion region for a symmetric input spectrum. 136

6-2 Analytical result for spectral evolution in the anomalous dispersion region for a symmetric input spectrum. 136

6-3 Numerical simulations of spectral evolution in the normal dispersion region for a symmetric input spectrum. 139

6-4 Numerical simulations of spectral evolution in the anomalous dispersion region for a symmetric input spectrum. 139

6-5 Analytical result for the relative-intensity-noise spectrum evolution in the normal dispersion region for a symmetric input spectrum. . 141

6-6 Analytical result for the relative-intensity-noise spectrum evolution in the anomalous dispersion region for a symmetric input spectrum. 141

6-7 Numerical simulations of relative-intensity-noise spectrum evolution in the normal dispersion region for a symmetric input spectrum. 142

6-8 Numerical simulations of relative-intensity-noise spectrum evolution in the anomalous dispersion region for a symmetric input spectrum. 142

6-9 Spectral evolution in the normal dispersion region for an asymmetric input spectrum. 145

6-10 Spectral evolution in the anomalous dispersion region for an asymmetric input spectrum. 146

6-11 Spectral evolutions over 6 nonlinear lengths for two Gaussian processes with different input bandwidths. The dispersion is normal. 153

6-12 Spectral evolutions over 6 nonlinear lengths for two Gaussian processes with different input bandwidths. The dispersion is anomalous. 153

6-13 Spectral evolutions over 6 nonlinear lengths for two diffusing-phase processes with different bandwidths at the input. The dispersion is normal. 155

6-14 Spectral evolutions over 6 nonlinear lengths for two diffusing-phase processes with different bandwidths at the input. The dispersion is anomalous. 155

Chapter 1

Introduction

1.1 Introduction

Modulational instability (MI) is one of the most fundamental phenomena in the physics of nonlinear wave propagation. In the presence of MI, a nonlinear continuous wave (CW) is not a stable state of the system (in contrast to the case of a linear wave). Due to the combined action of group velocity dispersion (or diffraction) and the intensity dependence of the refractive index, any small perturbation of the CW state will grow exponentially.

Because of their fundamental nature, MI's have played a prominent role in diverse areas of scientific research since their discovery more than twenty years ago.[1-9] In particular, the advent of lasers gave them practical importance because most media cannot be viewed as linear in regard to the propagation of large-amplitude electromagnetic (EM) waves. Naturally, MI's are of great concern in most branches of nonlinear optics.[10-12]

For example, in laser fusion, the nonlinear medium is a plasma. MI tends to destroy the uniformity of the laser light that is required for efficient compression of the nuclear fuel.[10] In optical phase conjugation,[13,14] uniform reference waves are also required for a high-quality conjugate wave to be generated by four-wave mixing (FWM). MI-induced nonuniformity is thus a limiting factor. In fiber-optical communication systems,[15] MI amplifies noise and increases the bit error rate.[16,17]

On the other hand, MI can be utilized to one's advantage. In fact, it has been applied to optical switching,[18,19] short pulse generation[20,21] and parametric amplification[12] and oscillation[22-25] in optical-fiber based systems. Of particular interest is the connection between MI and the formation of optical solitons[26] in a fiber. Because of their robust nature, these solitons can be used as the natural bits in high-speed long-distance communication.

In the following analyses, focus is made on cases in which a one-dimensional (1D) model is adequate and various aspects of longitudinal or temporal MI's are studied. Although optical fibers is often used for reference, the analyses are also relevant to the other areas of research mentioned above.

1.2 Physical mechanism

As an example of how this kind of instability can happen, consider the simple 1D problem of a single CW wave propagating in an instantaneous Kerr medium. In such a medium, the nonlinearity causes the dispersion relation to depend on the wave intensity. In the nonlinear geometrical optics approximation,[27,28] one can write the field as $A(t, z) \exp[i\theta(t, z)]$, where the scale of change in θ is much faster than in A, and in the local wave number $k \equiv \partial_z \theta$ and frequency $\omega \equiv -\partial_t \theta$. In this scheme, the first-order approximation gives $-\partial_t \theta = \omega(\partial_z \theta, |A|^2)$, which is identified as the local nonlinear dispersion relation in a Kerr medium. The second-order approximation gives the conservation of action which is proportional to $|A|^2$. For weak nonlinearity, the first equation can be written (after taking derivatives with respect to z on both sides and considering $|A|^2$ a small quantity) as

$$\partial_t k + v_g(k)\partial_z k = -\lambda(k)\partial_z|A|^2 \tag{1.1}$$

and the second can be written as

$$\partial_t|A|^2 + \partial_z(v_g(k)|A|^2) = 0. \tag{1.2}$$

In these equations, $v_g = \partial\omega/\partial k$ and $\lambda(k) = -\partial\omega/\partial|A|^2$. Both derivatives are evaluated at $|A|^2 = 0$. The first equation indicates that, in linear regime, each group of wavelets with a certain wave number convects at its group velocity, as is well known. The nonlinear effect modifies the wave number as the group propagates. The second equation is the conventional form of a conservation equation indicating that energy convects with the local group velocity.

The initial conditions corresponding to a plane wave are $k(0,z) = k_0$ and $|A(0,z)|^2 = |A_0|^2$, for which the constant solutions are $k(t,z) = k_0$ and $|A(t,z)|^2 = |A_0|^2$. Now consider a small amplitude perturbation to this equilibrium, i.e. small humps in intensity $I = |A|^2$ in the initial condition [Fig. 1-1 (a)].

It follows from Eq. (1.1) that instead of being constant, k is now a decreasing function of time in the front half of each hump and is an increasing function of time in the rear half of each hump, when λ is positive. If v_g is an increasing function of k, then, from Eq. (1.2), the front half of each hump is retarded while the rear half of each hump is advanced. Wave energy accumulates at the center of each hump and the perturbation grows as it convects [Fig. 1-1 (b)]. Conversely, if v_g is

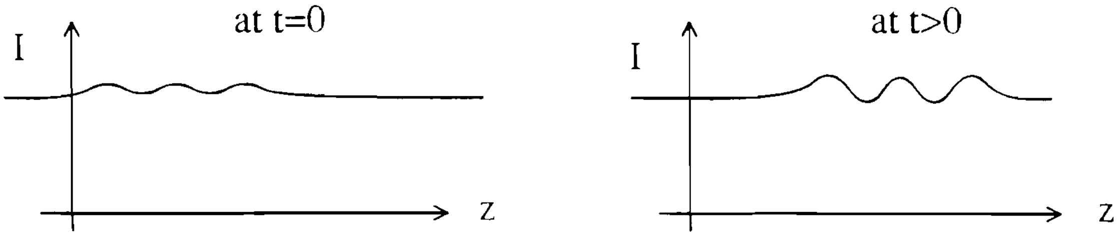

Figure 1-1: Schematic illustration of the temporal growth of an intensity perturbation

a decreasing function of k. then the front half of each hump is advanced while the rear half of each hump is retarded. Wave energy spreads outward from the center of each hump and the perturbation decreases. Thus the plane-wave equilibria are modulationally unstable if λ is positive and v_g is an increasing function of k or, alternately, if λ is negative and v_g is a decreasing function of k. Figure 1-2 illustrates representative wavelet trajectories and the resulting changes in the hump intensity for the case of linear medium, and the cases of modulationally stable and unstable nonlinear systems.

The nonlinear geometrical-optics model described above does not consider the effects of dispersion in their entirety. Specifically, it neglects the part similar to diffraction in physical optics that spreads the humps to prevent energy getting too concentrated and, hence, tends to stabilize the process. In fact, MI's generally disappear for relatively fast modulations, as indicated by the more accurate model described below. In the 1D case, the compression process is eventually counterbalanced by this dispersive spreading effect on the steepened humps.

From the preceding argument. one can see a fundamental aspect of nonlinear dispersive wave propagation, that is the interplay between dispersion and the Kerr nonlinearity. MI is closely related to soliton physics. It is well known that a single

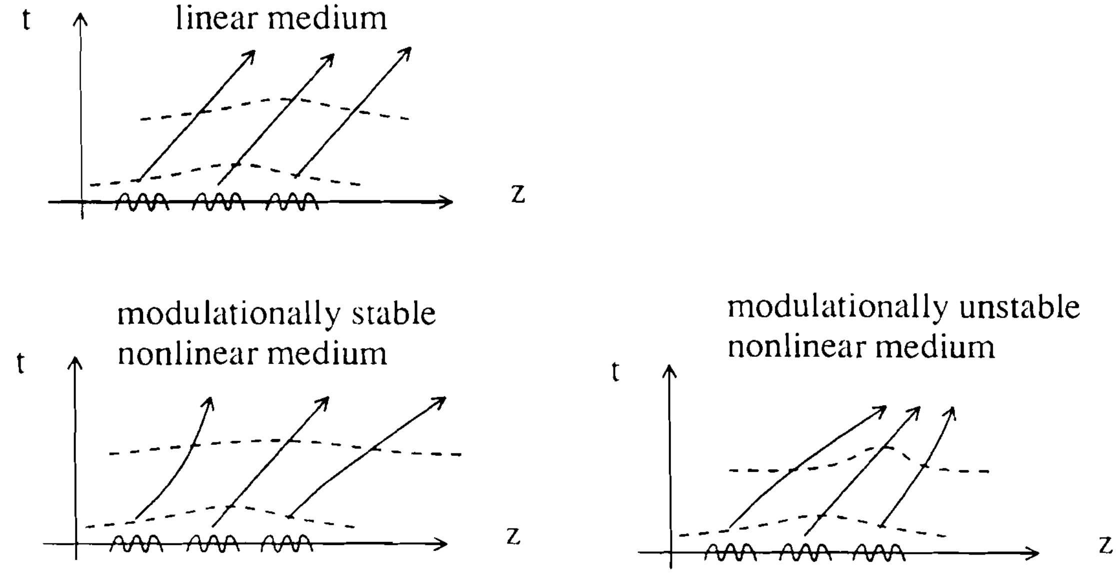

Figure 1-2: Wavelet trajectories and the development of an intensity perturbation in three kinds of media

pulse will eventually spread out during propagation due to the existence of dispersion. However, under certain conditions the novel balancing mechanism discussed above can lead to the formation of nonspreading pulses called solitons which are robust enough to survive collisions with other solitons of different speeds. Solitons are used as the natural bits of infomation for high-speed optical communications.

A quantitative study of MI's can be carried out within the framework of a nonlinear Schrodinger equation (NSE) for the slowly-varying wave amplitude. Such an equation takes both dispersion and nonlinearity into consideration. It is appropriate for a wide variety of dispersive, weakly nonlinear waves. When the wave motion can be described by a narrow range of wavenumbers and small intensity, it can be intuitively obtained by Taylor expanding the dispersion relation $\omega(k, |A|^2)$

as

$$\omega = \omega_0 + (\partial\omega/\partial k)_0(k-k_0) + (\partial^2\omega/\partial k^2)_0(k-k_0)^2/2 + (\partial\omega/\partial|A|^2)_0|A|^2, \tag{1.3}$$

where the derivatives of ω are evaluated at the central, or carrier, wave number k_0 and zero wave amplitude. Every factor of $\omega - \omega_0$ in the above equation must have originated as a term $i\partial_t$ in the differential equation from which it was obtained and, likewise, every factor of $k - k_0$ must have originated as a term $-i\partial_z$. By making these substitutions in the Taylor expansion of ω, one obtains the NSE

$$[i(\partial_t + v_g\partial_z) + \mu\partial^2_{zz} + \lambda|A|^2]A = 0, \tag{1.4}$$

where $v_g = (\partial\omega/\partial k)_0$, $\mu = (\partial^2\omega/\partial k^2)_0/2$, and $\lambda = -(\partial\omega/\partial|A|^2)_0$.

A plane-wave solution of this equation is $A_s = A_0\exp(i\lambda|A_0|^2t)$. Small perturbations of this equilibrium can be cast in the form $\delta A\exp(i\lambda|A_0|^2t)$. By linearizing Eq. (1.4) around this equilibrium, one finds that

$$[i(\partial_t + v_g\partial_z) + \mu\partial^2_{zz} + \lambda|A_0|^2]\delta A + \lambda A_0^2\delta A^* = 0. \tag{1.5}$$

The general eigensolution to this equation in an infinite medium is of the form $\delta A(t,z) = \delta A_+(t,k)\exp(ikz) + \delta A_-(t,k)\exp(-ikz)$, where k is real and the amplitude perturbations $\delta A_\pm$ satisfy the coupled-mode equations

$$\begin{aligned}
[id_t - v_gk - \mu k^2 + \lambda|A_0|^2]\delta A_+ &= -\lambda A_0^2\delta A_-^*,\\
[-id_t + v_gk - \mu k^2 + \lambda|A_0|^2]\delta A_-^* &= -\lambda A_0^{*2}\delta A_+.
\end{aligned} \tag{1.6}$$

By comparing Eq. (1.6) to the familiar equations governing FWM,[11,12] one has the following picture: Eqs. (1.6) describe the linearized stage of the induced decay of the carrier wave at k_0 into its daughter waves, or sidebands, at $k_0 \pm k$ (Fig. 1-3). The right sides of the equations represent the harmonic driving from the nonlinear beating of the carrier and one of the daughter waves, producing the mode coupling with coefficient λA_0^2, and the left sides describe wave propagation in the presence of the linear and nonlinear frequency mismatches $(-\mu k^2 + \lambda |A_0|^2)$. Alternatively, Eqs. (1.6) describe the scattering of the pump into one of the sidebands by the nonlinear grating produced by the pump and the other sideband. These FWM equations can be obtained without using a NSE by making a harmonic analysis of weakly-nonlinear wave propagation in a Kerr medium and by making a parabolic approximation of the linear dispersion relation. One of the differences between the modulational and ordinary FWM instabilities is that the frequency mismatch of a MI depends on the square of the wave number mismatch (a slower dependence) whereas it is proportional to the wave number mismatch (a faster dependence) in ordinary FWM.[11,12]

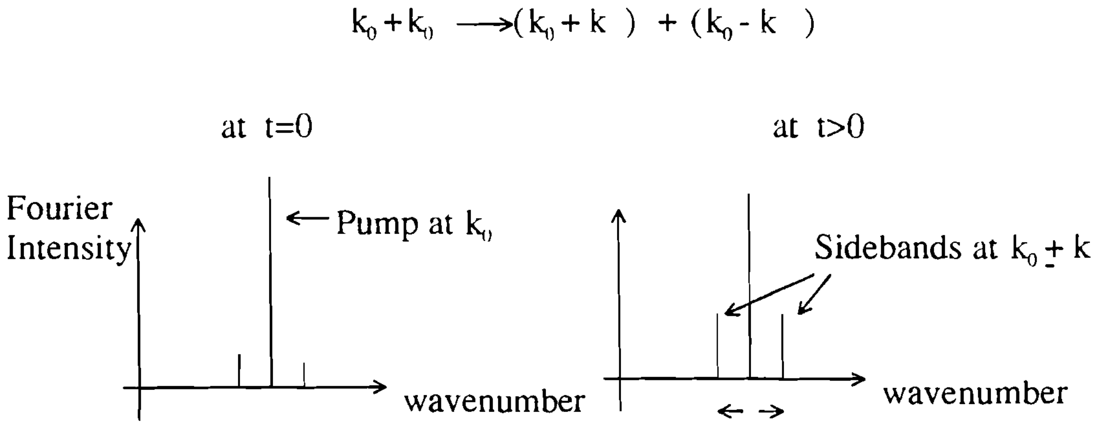

Figure 1-3: The picture of MI in wavenumber domain is FWM. The large Fourier peaks represent the pump wave, whereas the small peaks represent the sidebands

It is a straightforward matter to solve Eqs. (1.6). By setting $\delta A_{+}(t) =$

$\delta B_+ \exp(-i\omega t)$ and $\delta A_-(t) = \delta B_- \exp(i\omega^* t)$, where $\delta B_\pm$ are constants. One obtains the complex dispersion relation

$$\omega_\pm(k) = v_g k \pm \sqrt{\mu^2 k^4 - 2\mu\lambda|A_0|^2 k^2}. \tag{1.7}$$

Thus, whenever the product $\lambda\mu$ is positive, the plane-wave equalibrium is unstable, in agreement with the preceding qualitative discussion of modulational physics. The frequency mismatch determines the range of unstable wave numbers as $k_{mi} = \pm\sqrt{2\lambda|A_0|^2/\mu}$. This range is much wider than that of ordinary FWM (which is proportional to the square of the small wave amplitude). The peak temporal growth rate is $[Im(\omega)]_{max} = \lambda|A_0|^2$, corresponding to the optimal wave number $k_{opt} = \pm\sqrt{\lambda|A_0|^2/\mu}$. From the discussion after Eq. (1.6), it is easy to see that the peak growth corresponds to exactly resonant nonlinear beating or scattering where the sum of the linear and nonlinear frequency mismatches is zero. As the wave number increases, the vanishing of the instability can be viewed either as the stabilizing effects of dispersive-spreading, as discussed previously, or frequency mismatch in the FWM picture. Figure 1-4 shows the MI growth rate $\mathrm{Im}(\omega_-)$ at varying wave number.

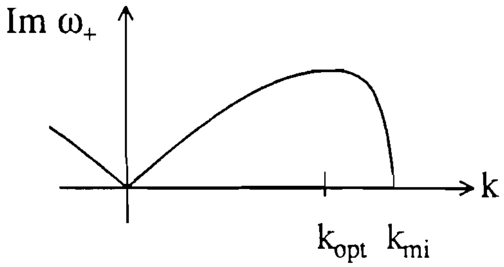

Figure 1-4: Temporal MI growth rate as a function of wave number

1.3 Overview

This thesis is an extension of the classical treatment of 1D MI discussed above. It reports new research results for the longitudinal, or temporal, MI ranging from such fundamental aspects as an inpulse response study, to the statistical aspects of MI, and to the complications associated with a dispersion-flattened fiber, the coexistence of two waves, and a finite medium. A short overview for each of the following chapters is provided below.

1.3.1 Impulse response of a nonlinear dispersive wave

The general solution for the perturbative field of a nonlinear CW pump wave is a linear superposition of the eigensolutions discussed in Chapter 1. This means the result from the wave number domain analysis cannot be used directly to get a physical picture in the spatial-temporal domain. For such a purpose, it is desirable to find the Green function, that is, the solution corresponding to a point initial disturbance at the origin. This is especially important if the initial perturbation contains many spatial frequencies (i.e. a localized initial perturbation). Normally, the asymptotic behavior of the Green function at large t will provide enough information to classify the instability as convective or absolute, and to the differentiate between evanescence and amplification. Due to its importance, this kind of impulse response analysis has been performed for nearly every instability found in plasmas and fluids. The routine procedure consists of studying the system responses to point-source perturbations in the form of an impulse and in the form of a sinosoidal oscillation in time.[29–32] However, the analysis is only done partially and numerically in the case of MI due to the complexity of the problem.[9]

Chapter 2 completes the impulse-reponse analysis analyically,[33] and gives simple expressions for the pulse shape due to an impulse perturbation, and, in the case of convective instability, for the unstable frequency range and the spatial growth rate. The analysis is extended to a modulationally stable nonlinear dispersive system. It is found that the response to an impulse perturbation does not disperse away as it does in a linear dispersive system. The time-asymptotic behavior of the perturbation is characterized. As will be shown in this chapter, the MI of an optical wave is almost always convective in an infinite medium. Henceforth the terms MI, amplification, and spatial growth will be used interchangebly when no confusion is likely to arise.

1.3.2 Broadband modulational instabilities

The spatial growth of a MI is usually studied using the local properties of the modal dispersion relation, such as second-order dispersion (as in the NSE), third-order dispersion and so on, resulting from the Taylor expansion of the dispersion relation $k(\omega, |A_0|^2)$.[34,35,37] However, for wide bandwidth or fast MI, the second-, third- and higher-order dispersion effects are all comparable: the Taylor expansion scheme breaks down and nonlocal properties of the dispersion curve have to be considered. Furthermore, the frequency dependence of the nonlinear coefficients due to the Raman or nonlinear-relaxation effects could become important. The usual approach can give erroneous information about the instability for fast modulations (for example, in the case of relatively large input power or relatively small dispersion).

MI at relatively fast modulational speeds is important because it is intrinsically related to the formation of ultrashort optical pulses. In Chapter 3, harmonic analysis is used to study MI. This formalism applies to broad-bandwidth perturbations and automatically includes the Raman and nonlinear-relaxation effects. To summarize the major results:[39] A simple expression for the gain curve of MI has been derived, which depends on the entire dispersion curve and includes the frequency dependence of the $\chi^{(3)}$ coefficients, so it is valid for high-frequency modulations. It is used to study propagation in a dispersion-flattened fiber,[40] whose second-order dispersion coefficient changes sign twice as the carrier frequency is varied. Rich behaviors of the MI gain curve are found as the fiber parameters, input power and pump frequency are changed, and simple expressions are given to characterize these behaviors. For example, a new kind of MI is found when the pump is in the normal dispersion regime, whereas no MI exists for ordinary fibers. Its relation to the conventional MI and FWM is discussed both mathematically and physically. In the anomalous dispersion regime, MI is also different from the conventional instability. At low input power, it is a mix of the conventional MI and FWM. At high power, these instabilities merge and the growth rate is greatly reduced from the conventional prediction for both MI and FWM individually. Optical communication systems employing dispersion flattened fibers are likely to be affected by this new instability in some parameter regions.

1.3.3 Effects of a copropagating wave

The analysis of the MI of a single wave can be generalized to the MI of two copropagating waves.[9,41] The dispersion relation for each wave is affected by the intensities of both waves, a phenomenon called cross-phase modulation. This situation is usually studied using a pair of coupled NSE's. The FWM interaction can involve as many as four sidebands, two for each wave. It is necessary to fully understand the process due to its importance in multichannel communication systems.[15]

Previous analyses of this interaction have identified some cases in which both pumps can be modulationally unstable, even when one or both of them are stable by themselves.[9,41,42] The overall picture of the two-pump case still needs further investigation, in part because several experimental parameters may lie outside the region of validity of the previous analyses based on coupled NSE's, which required small modulational bandwidth and neglected the FWM interference of the two waves. The coupled NSE model has generated controversial predictions about the existence of MI in the normal dispersion region of an optical fiber.[43–45]

In Chapter 4, harmonic analysis based on Zakharov equation[46] is used to study the MI of copropagating waves.[48] This approach is valid for arbitrary bandwidth and takes the FWM effect into account. The coupled-mode equations for the four sidebands are obtained and the dispersion relation is, of course, dependent on the whole dispersion curve. In the normal dispersion region, stability is predicted for two copropagating waves of different frequencies in a ordinary single-mode fiber, in opposition to the prediction of coupled NSE's. In other media (for example, a dispersion-flattened fiber whose dispersion curve has two regions in which dispersion is normal, separated by a region in which dispersion is anomalous), in which the group velocity difference can be made small (even zero) without causing the FWM interference of the pumps, an instability will occur that changes from a two-sideband FWM instability to a four-sideband MI as the pump power increases or the group-velocity difference decreases. Cross-phase induced modulational instability can thus occur in a dispersion-flattened fiber when the two light waves propagate in different normal-dispersion regimes. An associated question concerns the coupling between sidebands of the two pumps. The conditions for efficient coupling were studied. No such coupling was predicted for waves of two frequencies in an ordinary single-mode fiber, in either the normal or the anomalous region. A sufficient condition for such coupling is that the group velocity difference between the two pumps can be made very small without causing the FWM interference of the pumps.

1.3.4 Effects of a counterpropagating pump wave and a finite medium

Physically, there are two competing effects that determine the stability of a finite system. The first is the tendency of the amplified perturbation to convect out of the system. The second is for it to feed back into the system by reflecting from the boundary or by scattering from a counterpropagating wave. Two counterpropagating light waves in a dispersive Kerr medium, with various boundary reflection conditions, are often encountered in nonlinear optics. The self-pulsing behavior of this kind of system is important for both active optical components, because it provides a mechanism for mode-locking, and passive components, because it limits the functioning of dispersive bistable devices as well as FWM.

Previous works have studied numerically the special case of two identical counterpropagating waves in a nonlinear dispersive medium with antireflecting boundaries.[49,50] In Chapter 5, the general system is studied analytically.[51,52] The results indicate that self-oscillation is sustained under conditions where the gain is provided by the individual MI's of each wave and the feedback is provided by reflections from the boundary or by scattering from the counterpropagating pump wave. In other words, the convective MI becomes absolute. Simple expressions are given for characterics of modulational self-oscillations such as the threshold condition, the maximal growth rate and the oscillation frequency in most parameter regimes.

The dependence of the self-pulsing behavior on such parameters as the powers, frequencies and phases of the counterpropagating light waves and the boundary reflection coefficient are explored. Simple physical pictures are presented to explain the formulas. For example, the case of an anti-reflection boundary is somewhat like what happens in an improperly designed distributed-feedback laser,[53] where the Bragg frequency is detuned from the gain peak by a relatively large amount, only in this case one has to consider coupled sidebands, and the feedback and phase-matching are provided automatically. The addition of boundary reflections enhances the feedback but the relative phase (which is adjustable) of the two light waves has an effect on the oscillation behavior in some parameter regimes.

1.3.5 Effects of incoherence

In many situations, the small input is not an ordinary function of time, but falls into the category of a stochastic process. Thus a statistical theory for the MI is needed. Such a theory is developed in Chapter 6. The analysis is straightforward because the governing equation is linear and stationary.[54] Simple expressions are given for the output power spectrum and relative-intensity-noise spectrum. As a bonus, when these results are applied to the normal dispersion case (without MI), they show that fringes in the spectra form due to the nonlinear dispersive effects.

Chapter 6 also contains a discussion of the effect of the finite linewidth of pump wave on the MI.[55] In spectral space MI can be pictured as follows: the overall spectrum at the input end can be decomposed into a δ function from the pump plus a small component from the input or noise. The small component gets amplified as if it passed through an amplifier of certain bandwidth (of the order of MI bandwidth ω_{mi}, which is proportional to the square root of input power).

Without the small component at the input, the spectrum keeps the delta function shape as it propagates. A frequently asked question is how the incoherence of the pump (ie. a non-δ spectrum) affects the MI (or whether noise amplification by MI can be suppressed by introducing finite bandwidth to the pump). One can deduce that if the pump bandwidth is much smaller than the MI bandwidth, the spectral picture of MI described above still holds qualitatively However, it is deduced that if the pump bandwidth is of the order of the MI bandwidth, the spectrum will evolve qualitatively the same with or without the small noise perturbation. This is understandable because the incoherence within the pump is actually no different from the noise, except that it is so big that the noise is insignificant. The evolution of the incoherent pump by itself is nonlinear and dispersive. In other words, it is like the propagation of pure stationary noise in a nonlinear dispersive medium. In this case, MI supression by pump incoherence is out of the question. Thus the existing theory[58] based on the perturbation of a steady-state stochastic process is not self-consistent. But in any case, it still makes sense to study the spatial evolution of the total spectrum, which is just one of the challenging tasks of understanding the nonlinear propagation of a stochastic signal.[56,57] Although theories have been developed,[58,59] neither is suitable for this case. The preliminary results from our numerical simulation have been able to give a quantitative description.

Chapter 2

Impulse-Response of a Nonlinear Dispersive Wave

2.1 Introduction

The nonlinear Schrodinger equation (NSE) is widely used to describe nonlinear dispersive wave propagation occurring in many branches of physics and engineering, such as plasma physics, nonlinear optics and fluids dynamics. One of the prominent features associated with the NSE is the existence of modulational instability (MI),[9] which causes small modulations of a plane wave propagating in a dispersive Kerr medium to grow exponentially.

A fundamental characterization for any unstable (or stable) dispersive system is the asymptotic spatiotemporal behavior of a small localized perturbation. Such an asymptotic impulse-response study can provide lots of important information, including the classification of the instability as convective or absolute, and the differentiation between evanescent and amplified waves. In fact, the asymptotic impulse-response study has been performed on most common instabilities in both plasmas and fluids, and the results can be found in standard textbooks.[29-32] However, for the important case of a nonlinear dispersive wave, this study was only done partially.[9] To fill the gap in the literature, the impulse response of a nonlinear plane wave in a dispersive Kerr medium is studied analytically. Some features pertinent to the MI system as revealed by the following impulse response study are discussed.

2.2 Impulse response

Let us write the NSE as

$$\partial_{t'} a = -v_g' \partial_{x'} a - i\mu \partial^2_{x'x'} a + i\lambda |a|^2 a. \tag{2.1}$$

where a is the complex wave amplitude, x' and t' are the spatial and temporal coordinates, v_g' is the group velocity, μ is the dispersion coefficient and λ is the nonlinear coefficient.

Equation (2.1) has a plane-wave solution $a_p(x,t) = a_0 \exp(i\lambda a_0^2 t)$, where a_0 is a complex constant representing the amplitude and phase of the plane wave. Without loss of generality, we assume a_0 to be a real positive quantity since its phase can always be canceled by a time translation. We will also assume λ is positive since the discussion for the negative case is quite similar. If we introduce the normalizations $A = a/a_0$, $x = x' a_0 \sqrt{\lambda/|\mu|}$, $t = t' \lambda a_0^2$, and $v_g = v_g' / \sqrt{a_0^2 \lambda |\mu|}$, Eq. (2.1) can be written in the normalized form,

$$\partial_t A = -v_g \partial_x A - i\, \sigma \partial^2_{xx} A + i|A|^2 A, \tag{2.2}$$

and the plane-wave solution becomes $A_p = \exp(it)$. We have used $\sigma = \text{sign}(\mu)$ to simplify the notation.

The evolution of the perturbative field is governed by Eq. (2.2) linearized around the plane-wave solution. Using $A = (1 + \delta A)\exp(it)$ in Eq. (2.2) and linearizing for δA, we obtain

$$\partial_t \delta A + v_g \partial_x \delta A + i\sigma \partial^2_{xx} \delta A - i\delta A - i\delta A^* = 0. \tag{2.3}$$

For the impulse-response analysis of the linearized equation, we need to solve the initial value problem of

$$\partial_t \delta A + v_g \partial_x \delta A + i\sigma \partial^2_{xx} \delta A - i\delta A - i\delta A^* = S(t)\delta(x), \tag{2.4}$$

with $\delta A(x, t) = 0$ for $t < 0$, where $S(t)\delta(x)$ is the point source of the perturbation. Equation (2.4) is readily solved by applying Fourier and Laplace transforms in x and t. The result is

$$i(-\omega + kv_g - \sigma k^2 - 1)\overline{\delta A}(\omega, k) - i[\overline{\delta A}(-\omega^*, -k)]^* = \overline{S}(\omega). \tag{2.5}$$

Since the above equation holds for arbitrary ω and k, we take its complex conjugate and replace ω and k with $-\omega^*$ and $-k$, respectively:

$$-i(\omega - kv_g - \sigma k^2 - 1)[\overline{\delta A}(-\omega^*, -k)]^* + i\overline{\delta A}(\omega, k) = [\overline{S}(-\omega^*)]^*. \tag{2.6}$$

Using Eq. (2.5) and (2.6), we obtain the solution

$$\overline{\delta A}(\omega, k) \quad = \quad i\frac{(\omega - v_g k - \sigma k^2 - 1)\overline{S}(\omega) - [\overline{S}(-\omega^*)]^*}{(\omega - v_g k)^2 - \sigma k^2(2 + \sigma k^2)}. \tag{2.7}$$

Its inverse transform is given by,

$$\delta A(x,t) = \int \frac{dk}{2\pi} \int_L \frac{d\omega}{2\pi} e^{-i\omega t + ikx} \overline{\delta A}(\omega, k) \tag{2.8}$$

where the integration paths of k and ω are the real axis and Landau contour (for the inverse Laplace transform, see[30]), respectively.

2.3 Time-asymptotic pulse evolution

We first consider $S(t) = c\delta(t)$, where c is generally a complex constant. In such a case, the Green function obtained from Eq. (2.8) corresponds to the evolution of a delta-pulsed perturbation. The evolution of a general pulse can be studied in terms of the convolution of the Green function. For simplicity, we assume $c = 1$ so that $\overline{S}(\omega) = 1$. We concern ourselves with the asymptotic spatiotemporal behavior of the Green function. Thus, we assume t is very large and work with a spatial coordinate normalized to t, i.e. $v = x/t$. In such a limit, the integrations in Eq. (2.8) can be carried out approximately. There are two equivalent approaches. Basically, the first one is to conceptually integrate k first and approximate the final integration of ω by the contributions from its branch points in the integrand. The second one is to integrate ω first and approximate the final integration of k by the contributions from its saddle points in the exponentials (i.e. by steepest descent integration). We adopt the second approach here. After carrying out the integration in Eq. (2.8) with respect to ω by summation of its simple poles at

$$\omega = v_g k \pm k\sqrt{k^2 + 2\sigma}, \tag{2.9}$$

in Eq. (2.7), we have,

$$\begin{aligned}\delta A(vt,t) &= \int \frac{dk}{2\pi} \exp[ikv't]\{[\exp(itk\sqrt{k^2+2\sigma}) + \exp(-itk\sqrt{k^2+2\sigma})]/2 \\ &\quad +\sigma\frac{\sqrt{k^2+2\sigma}}{2k}[\exp(itk\sqrt{k^2+2\sigma}) - \exp(-itk\sqrt{k^2+2\sigma})]\}, \quad (2.10)\end{aligned}$$

where $v' \equiv v - v_g$. Equation (2.9) is the dispersion relation. It indicates that the system is stable or unstable for $\mathrm{sign}(\mu) < 0$ or $\mathrm{sign}(\mu) > 0$.[9]

Equation (2.10) can be decomposed as the summation of four exponential integrals so that each integral can be carried out by the saddle point method for large t. To realize the decomposition, we need an infinitessimal deformation of the integration path around $k = 0$, i.e., along an infinitessimal semicircle above (below) $k = 0$. This does not change the value of the integration in Eq. (2.10) since $k = 0$ is an analytic point (removable singularity) of the total integrand, but it does make all four exponential integrals individually well defined. It is evident from Eq. (2.10) that $k = 0$ now becomes a simple pole for two of the four integrands. To evaluate each of the four integrals individually, we need to further deform their integration paths to reach their respective steepest descent paths. In some cases, the path will come across the simple pole in the deformation process. In such cases, the asymptotic value of the integral is the contribution from the saddle point and the pole. In the following, however, we will not explicitly decompose Eq. (2.10) and perform the above procedure. Instead, we only give the final results and concentrate on the physical picture.

We first consider the stable case in which $\mathrm{sign}(\mu) > 0$. Then, the time dependence of the contributions from the saddle points of $kv' \pm k\sqrt{k^2+2}$ in Eq. (2.10) normally has a decay factor $1/t^{1/2}$ [or $1/t^{1/3}$ if the group velocity dispersion, i.e. the second order derivative of $kv' \pm k\sqrt{k^2+2}$, is also zero at the saddle point] multiplied by an oscillatory or an exponentially decaying factor.[28] This is expected of an ordinary stable dispersive system, where an initial perturbation tends to disperse and vanish in the space-time domain. However, the simple pole contribution at $k = 0$ in the second term in Eq. (2.10) should also be considered. It actually gives the dominant contribution for large t. This effect is different from the ordinary stable dispersive system. As long as $v' \neq \sqrt{2}$, the saddle points and the pole $k = 0$ are separated. It turns out that the pole contribution can be obtained by the lowest order Taylor expansion of $\pm k\sqrt{k^2+2}$ in the exponential and $\sqrt{k^2+2}$ in the numerator at $k = 0$, and we have

$$\begin{aligned} \delta A(vt,t) &\simeq \int \frac{dk}{2\pi} \exp(ikv't)\frac{1}{\sqrt{2}k}[\exp(i\sqrt{2}kt) - \exp(-i\sqrt{2}kt)] \qquad (2.11)\\ &= (i/\sqrt{2})\mathrm{rect}[v'/(2\sqrt{2})] \qquad \text{for} \quad t \to \infty \qquad (2.12) \end{aligned}$$

where the rectangular function $\mathrm{rect}(y)$ is unity if $-1/2 < y < 1/2$ and zero elsewhere. The decaying saddle-point contributions have been neglected in Eqs. (2.11) and (2.12). Physically, we notice that the group velocity from the dispersion relation Eq. (2.9) is always in the ranges $v - v_g < -\sqrt{2}$ and $v - v_g > \sqrt{2}$ for $\mathrm{sign}(\mu) > 0$. Thus the finite level of perturbation within $-\sqrt{2} < v - v_g < \sqrt{2}$ at large t is due to the nonlinearity.

The above approximation breaks down around $v' = \pm\sqrt{2}$ within a "boundary layer" of v' which shrinks as $t \to \infty$. This is because the saddle point can then be so close to the pole $k = 0$ that the magnitude of the saddle point contribution is very large in this parameter region (although still decreasing for large t). Incidentally, the case of zero group-velocity-dispersion also corresponds to $v' = \sqrt{2}$. In order to find the solution for this "boundary layer", we need an approximation that is valid even when v' is close to $\sqrt{2}$. This can be accomplished by keeping the second-order terms in the Taylor expansion of $\pm k\sqrt{k^2-2}$ in the exponential since the saddle point contribution for v' around $\sqrt{2}$ is then automatically included. This results in

$$\begin{aligned}\delta A(vt,t) &\simeq \int \frac{dk}{2\pi}\exp(ikv't)\frac{1}{\sqrt{2}k}\{\exp[i\sqrt{2}kt+ik^3t/(2\sqrt{2})] \\ &\quad -\exp[-i\sqrt{2}kt-ik^3t/(2\sqrt{2})]\} &(2.13)\\ &= \frac{i}{\sqrt{2}}\{F[3^{-1/3}\sqrt{2}(\sqrt{2}+v')t^{2/3}]+F[3^{-1/3}\sqrt{2}(\sqrt{2}-v')t^{2/3}]\} &(2.14)\end{aligned}$$

for $t \to \infty$. where the function $F(\alpha) = \int(dy/2\pi)[\sin(\alpha y + y^3/3)]/y = 1/2 - \int_\alpha^\infty \mathrm{Ai}(y)dy = \int_{-\infty}^{\alpha}\mathrm{Ai}(y)dy - 1/2$. and $\mathrm{Ai}(\alpha)$ is the Airy function defined by $\mathrm{Ai}(\alpha) = \int_0^\infty \cos(\alpha y + y^3/3)dy/\pi$.[28] Since $F(\alpha) \sim \pm 1/2$ for $|\alpha| \gg 1$. it can be shown that for a fixed v' not very close to $\pm\sqrt{2}$, this result is identical with previous derivation. But this result also gives the boundary layer structure. By using $|\alpha| \sim 1$. it is easy to see that the thickness of boundary layers about $v' = \pm\sqrt{2}$ decreases as $1/t^{2/3}$ in the normalized spatial coordinate of v. This corresponds to a boundary layer of the order of $t^{1/3}$ in the spatial coordinate x. The structure of the boundary layer is isomorphic with the front of a water wave (surface-gravity wave).[28]

Figure 2-1 shows the result for $|\delta A(vt,t)|^2$ from numerical integration of Eq. (2.10) and our simplified calculations based on Eq. (2.14) and (2.12), which agree well even for a moderately long time of $t = 15$. Compared with the case of a linear medium,[28] this result shows that the development of a localized perturbation will be saturated at a certain level determined by the energy of the initial perturbation, instead of dispersing away. The perturbation will radiate outward, as it propagates with speed v_g, with both shock-like fronts moving out from the center with constant speed $\sqrt{2}$, so the total perturbation energy increase linearly with time. If $v_g < \sqrt{2}$, the perturbation will not vanish after a long time in the laboratory frame as do perturbations of ordinary dispersive waves.

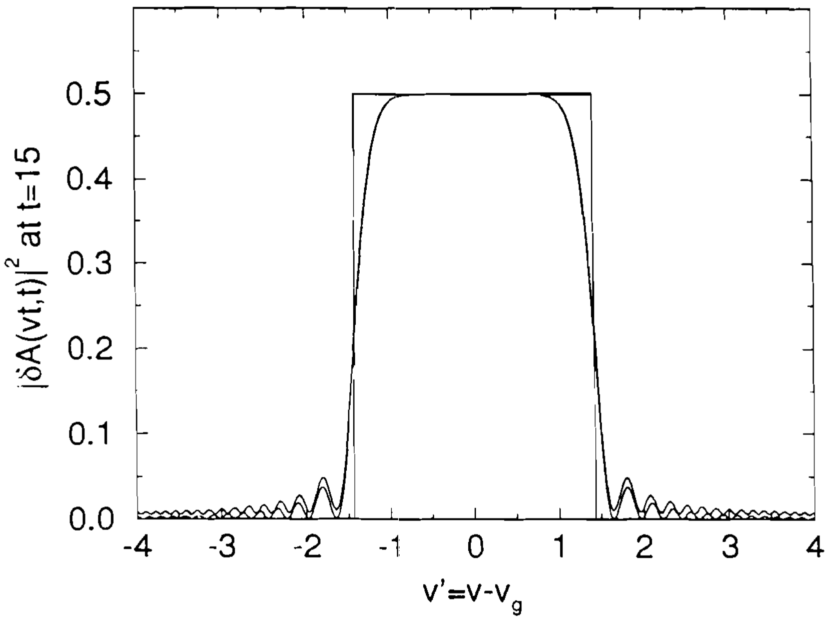

Figure 2-1: The shape of the Green function for the modulationally stable system plotted as $|\delta A(vt, t)|^2$ versus $v' \equiv v - v_g$ at $t = 15$. The square curve is the approximation from Eq. (2.12). The other two curves are the exact result from Eq. (2.10) (upper curve) and the approximation from Eq. (2.14) (lower curve), respectively.

We now turn our attention to the important case of the modulationally unstable system with sign(μ) < 0. In such a case, we can prove that the pole $k = 0$ in Eq. (2.10) cannot be a saddle point for any value of v. thus the saddle points and the pole are always separated, and the contribution to the integration at large t is just the summations of the pole contribution and the saddle point contributions. For the unstable portion of v, since the saddle point contribution represents an exponential growth with time, the pole contribution can be neglected. Actually, there are two saddle points from $kv' \pm k\sqrt{k^2 - 2}$ in Eq. (2.10) that give contributions growing exponentially with time. Compared to most unstable systems in which only one saddle-point contribution has the largest growth rate, here the growth rates of the two contributions are the same whereas their phases are different. Thus, as will be detailed in the following calculation, the amplitude of the asymptotic pulse is oscillatory with an exponentially growing envelope. This behavior is characteristic of a modulationally unstable system.

For the exponential $kv' + k\sqrt{k^2-2}$ in Eq. (2.10), the saddle points in the complex k plane satisfy

$$d_k[kv' + k\sqrt{k^2-2}] = 0. \tag{2.15}$$

The saddle point with exponentially growing contribution is determined to be

$$k(v) = -\sqrt{[8 + v'^2 + v'\sqrt{v'^2-16}]/8}. \tag{2.16}$$

Here we concern ourselves with $|v'| < 4$ for the unstable portion of the pulse. The value of the exponential $kv' + k\sqrt{k^2-2}$ and its second order derivative at the saddle point can be calculated to be

$$\begin{aligned} s(v) &= k(v)(3v' + \sqrt{v'^2-16})/4 && (2.17)\\ &= (\sqrt{2}/8)[v'^4 + 40v'^2 - 16 - v'(v'^2-16)^{3/2}]^{1/2} && (2.18)\end{aligned}$$

and

$$p(v) = 8k(v)[v'/(v'^2 - 8 - v'\sqrt{v'^2-16}) - (v' + \sqrt{v'^2-16})/8], \tag{2.19}$$

respectively. The value of the factor $\sqrt{k^2-2}/k$ in Eq. (2.10) at the saddle point is

$$d(v) = -(1/4)(v' - \sqrt{v'^2 - 16})/k(v). \tag{2.20}$$

In Eqs. (2.18)-(2.20), $k(v)$ is given by Eq. (2.16). Similar results can be obtained for the other exponential $kv' - k\sqrt{k^2 - 2}$ in Eq. (2.10).

According to the method of steepest descent, we add up the two saddle-point contribution from $kv' \pm k\sqrt{k^2 - 2}$. Detailed analysis shows that their contribution are complex conjugate to each other so that the final result can be written as

$$\begin{aligned} \delta A(vt,t) &\simeq (1/\sqrt{4\pi t})\mathrm{Re}[e^{is(v)t}/\sqrt{-ip(v)}] + \\ &\quad i(1/\sqrt{4\pi t})\mathrm{Im}[e^{is(v)t}d(v)/\sqrt{-ip(v)}] \qquad (2.21) \\ &= (1/\sqrt{4\pi t})e^{-\mathrm{Im}(s)t}\{\mathrm{Re}[e^{i\mathrm{Re}(s)t}/\sqrt{-ip}] + \\ &\quad i\,\mathrm{Im}[e^{i\mathrm{Re}(s)t}d/\sqrt{-ip}]\} \qquad (2.22) \end{aligned}$$

for $t \to \infty$, where by using Eq. (2.18),

$$\begin{aligned} -\mathrm{Im}(s) &= [4(2v'^2 + 4)^{3/2} + 32 - 40v'^2 - v'^4]^{1/2}/8, \qquad (2.23) \\ \mathrm{Re}(s) &= -\mathrm{sign}(v')[4(2v'^2 + 4)^{3/2} - 32 + 40v'^2 + v'^4]^{1/2}/8. \qquad (2.24) \end{aligned}$$

as are displayed in Fig. 2-2.

Equation (2.22) means that the envelope of asymptotic pulse is determined by $\exp(-\mathrm{Im}[s(v)]t)$,[9] while the frequency and phase of the amplitude oscillation are determined by $\mathrm{Re}[s(v)]t$, $p(v)$ and $d(v)$. The most important information for the instability is the magnitude of envelope, which gives the asymptotic temporal growth rate $-\mathrm{Im}[s(v)]$ displayed in Fig. 2-2. Thus the unstable portion of the pulse corresponds to $|v'| < 4$. By checking the asymptotic temporal growth rate

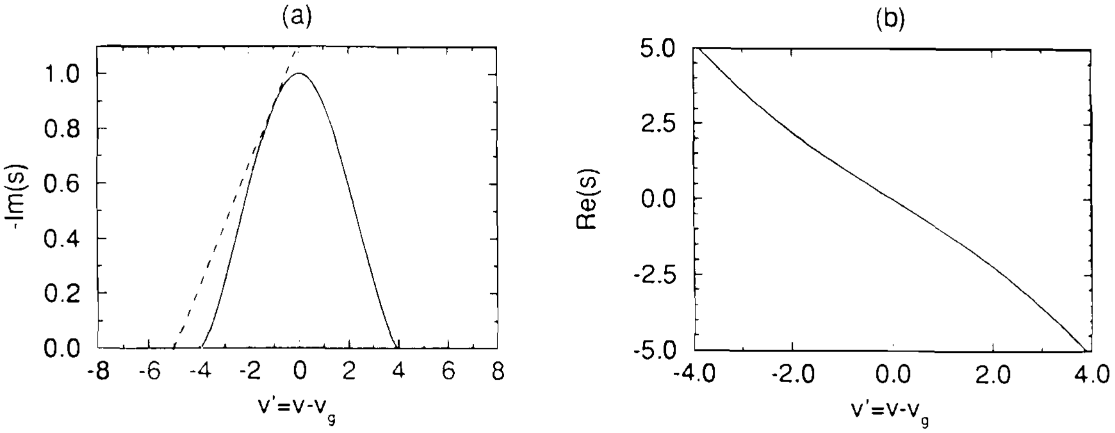

Figure 2-2: The real and imaginary part of the exponential factor $s(v)$ in the saddle point integration. (a) $-\text{Im}[s(v)]$ is the asymptotic growth rate. The slope of the dashed curve corresponds to maximum spatial growth rate for $v_g = 5$. (b) $\text{Re}[s(v)]$ is the phase for the oscillations in Fig. 2-3.

at $v = 0$,[29-32] we find that the instability is convective or absolute for $v_g > 4$ or $v_g < 4$. This is in agreement with previous results.[9]

In order to find a simpler expression for the pulse shape, we notice that the predominant portion of the pulse is around $v' = 0$ at large t. This allows us to take Taylor expansions for both exponentials and coefficients in Eq. (2.22) and keep only the lowest order terms. Then, Eq. (2.22) becomes,

$$\delta A(vt, t) \simeq \frac{1+i}{2\sqrt{2\pi t}} \exp[(1 - v'^2/8)t] \cos(v't). \tag{2.25}$$

The same result can be obtained by a second-order Taylor expansion of the exponentials $\pm itk\sqrt{k^2 - 2}$ in Eq. (2.10) around $k = \mp 1$, which correspond to their respective maxima. Figure 2-3 shows the asymptotic pulse shape plotted as $t\exp(-2t)|\delta A(vt, t)|^2$, determined by numerical integration of Eq. (2.10) and by our simplified Eq. (2.25). They agree each other well even for a moderately long time of $t = 10$.

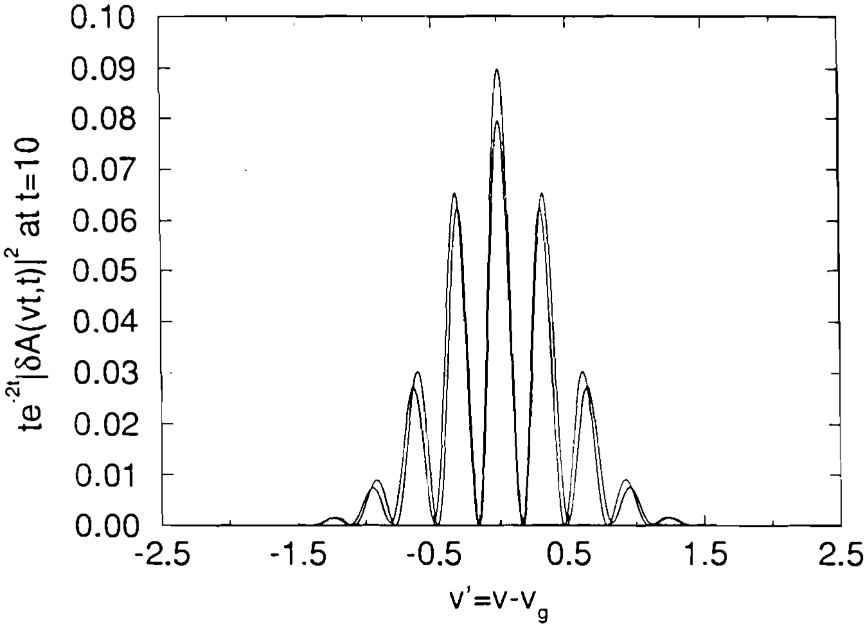

Figure 2-3: The shape of the Green function for the modulationally unstable system plotted as $t\exp(-2t)|\delta A(vt,t)|^2$ versus $v' \equiv v - v_g$ at $t = 10$. The two curves are the exact result from Eq. (2.10) (upper curve) and the approximation from Eq. (2.25) (lower curve).

2.4 Spatial amplification

Following the systematic approach of the impulse-response analysis,[29-32] we now study the spatial growth rate for the convectively unstable case in which $\mathrm{sign}(\mu) < 0$ and $v_g > 4$. This is accomplished by introducing a point source oscillating at a frequency ω_0 (i.e., zero spectral line width), and finding the steady-state spatial solution reached at large t (after a transient time), whose existence is guaranteed by the convective nature of the instability. The amplification of a signal with arbitrary line width can be studied in terms of spectrum decomposition. Thus, we assume $S(t) = \exp(-i\omega_0)t$ in Eq. (2.4) or $\overline{S}(\omega) = [i(\omega - \omega_0)]^{-1}$ in Eq.(2.7). In this analysis, we use the spatial coordinate x instead of the normalized spatial coordinate v since we are concerned with the steady state.

Following the standard approach,[29-32] we move the integration path of ω below its real axis. Due to the absence of absolute instability, The k integration path can always be deformed so that the solution at large t is only due to the pole of ω at ω_0 and can be expressed as

$$\delta A(x,t) \simeq \int_L \frac{dk}{2\pi} \exp(ikx) \frac{-(\omega_0 - v_g k + k^2 - 1)\exp(-i\omega_0 t) + \exp(i\omega_0 t)}{k^2(k^2-2) - (\omega_0 - v_g k)^2} \quad (2.26)$$

for $t \to \infty$, where L is the Landau contour. (For a detailed discussion, see.[30]) This steady-state solution can be reached for any fixed spatial coordinate x after a transient time. Physically, the new frequency component of $\exp(i\omega_0 t)$ is generated by the four-wave mixing process.

The integration in Eq. (2.26) can be worked out for $x > 0$ and $x < 0$ separately. For simplicity we only consider $x > 0$ since the case $x < 0$ is similar. Then the integration with k in Eq. (2.26) is just the residue summation from all the poles of the integrand above the Landau contour. For large x, the lowest pole at k_0 gives the dominant contribution, that is

$$\delta A(x,t) \simeq \exp\left[ik_0 x\right] \frac{-(\omega_0 - v_g k_0 + k_0^2 - 1)\exp(-i\omega_0 t) + \exp(i\omega_0 t)}{4k_0(k_0^2 - 1) + 2v_g(\omega_0 - v_g k_0)} \quad (2.27)$$

for $t \to \infty$, where $k_0(\omega_0)$ is a function of ω_0 and satisfies

$$k_0^2(k_0^2 - 2) - (\omega_0 - v_g k_0)^2 = 0. \quad (2.28)$$

For amplification, $k_0(\omega_0)$ should be below the real axis while still above the Landau contour. This criterion is equivalent to requiring the corresponding solutions of Eq. (2.28) to cross the real axis from above to below when we attach an imaginary part to ω_0 that goes from some positive value to zero. (For a detailed discussion, see.[30])

The solutions of Eq. (2.28) are of course functions of ω_0. A detailed study shows that for $v_g > 4$, there are two separate regions for positive ω_0, namely $(0, \omega_a)$ and (ω_e, ∞), that result in complex solutions of Eq. (2.28). However, only the first region corresponds to amplification. By applying the above criterion, it can be shown that the second one corresponds to evanescent waves. The same is true for negative ω_0 due to symmetry. As an example, Fig. 2-4 shows all four solution branches of Eq. (2.28) for $v_g = 5$ and for a varying ω_0. We have used the normalized frequency $\Omega_0 = \omega_0/v_g$, and chosen the attached imaginary part to Ω_0 to be from 0.4, 0.1 to 0, while its real part can be at some discrete values which are 0.1 apart in the range $(-5, 5)$. Thus, only the portion of the bow-shaped curve below the real axis in Fig. 2-4(d) has come across the real axis and corresponds to amplification. This portion of k_0 corresponds to the Ω_0 range of $(-1.35, 1.35)$, i.e. $\Omega_a = \omega_a/v_g = 1.35$.

Figures 2-5 shows the wave number $\mathrm{Re}[k_0(\omega_0)]$ as $\mathrm{Re}[k_0(\omega_0)] - \Omega_0$ and the spatial growth rate $-\mathrm{Im}[k_0(\omega_0)]$ as $-v_g\mathrm{Im}[k_0(\omega_0)]$ in the amplification range of Ω_0. The results were obtained by solving Eq. (2.28) for $v_g > 4$.

Figure 2-6 shows the amplification range Ω_a, the maximum growth rate as $v_g\max[-\mathrm{Im}(k_0)]$ and corresponding frequency $\Omega_m = \omega_m/v_g$ for different values of v_g. As v_g increases, the wave number $\mathrm{Re}(k_0)$ approaches Ω_0, the quantities $v_g\max[-\mathrm{Im}(k_0)]$, related to the maximum spatial growth rate, and Ω_m, related to the corresponding frequency, decrease to approach 1, and the normalized amplification frequency range Ω_a increases to approach $\sqrt{2}$. It should be pointed out that for a given v_g, $\max[-\mathrm{Im}(k_0)]$ is equal to the slope of the tangential line

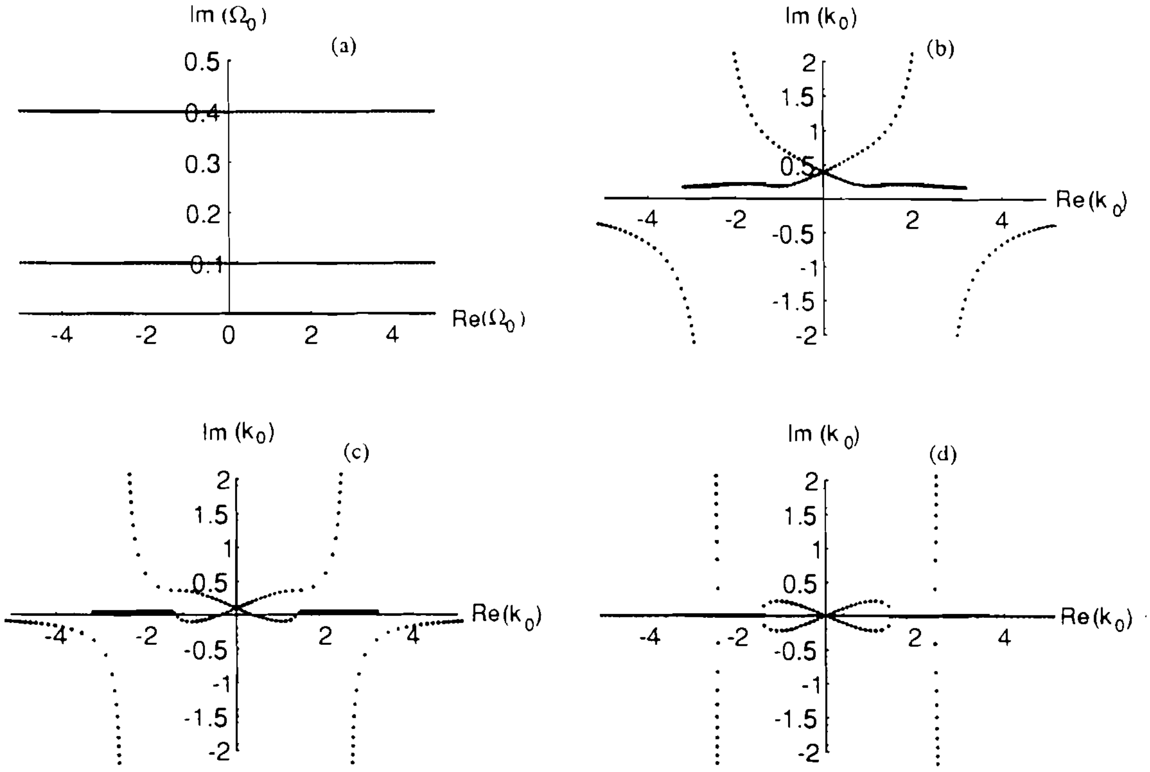

Figure 2-4: The four branches of the dispersion relation satisfying Eq. (2.28) for $v_g = 5$ and a varying parameter ω_0. (a) The values of the parameter $\Omega_0 = \omega_0/v_g$ are doted on the three horizontal lines at $\mathrm{Im}(\Omega_0) = 0.4$ (first), 0.1 (second) and 0 (third) with separation of 0.1 between the dots. (b) The four branches of the solution of Eq. (2.28) for the values of Ω_0 on the first line in (a). (c) Same as (b) except for the second line in (a). Note the part that crosses the real axis. (d) Same as (b) except for the third line in (a). Thus, k_0 is on the bow-shaped curve below the real axis.

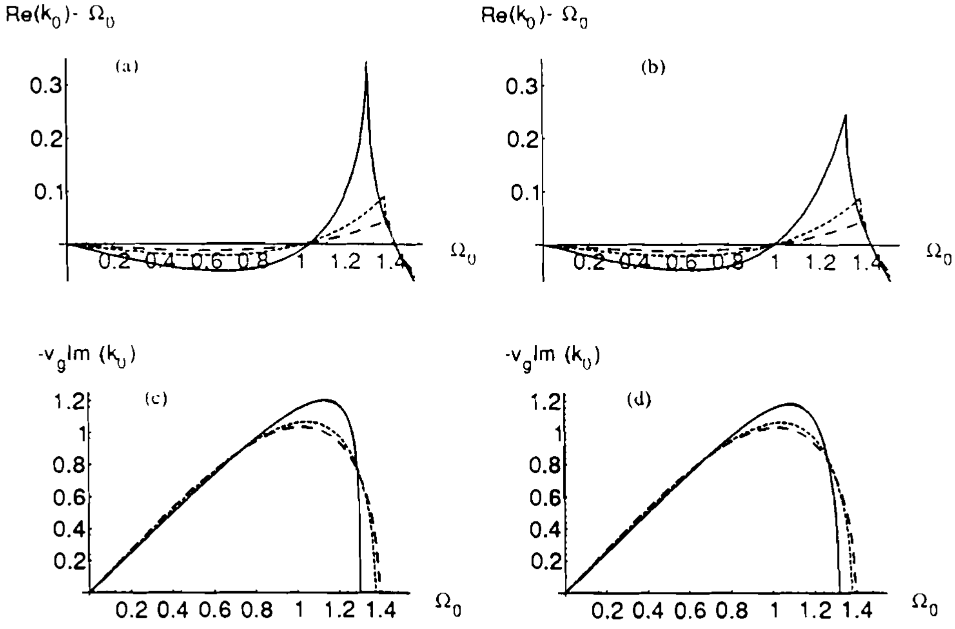

Figure 2-5: The spatial growth rate and corresponding wavenumber for the varying frequency in the amplification range and for $v_g = 4$ (solid), 6 (dashed) and 8 (long dashed). The wavenumber is plotted as $\mathrm{Re}(k_0) - \Omega_0$ versus $\Omega_0 = \omega_0/v_g$ in (a) and (b), and the spatial growth rate is plotted as $-v_g\mathrm{Im}(k_0)$ versus Ω_0 in (c) and (d), where (a) and (c) are the exact results from Eq. (2.28), and (b) and (d) are the approximations from Eq. (2.31).

shown in Fig. 2-2(a) (where we have used $v_g = 5$ as a example) as can be generally proved.[29-32]

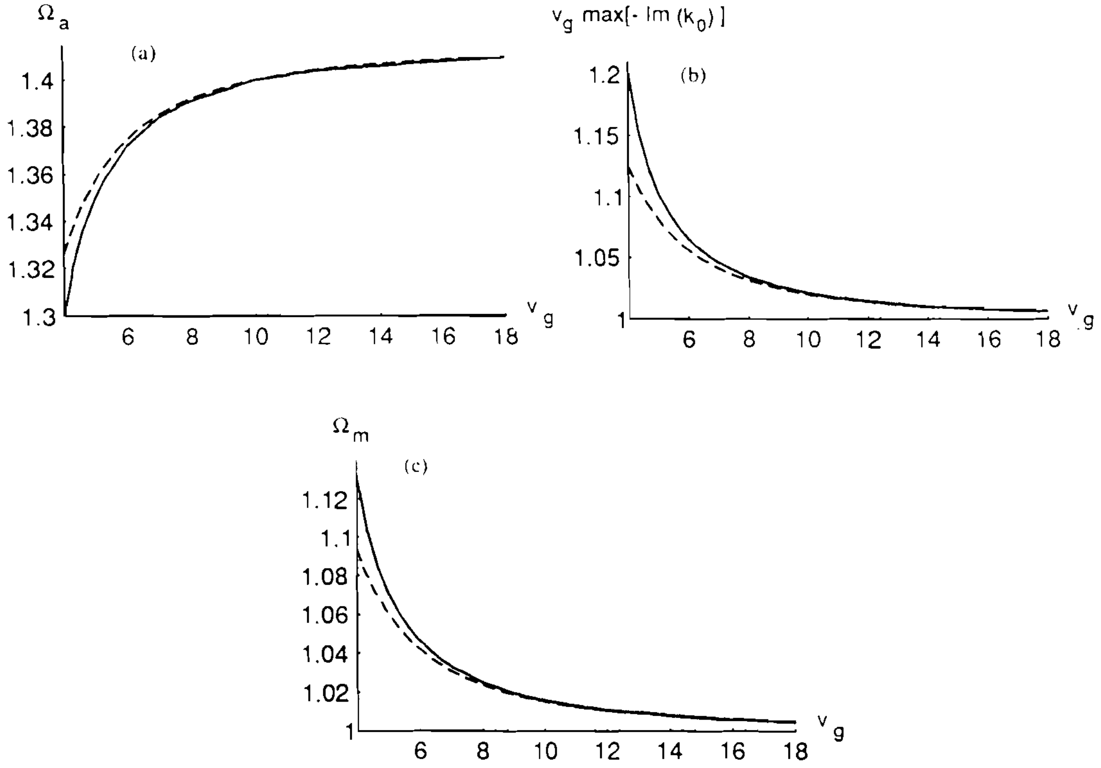

Figure 2-6: The amplification frequency range plotted as $\Omega_a = \omega_a/v_g$ (a), the maximum spatial growth rate plotted as $v_g\max[-\mathrm{Im}(k_0)]$ (b), and the corresponding frequency plotted as $\Omega_m = \omega_m/v_g$ (c) for varying v_g. The solid lines are from numerical calculations based on Eq. (2.28) and the dashed line are from the approximations based on Eqs. (2.32), (2.35) and (2.34).

The branch of the solution of Eq. (2.28) related to amplification can be obtained directly by treating v_g^{-2} as a small parameter since we have assumed $v_g > 4$. By writing Eq. (2.28) in the form

$$(k_0 - \Omega_0)^2 = v_g^{-2}(k_0^4 - 2k_0^2), \tag{2.29}$$

it is easy to see that the zeroth-order solution is $k_0 = \Omega_0$. The next order solution will be accurate to $O(v_g^{-1})$ and can be obtained by the first-order Taylor expansion of the right-hand-side of Eq. (2.29) at $k_0 = \Omega_0$. After taking the square root on both sides of the resulting equation, we have

$$k_0(\omega_0) \simeq \Omega_0 - v_g^{-1}\Omega_0\sqrt{\Omega_0^2 - 2}. \tag{2.30}$$

Thus $\Omega_a = \sqrt{2}$, $\Omega_m = 1$ and $v_g \max[-\mathrm{Im}(k_0)] = 1$ in agreement with the results in Figs. 2-5 and 2-6 for $v_g \gg 1$. This result can also be obtained from another version of the NSE used to study the boundary input problem, i.e. $\partial_{x'} a = -{v'}_g^{-1}\partial_{t'} a - i(\beta_2/2)\partial_{t't'}^2 a + i\gamma|a|^2 a$ where $\beta_2 = 2\mu/(v'_g)^3$ and $\gamma = \lambda/v'_g$. The two versions of the NSE are equivalent only when $v_g = v'_g/\sqrt{a_0^2\lambda|\mu|} \gg 1$.

The accuracy of Eq. (2.30) can be improved by considering the second-order Taylor expansion of the right-hand-side of Eq. (2.29) at $k_0 = \Omega_0$. In fact, one can prove that the solution thus obtained is accurate to $O(v_g^{-3})$ at least with higher accuracy around $\Omega_0 = 0$ and $\Omega_0 = \sqrt{2}$. The resulting second-order algebraic equation for k_0 can be easily solved to give,

$$k_0(\omega_0) - \Omega_0 \simeq \frac{2v_g^{-2}\Omega_0(\Omega_0^2 - 1) - v_g^{-1}\Omega_0\sqrt{\Omega_0^2 - 2 + 2v_g^{-2}(-\Omega_0^4 + 3\Omega_0^2)}}{[1 - 2v_g^{-2}(3\Omega_0^2 - 1)]} \tag{2.31}$$

Equation (2.31) is quite accurate, as shown in Fig. 2-5.

The frequency range for amplification can be easily obtained from Eq. (2.31) by setting the term under the square root to zero. The solution is

$$\Omega_a \simeq \sqrt{2}(1 - v_g^{-2}), \tag{2.32}$$

where we have Taylor-expanded the result up to the $O(v_g^{-2})$ term.

According to Eq. (2.31), the maximum growth rate $\max[-\mathrm{Im}(k_0)]$ and the corresponding frequency Ω_m can be obtained by studying the extremum of

$$\begin{aligned} & \frac{-v_g^{-1}\Omega_0\sqrt{\Omega_0^2 - 2 + 2v_g^{-2}(-\Omega_0^4 + 3\Omega_0^2)}}{[1 - 2v_g^{-2}(3\Omega_0^2 - 1)]} \simeq \\ & \quad -v_g^{-1}\sqrt{y^2 - 1 + 2v_g^{-2}(5y^3 + 4y^2 - 3y - 2)}, \end{aligned} \tag{2.33}$$

where $y = \Omega_0^2 - 1$ and a Taylor expansion has been made up to $O(v_g^{-2})$. The extremum of the argument under the square root of the right-hand-side of Eq. (2.33) can be easily found by using ordinary perturbation with respect to v_g^{-2}. After some straightforward algebra, we obtain

$$\Omega_m \simeq 1 + (3/2)v_g^{-2}. \tag{2.34}$$

$$v_g\max[-\mathrm{Im}(k_0)] \simeq 1 + 2v_g^{-2}. \tag{2.35}$$

where we have kept terms up to $O(v_g^{-2})$ in the expansions.

Equations (2.32), (2.34) and (2.35) are good approximations as long as $v_g^2 \gg 1$. The comparison with the numerical solution is displayed in Fig. 2-6.

2.5 Conclusions

We report the result of impulse-response analysis for a nonlinear wave in a dispersion medium. The Green function (response to a pulse-like perturbation) and the solution for oscillatory perturbations were studied. For a modulationally unstable system, the asymptotic pulse not only grows but is also modulated, i.e. the perturbation pulse consists of a modulated structure whose envelope grows exponentially. The pulse shape and the condition for convective and absolute instability are obtained analytically. Even for a modulationally stable nonlinear dispersive system, the perturbation does not disperse away as it does in a linear system. Instead, a certain level of perturbation, determined by the energy of the initial pulse, occurs in a widening region of space whose center moves with the group velocity. In a sense, it is like a spreading square pulse. For an oscillatory perturbation source, we determined the frequency regions for amplification and evanescence. The spatial growth rates for amplifying waves were obtained. The results also showed that the spatial NSE and temporal NSE are equivalent only for $v_g \gg 1$.

Chapter 3

Modulational Instabilities in Dispersion-Flattened Fibers

3.1 Introduction

MI is usually studied within the framework of a NSE, the validity of which requires a weak instantaneous nonlinearity and a slowly-varying wave amplitude. In the frequency domain, the spectral width of the field must be narrow enough that the modal dispersion relation $\beta(\omega)$ can be approximated by a second-order Taylor expansion around the carrier frequency ω_0. For slightly wider bandwidths, some corrections to NSE have been made by adding higher-order dispersion terms in the Taylor expansion.[34-37]

In some cases discussed below, however, MI can actually occur with a wide bandwidth (corresponding to a fast temporal modulation). In other words, the effects of second- and third-order dispersion, etc., could be all comparable in these cases; the Taylor expansion breaks down, and the nonlocal properties of the modal dispersion relation must be considered. For fast modulations, nonlinear relaxation and the Raman effect may also become important.[11,35,37,38] Because of the non-instantaneous nonlinearity, the dependence of the nonlinear coefficient on the modulational frequency should be included.

Broader-bandwidth MI is important due to its intrinsic relation to shorter pulses. In this paper, we use harmonic analysis instead of the NSE to study MI. This approach still requires weak nonlinearity but does not require narrow bandwidth. A simple expression for the gain curve of MI is given that depends on the entire modal dispersion curve and the frequency-dependent nonlinear coefficients. It is then applied to a dispersion-flattened fiber,[40] for which the second-order dispersion coefficient changes sign twice as the frequency is varied, to study the effects of the modal dispersion relation and to illustrate the basic physics.

3.2 Harmonic analysis

To be precise, the harmonic analysis described below is actually a multiscale approximation[61] used to solve the linearized equation around a nonlinear steady-state pump wave in a single-mode fiber. The small parameter in the linearized equation is the amplitude of the nonlinear pump wave normalized to $\sqrt{\beta(\omega_0)/\gamma}$ [see Eq. (3.4)]. In the following summary, however, the physical picture is emphasized at the expense of mathematical detail.

Consider wave propagation in a single-mode fiber. The electric field is written as

$$\overline{E}(t, x, y, z) = \overline{A}(t, z)\overline{F}(x, y), \tag{3.1}$$

where $\overline{A}$ is referred to as the wave amplitude and the function $\overline{F}$ describes the transverse variation of the field. The Fourier amplitude of the wave is defined according to the convention

$$A(\omega, z) = \frac{1}{2\pi}\int_{-\infty}^{\infty} \overline{A}(t, z)\exp(i\omega t)dt. \tag{3.2}$$

It is well known that the nonlinear steady-state or CW pump wave for the single transverse mode of the fiber is approximately a sinusoidal wave with dispersion relation[11, 12]

$$k_s(\omega_0) = \beta(\omega_0) + \gamma(\omega_0, -\omega_0, \omega_0)|A_0|^2, \tag{3.3}$$

where the subscript s is for steady state, and the weak nonlinearity condition

$$\gamma|A_0|^2 \ll \beta(\omega_0) \tag{3.4}$$

is required. Equations (3.3) and (3.4) indicate that the $\chi^{(3)}$ nonlinearity changes the wave number (and the phase, which is the product of wave number and distance) by a small amount. For an optical fiber, $\gamma(\omega_0, -\omega_0, \omega_0) = 6\pi\omega_0\chi^{(3)}(\omega_0, -\omega_0, \omega_0)/[cn(\omega_0)A_{\text{eff}}]$ in electrostatic units, to within a factor of the order of unity that depends on the transverse mode structure, where $\chi^{(3)}(\omega_0, -\omega_0, \omega_0)$ is the third-order nonlinear susceptibility of the fiber, c is the speed of light, $n(\omega_0)$ is the modal refractive index, and A_{eff} is its effective mode area.[12]

An equation linearized around the CW solution can then be formed for a perturbation field. The evolution of the perturbation field in the presence of the cw pump described by Eq. (3.3) can be studied in Fourier domain by considering the propagation of its frequency components $\delta A(\omega', z)$ for the single transverse mode, where z and ω' represent space and frequency coordinates, respectively. Since the amplitude of the cw field is the small parameter, the trivial case of the zeroth-order approximation, which corresponds to a vanished pump, gives a linear propagation of the perturbation field, i.e. $d_{zz}^2\delta A(\omega', z) + \beta^2(\omega')\delta A(\omega', z) = 0$. The zeroth-order solution is thus $\delta A(\omega', z) = \delta A(\omega', 0)\exp[i\beta(\omega')z]$, corresponding to forward propagation. Note that the reality condition requires $\delta A(-\omega', z) = \delta A^*(\omega', z)$.

In the presence of the CW pump-wave, the following linearized equation for $\delta A(\omega', z)$ can be obtained from the Maxwell equation for the single transverse mode:

$$d_{zz}^2\delta A(\omega', z) + \beta^2(\omega')\delta A(\omega', z) = (4\pi/c)\omega'^2\delta P_{nl}(\omega'), \tag{3.5}$$

where the term δP_{nl}, still linear in the perturbative field, is the nonlinear part of the electric polarization field projected onto the transverse mode by an overlap integration.[12]

Recall that $\delta P_{nl} \simeq 0$ in the zeroth-order approximation. For a better approximation beyond zeroth order, we have

$$\begin{aligned}\delta P_{nl}(\omega') \;=\; & (3/A_{\text{eff}})\int\int\int_{-\infty}^{+\infty}\chi^{(3)}(\omega_1, \omega_2, \omega_3) \\ & E_0(\omega_1, z)E_0(\omega_2, z)\delta A(\omega_3, z)\delta(\omega' - \omega_1 - \omega_2 - \omega_3)d\omega_1 d\omega_2 d\omega_3, \end{aligned} \tag{3.6}$$

where we have assumed the overlap integral of the transverse mode is the same for the frequencies of interest.[12] $E_0(\omega, z) = A_0\exp[ik_s(\omega_0)z]\delta(\omega-\omega_0)+A_0^*\exp[-ik_s(\omega_0)z]\delta(\omega+\omega_0)$ is the Fourier transform of the cw field $\overline{E}_0(t, z) = A_0\exp[ik_s(\omega_0)z - i\omega_0 t] + c.c.$. Equation (3.6) describes the nonlinear electric polarization (but linear in the perturbation field) induced by the pump and the perturbation field in the $\chi^{(3)}$ medium. The degeneracy factor 3 appears because we treat the perturbation as a different field from the pump wave.[11] We have neglected higher-order (greater than $|A_0|^2$) contributions of the pump field to δP_{nl}.

To solve Eq. (3.5) beyond the zeroth-order approximation, we follow the multiscale procedure by inserting the zeroth-order solution in the right-hand-side of Eq. (3.5) [using Eq. (3.6)] and collecting all the possible phase-matched terms. This analysis can be facilitated by switching to the temporal-domain picture. For a forward propagation component at ω', the field is $\delta A(\omega', 0)\exp[i\beta(\omega')z - i\omega' t] + c.c.$. Through the nonlinear electric polarization, this field generates the terms proportional to $\delta A(\omega', z)|A_0|^2\exp[i\beta(\omega')z - i\omega' t] + c.c.$ and $\delta A^*(\omega', z)A_0^2\exp\{i[2k_s(\omega_0) - \beta(\omega')]z - i(2\omega_0 - \omega')t\} + c.c.$. The first term is obviously phase-matched. The second term could also be phase-matched to a forward propagating component at $(2\omega_0 - \omega')$ if $|2k_s(\omega_0) - \beta(\omega') - \beta(2\omega_0 - \omega')|$ is very small. Thus we should study the component $\delta A(2\omega_0 - \omega', z) = \delta A(2\omega_0 - \omega', 0)\exp[i\beta(2\omega_0 - \omega')z - i(2\omega_0 - \omega')t] + c.c.$. Similar analysis for this component indicates two phase-matched terms generated at $(2\omega_0 - \omega')$ and ω'.

According to the multiscale procedure, the above consideration allows us to solve Eq. (3.5) approximately in terms of the coupled mode equation of the frequency components at ω' and $2\omega_0 - \omega'$, called the anti-Stokes and Stokes sideband for the upshifted and downshifted frequency, respectively. By retaining all the possible phase-matched driving terms, Eqs. (3.5) and (3.6) become

$$
\begin{aligned}
&[d_{zz}^2 + \beta^2(\omega')]\delta A(\omega', z)/[2\beta(\omega')] = \\
&\quad 2\gamma(\omega_0, -\omega_0, \omega')|A_0|^2\delta A(\omega', z) \\
&\quad +\gamma[\omega_0, \omega_0, -(2\omega_0 - \omega')]A_0^2\exp[i2k_s(\omega_0)]\delta A^*(2\omega_0 - \omega', z) \qquad (3.7)
\end{aligned}
$$

$$
\begin{aligned}
&[d_{zz}^2 + \beta^2(2\omega_0 - \omega')]\delta A(2\omega_0 - \omega', z)/[2\beta(2\omega_0 - \omega')] = \\
&\quad 2\gamma(\omega_0, -\omega_0, 2\omega_0 - \omega')|A_0|^2\delta A(2\omega_0 - \omega', z) \\
&\quad +\gamma(\omega_0, \omega_0, -\omega')A_0^2\exp[i2k_s(\omega_0)]\delta A^*(\omega', z), \qquad (3.8)
\end{aligned}
$$

where we have defined

$$\gamma(\omega_1, \omega_2, \omega_3) = 6\pi(\omega_1 + \omega_2 + \omega_3)\chi^{(3)}(\omega_1, \omega_2, \omega_3)/[cn(\omega_1 + \omega_2 + \omega_3)A_{\text{eff}}]. \quad (3.9)$$

Equations (3.7) and (3.8) will give a correction to the linear dispersion relation $\beta(\omega')$ [or $\beta(2\omega_0 - \omega')$ for frequency $2\omega_0 - \omega'$] by an amount $O(\gamma|A_0|^2)$. Simplification can be made for forward propagation by using $(d_{zz}^2 + \beta^2)/(2\beta) = (-id_z + \beta)(id_z + \beta)/(2\beta) \simeq id_z + \beta$ [where β indicates $\beta(\omega')$ or $\beta(2\omega_0 - \omega')$] since a careful analysis shows this doesn't alter current level of approximation at all. If we define the modulational frequency $\omega \equiv \omega' - \omega_0$, and set $\delta A(\omega', z) \equiv B_+(\omega, z)\exp(ik_s z)$ and $\delta A(2\omega_0 - \omega', z) \equiv B_-(\omega, z)\exp(ik_s z)$, then Eqs. (3.7) and (3.8) become.

$$\begin{aligned} D_+(-id_z, \omega)B_- &= \gamma_{f+}A_0^2 B_-^*, & (3.10)\\ D_-(-id_z, \omega)B_-^* &= -\gamma_{f-}^* A_0^{*2} B_+, & (3.11) \end{aligned}$$

where

$$\begin{aligned} D_+(-id_z, \omega) &\equiv -id_z + \beta(\omega_0) - \beta(\omega_0 + \omega) - \gamma_{x+}|A_0|^2 & (3.12)\\ D_-(-id_z, \omega) &\equiv -id_z - \beta(\omega_0) + \beta(\omega_0 - \omega) + \gamma_{x-}^*|A_0|^2. & (3.13) \end{aligned}$$

and

$$\begin{aligned} \gamma_{x+} &\equiv 2\gamma[\omega_0, -\omega_0, (\omega_0 + \omega)] - \gamma(\omega_0, -\omega_0, \omega_0), & (3.14)\\ \gamma_{x-} &\equiv 2\gamma[\omega_0, -\omega_0, (\omega_0 - \omega)] - \gamma(\omega_0, -\omega_0, \omega_0), & (3.15)\\ \gamma_{f+} &\equiv \gamma[\omega_0, \omega_0, -(\omega_0 - \omega)], & (3.16)\\ \gamma_{f-} &\equiv \gamma[\omega_0, \omega_0, -(\omega_0 + \omega)]. & (3.17) \end{aligned}$$

The subscripts x and f refer to cross-phase modulation (XPM) and four-wave mixing (FWM) to indicate their relation to these processes, respectively. Note the Raman effect and the effect of nonlinear relaxation is included through the dependence of the nonlinear coefficients on the modulational frequency.

Equations (3.10) and (3.11) can be easily solved. The general solution consists of two independent eigenmodes,

$$\begin{pmatrix} B_+ \\ B_-^* \end{pmatrix} = c_1 \begin{pmatrix} 1 \\ r_+(\omega) \end{pmatrix} e^{ik_+(\omega)z} + c_2 \begin{pmatrix} r_-(\omega) \\ 1 \end{pmatrix} e^{ik_-(\omega)z}, \tag{3.18}$$

where c_1 and c_2 are constants, and

$$r_+ = D_+(k_+,\omega)/\gamma_{f+}A_0^2 = -\gamma_{f-}^*A_0^{*2}/D_-(k_+,\omega), \tag{3.19}$$

$$r_- = \gamma_{f+}A_0^2/D_+(k_-,\omega) = -D_-(k_-,\omega)/\gamma_{f-}^*A_0^{*2} \tag{3.20}$$

indicate the relative amplitudes of Stokes and anti-Stokes sidebands for each eigenmode, respectively. $k_\pm(\omega)$ are the dispersion relations for the two eigenmodes,

$$\begin{aligned} k_\pm(\omega) \; = \; & \Big[\beta(\omega_0+\omega) - \beta(\omega_0-\omega) + (\gamma_{x+} - \gamma_{x-}^*)|A_0|^2 \\ & \pm\sqrt{\Delta^2 - 4\gamma_{f+}\gamma_{f-}^*|A_0|^4} \;\Big]/2, \end{aligned} \tag{3.21}$$

where

$$\Delta(\omega) \equiv \Delta_l - \gamma_{x+}|A_0|^2 - \gamma_{x-}^*|A_0|^2, \tag{3.22}$$

is the total wave-number mismatch and

$$\Delta_l(\omega) \equiv 2\beta(\omega_0) - \beta(\omega_0+\omega) - \beta(\omega_0-\omega) \tag{3.23}$$

is the linear wave-number mismatch (the subscript l is for linear). Naturally, a negative imaginary part of $k_\pm(\omega)$ indicates the growth of the corresponding eigenmode.

Physically, the coupled Eqs. (3.10) and (3.11) describe the linearized stage of the induced decay of the carrier wave at the frequency ω_0 into its daughter waves at the sideband frequencies $\omega_0 \pm \omega$. The right side of each equation represents the harmonic driving from the nonlinear beating or FWM of the carrier and the other daughter wave, and the left side describes propagation with total wave number mismatch (including linear and nonlinear mismatch). The nonlinear wavenumber mismatch comes from XPM, and is generally complex due to the Raman effect or nonlinear relaxation. Alternatively, Eqs. (3.10) and (3.11) describe the scattering of the pump into one of the sidebands by the nonlinear grating produced by the pump and the other sideband. These equations decouple automatically when $|\gamma A_0^2/\Delta_l| \ll 1$. In this limit, without loss of accuracy, the two independent eigenmodes of Eqs. (3.10) and (3.11) become

$$\begin{cases} k_+ = -\beta(\omega_0) + \beta(\omega_0 + \omega) + \gamma_{x+}|A_0|^2, \\ r_+ \simeq 0 \quad \text{or,} \quad B_- = 0 \end{cases} \tag{3.24}$$

and

$$\begin{cases} k_- = \beta(\omega_0) - \beta(\omega_0 - \omega) - \gamma_{x-}^*|A_0|^2, \\ r_- \simeq 0 \quad \text{or,} \quad B_+ = 0. \end{cases} \tag{3.25}$$

Physically, these solutions correspond to the independent evolution of each sideband subject to Raman loss (for the anti-Stokes sideband) or gain (for the Stokes sideband) and with the refractive index changed by the pump due to XPM.

Generally, each frequency component cannot propagate independently, but couples to the other sideband. In fact, expressing c_1 and c_2 in terms of the input condition leads to the general solution in form of a transfer matrix,

$$\begin{pmatrix} B_+(\omega, z) \\ B_-^*(\omega, z) \end{pmatrix} = \frac{1}{1 - r_+r_-} \begin{pmatrix} e^{ik_+z} - r_+r_-e^{ik_-z} & r_-(e^{ik_-z} - e^{ik_+z}) \\ r_+(e^{ik_+z} - e^{ik_-z}) & e^{ik_-z} - r_+r_-e^{ik_+z} \end{pmatrix} \begin{pmatrix} B_+(\omega, 0) \\ B_-^*(\omega, 0) \end{pmatrix}. \quad (3.26)$$

This equation linearly relates the Fourier spectrum at any distance z to the input spectrum.

In the case of instability and at large distances, the contribution from the damped eigenmode can be neglected. Then $\mathrm{Im}[k_+(\omega)]$ gives the information about the spectrum amplification with distance, while $|r_+(\omega)|$ indicates the relative amplitude of Stokes and anti-Stokes sidebands, if the + sign is used to represent the growing mode.

To isolate the effect of the shape of the modal dispersion curve $\beta(\omega')$, we first neglect the frequency dependence of the nonlinear coefficients by using their value at zero modulational frequency $\omega = 0$. It is easy to show that $\gamma_{x\pm} = \gamma_{f\pm} = \gamma(\omega_0, -\omega_0, \omega_0)$, which is a parameter denoted by γ. This means that the Raman effect and other dependence of nonlinear coefficients on frequency are neglected. Then Eq. (3.21) becomes

$$k_\pm = \left[\ \beta(\omega_0 + \omega) - \beta(\omega_0 - \omega) \pm \sqrt{(\Delta_l - 2\gamma|A_0|^2)^2 - (2\gamma|A_0|^2)^2}\ \right] /2, \quad (3.27)$$

where the term $\Delta_l - 2\gamma|A_0|^2$ under the square root is just the total wave-number mismatch Δ, which is real in this case. Instability happens whenever its amplitude is smaller than that of the FWM coupling strength $2\gamma|A_0|^2$. (This condition means that the linear mismatch compensates nonlinear mismatch.) It can be proved that

$|r_+(\omega)| = 1$ for ω in the unstable range, so the amplitudes of the Stokes and anti-Stokes waves are equal for the growing mode. In the following, we only consider the $\gamma > 0$ case. Since the $\gamma < 0$ case is similar, our discussion can be easily extended.

The instability happens when

$$0 < \Delta_l(\omega) < 4\gamma|A_0|^2. \tag{3.28}$$

In a diagram of $\Delta_l(\omega)$ (see, for example, Fig. 3-1), the instability range is between the horizontal axis and the horizontal line at $4\gamma|A_0|^2$. If, in this range, $\Delta_l(\omega)$ reaches the value $2\gamma|A_0|^2$, then the maximum growth rate $[\text{Im}(k)]_{\text{max}} = \gamma|A_0|^2$ is obtained, corresponding to a complete linear compensation of the nonlinear wave-number mismatch; if it does not (as can happen in the dispersion-flattened fiber), the maximum growth rate happens at Δ_{le} (the subscript e is for extremum), which is the extremum of $\Delta_l(\omega)$ closest to the horizontal line at $2\gamma|A_0|^2$, with a value

$$[\text{Im}(k)]_{\text{max}} = \sqrt{(2\gamma|A_0|^2 - \Delta_{le})^2 - (2\gamma|A_0|^2)^2} \Big/ 2 \;\; < \gamma|A_0|^2. \tag{3.29}$$

This corresponds to maximal, but incomplete, compensation.

In many situations, the second-order dispersion function, defined as $\beta_2(\omega') \equiv \beta''(\omega')$ is given instead of the modal dispersion $\beta(\omega')$. Thus we wish to express $\Delta_l(\omega)$ in terms of the second-order dispersion function. Since $(d/d\omega)^2\Delta_l(\omega) = -\beta_2(\omega_0+\omega) - \beta_2(\omega_0-\omega)$ and $\Delta_l'(0) = \Delta_l(0) = 0$ from Eq. (3.23), we can show that

$$\Delta_l(\omega) \;\; = \;\; \int_0^{\omega} [\beta_2(\omega_0+\nu) + \beta_2(\omega_0-\nu)](\nu-\omega)d\nu, \tag{3.30}$$

For very small modulational frequency, a parabolic approximation for the

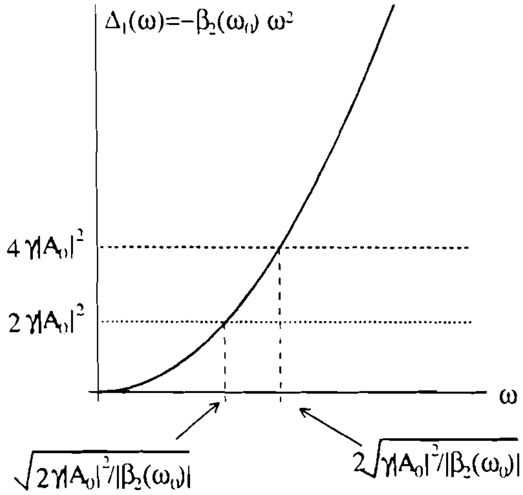
$\Delta_l(\omega)=-\beta_2(\omega_0)\ \omega^2$
$4\gamma|A_0|^2$
$2\gamma|A_0|^2$
ω
$\sqrt{2\gamma|A_0|^2/|\beta_2(\omega_0)|}$
$2\sqrt{\gamma|A_0|^2/|\beta_2(\omega_0)|}$

Figure 3-1: The instability analysis using $\Delta_l(\omega) = -\beta_2(\omega_0)\omega^2$. The upper dashed horizontal line is $4\gamma|A_0|^2$ and the lower is $2\gamma|A_0|^2$. The frequency range of instability corresponds to the section of $\Delta_l(\omega)$ curve between the horizontal axis and upper dashed horizontal line. The intersections of the curve with the lower dashed horizontal line indicate the frequency of maximum growth rate $\gamma|A_0|^2$. As power increases, both horizontal lines go up.

modal dispersion curve $\beta(\omega')$ can be used around the pump frequency. This is equivalent to considering $\beta_2(\omega')$ a constant within the frequency range of investigation: $\beta_2(\omega_0 \pm \omega) = \beta_2(\omega_0)$. It follows from Eq. 3.30, $\Delta_l(\omega) = -\beta_2(\omega_0)\omega^2$, which is displayed in Fig. 3-1 for the case of $\beta_2(\omega_0) < 0$. This figure also indicates that the instability range is $2\sqrt{\gamma|A_0|^2/|\beta_2(\omega_0)|}$ and the maximum growth is $\gamma|A_0|^2$. These results agree with those obtained from the standard NSE model.[12]

However, as the power increases [but Eq. (3.4) must be satisfied] or the second-order dispersion coefficient at the pump frequency decreases, the instability range becomes wider, and finally the approximation that $\beta(\omega')$ is parabolic, or $\beta_2(\omega')$ is constant, breaks down. In addition, this treatment will miss any MI gain occurring at relatively large ω. So, to explore the broad-bandwidth behavior of the MI gain, the exact linear dispersion relation should be used.[48] A good example is the dispersion-flattened fiber discussed in the following section.

3.3 Dispersion-flattened fiber

3.3.1 $\beta_{2e} < 0$ case

A dispersion-flattened fiber[40] has the characteristic second-order dispersion function shown in Fig. 3-2. Notice that $\beta_2(\omega)$ cannot be considered constant in the frequency range of interest because it changes sign twice. As a simple model, we fit the curve with a parabola. With this assumption,

$$\beta_2(\omega') = \beta_{2e}[1 - (\omega' - \omega_p')^2/\omega_z^2], \tag{3.31}$$

where β_{2e} is the minimal value of $\beta_2(\omega')$ occurring at the frequency ω_p', and $2\omega_z$ is the frequency spacing between the two points of zero dispersion (the subscript e

and z are for extremum and zero respectively). In an ordinary dispersion flattened-fiber β_{2e} is negative.

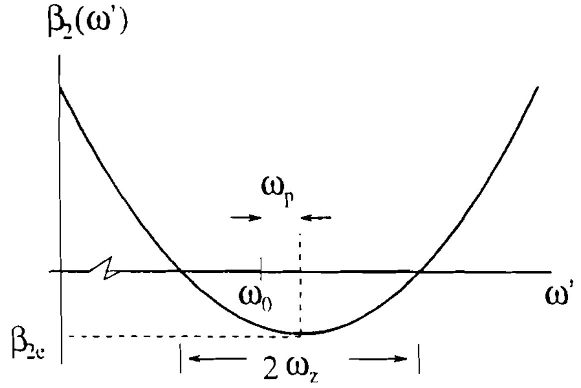

Figure 3-2: Illustration of $\beta_2(\omega')$ for a dispersion-flattened fiber. β_{2e} and ω_p are the extreme β_2 value and the corresponding frequency relative to the pump frequency, respectively. $2\omega_z$ is the difference between the two zero-dispersion frequencies.

Using Eqs. (3.30) and (3.31), we get

$$\Delta_l(\omega) = -\beta_{2e}(1-\omega_p^2/\omega_z^2)\omega^2[1-\frac{\omega^2}{6\omega_z^2(1-\omega_p^2/\omega_z^2)}], \tag{3.32}$$

where $\omega_p = \omega_p' - \omega_0$ is the minimum dispersion frequency relative to the pump frequency. Instability analysis based on $\Delta_l(\omega)$ is displayed in Fig. 3-3. Its two zero points are at $\omega = 0$ and ω_f (the subscript f is for FWM), where

$$\omega_f^2 = 6\omega_z^2(1-\omega_p^2/\omega_z^2). \tag{3.33}$$

Usually the zeros of linear mismatch at nonzero ω's imply the presence of FWM instabilities for some parameter values. The maximum of Δ_l happens at

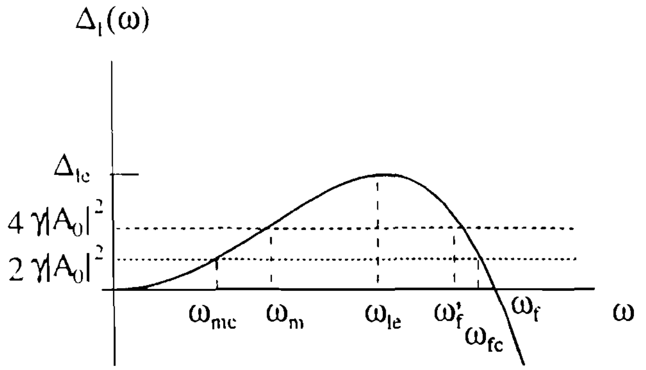
$\Delta_l(\omega)$
Δ_{lc}
$4\gamma|A_0|^2$
$2\gamma|A_0|^2$
ω_{mc}
ω_m
ω_{lc}
ω'_f
ω_{fc}
ω_f
ω

Figure 3-3: The instability analysis using $\Delta_l(\omega)$ in the case of dispersion-flattened fiber. The upper and lower dashed horizontal lines are $4\gamma|A_0|^2$ and $2\gamma|A_0|^2$, respectively. The two frequency ranges of instability correspond to the two sections of $\Delta_l(\omega)$ curve between the horizontal axis and upper dashed horizontal line, i.e., $(0, \omega_m)$ and (ω'_f, ω_f). The two intersections of the curve with the lower dashed horizontal line at ω_{mc} and ω_{fc} indicate the frequencies of maximum growth rate $\gamma|A_0|^2$. As power increases, both horizontal lines go up and the two instability regions merge. With a further power increase, the intersections of the curve with the lower dashed horizontal line also disappear.

ω_{le} (the subscript l is for linear and e is for extremum), where

$$\omega_{le}^2 = 3\omega_z^2(1 - \omega_p^2/\omega_z^2) = \omega_f^2/2, \tag{3.34}$$

with the maximal value of

$$\Delta_{le} = -3\omega_z^2(1 - \omega_p^2/\omega_z^2)^2\beta_{2c}/2. \tag{3.35}$$

For the relatively low pump power $4\gamma|A_0|^2 < \Delta_{le}$, there are two intersection points with the horizontal line of $4\gamma|A_0|^2$ at ω_m (the subscript m is for MI) and ω'_f, where

$$\omega_m^2 = \omega_{le}^2(1 - \sqrt{1 - 4\gamma|A_0|^2/\Delta_{le}}), \tag{3.36}$$

$$\omega_f'^2 = \omega_{le}^2(1 + \sqrt{1 - 4\gamma|A_0|^2/\Delta_{le}}). \tag{3.37}$$

This indicates two regions of instability with boundary $(0, \omega_m)$ and (ω'_f, ω_f). The maximal growth rates in both ranges are $\gamma|A_0|^2$ at ω_{mc} and ω_{fc}, respectively, where

$$\omega_{mc}^2 = \omega_{le}^2(1 - \sqrt{1 - 2\gamma|A_0|^2/\Delta_{le}}), \tag{3.38}$$

$$\omega_{fc}^2 = \omega_{le}^2(1 + \sqrt{1 - 2\gamma|A_0|^2/\Delta_{le}}). \tag{3.39}$$

If the pump power continues to decrease, a comparison of Fig. 3-3 with 3-1 indicates that the first region reduces to the conventional MI discussed in Sec. 3.2. In fact, one can prove that the instability range approaches the conventional form of $\omega_m \sim 2\sqrt{\gamma|A_0|^2/|\beta_2(\omega_0)|}$, where $\beta_2(\omega_0)$ is actually the second-order dispersion coefficient at the pump frequency from Eq. (3.31) (see Fig. 3-2). The growth rate is also approximated by the conventional expression. This is expected since the linear phase-mismatch Δ_l is approximated by the conventional form of $-\beta_2(\omega_0)\omega^2$ within this instability range. [This can be deduced from the Taylor expansion $\Delta_l(\omega) \simeq \Delta_l''(0)\omega^2/2$, where $\Delta_l''(0) = -2\beta_2(\omega_0)$ from the definition of Δ_l and β_2.]

The second region can be shown to reduce to the conventional FWM instability. For a weak pump power, $\omega_f - \omega_f' \sim \omega_{le}\gamma|A_0|^2/\sqrt{2}\Delta_{le}$ and $\Delta_l(\omega) \sim (-4\sqrt{2}\Delta_{le}/\omega_{le})(\omega - \omega_f)$ in the range (ω_f', ω_f). Recall that for a conventional FWM of a pump wave at ω_0 and the two daughter wave at about $\omega_0 \pm \omega_f$, the linear wave-number mismatch and instability bandwidth is $\Delta v_g^{-1}(\omega - \omega_f)$ and $4\gamma|A_0|^2/|\Delta v_g^{-1}|$, respectively, where $\Delta v_g^{-1} \equiv \beta'(\omega_0 - \omega_f) - \beta'(\omega_0 + \omega_f)$ is the difference of the inverse group-velocities between the two daughter waves (the prime means derivative). We have obtained exactly these forms considering $\Delta v_g^{-1} = \Delta'(\omega_f) = -4\sqrt{2}\Delta_{le}/\omega_{le}$. The growth rate also takes the conventional form. We know that in the presence of conventional MI, a long optical pulse will break up to form solitons, but in our case, a competing process of the conventional FWM will channel the energy into the sidebands at approximately ω_f. These sidebands will beat to form high-repetition-rate short pulses; however, this is a reversible process at the nonlinear stage[62] because after pump depletion, the sidebands' energy will be transferred back to the pump.

If we increase the pump power, the two regions begin to merge as ω_m and ω_f' come closer until they coincide at ω_{le} for the power corresponding to $4\gamma|A_0|^2 = \Delta_{le}$ (ω_f does not change with power). After that, the instability range is locked at $(0, \omega_f)$ independent of power increase. The two peaks of the gain curve with a value of $\gamma|A_0|^2$ are still separated since ω_{mc} and ω_{fc} are different, but if the power continues to increase, they also coincide at ω_{le} when $2\gamma|A_0|^2 = \Delta_{le}$. After that, the $\Delta_l(\omega)$ curve has no intersection with the horizontal line at $2\gamma|A_0|^2$; thus, the maximum growth rate is smaller than $\gamma|A_0|^2$ and is given by Eq. (3.29). At even higher powers it is approximately $\sqrt{\gamma|A_0|^2\Delta_{le}}$. The peak is locked at ω_{le}, independent of power increase.

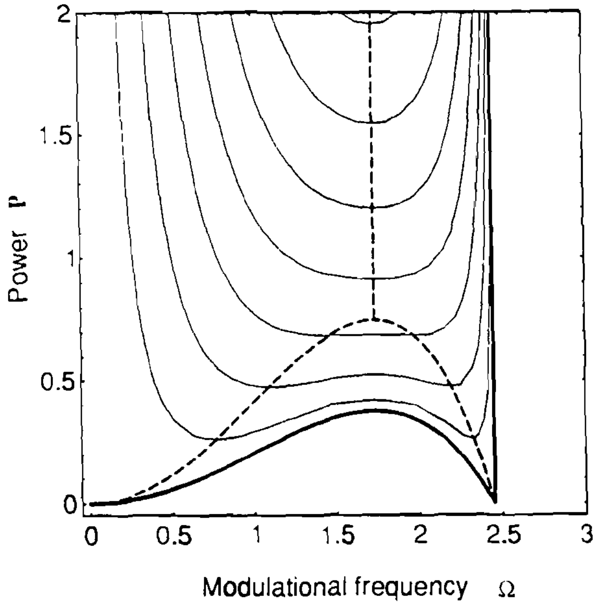

Figure 3-4: The instability region in Ω-P space for a dispersion-flattened fiber. The thick lines and the vertical axis enclose the instability region. Within this region, the dashed lines are the position of the peak-growth frequency for varying power. The background curves are the contour plots of the growth rate from Eq. (3.41).

Using the analytical expressions for ω_{mc}, ω_m, ω_f', ω_{fc}, and ω_f, the above analysis is graphically displayed in Fig. 3-4, indicating the instability region and the ridge of peak growth in a contour plot of the growth rate versus frequency and power. To reduce the number of free parameters, normalized units were introduced. We normalized ω as $\Omega = \omega/(\omega_z\sqrt{1-\omega_p^2/\omega_z^2})$, β_{2e} as $\beta_{2en} = \beta_{2e}\omega_z^2(1-\omega_p^2/\omega_z^2)^2$, $\gamma|A_0|^2$ as $P = \gamma|A_0|^2/|\beta_{2en}|$, and the growth rate as $G = \mathrm{Im}(k)/|\beta_{2en}|$.

Thus, in the normalized units, all the formulas can be rewritten with the formal substitution of $\omega_p = 0$, $\beta_{2e} = \text{sign}(\beta_{2e}) = -1$, $\omega_z = 1$, $\gamma|A_0|^2 = P$ and $\omega = \Omega$. For example, Eq. (3.32) becomes

$$\Delta_l(\Omega) = -\text{sign}(\beta_{2e})(1 - \Omega^2/6)\Omega^2. \tag{3.40}$$

From Eq. (3.27),

$$G = \text{Im}\sqrt{(\Delta_l(\Omega) - 2P)^2 - (2P)^2} \Big/ 2 \ . \tag{3.41}$$

Equations (3.33)-(3.39) become $\Omega_f^2 = 6$, $\Omega_{lc}^2 = 3$, $\Delta_{le} = -\text{sign}(\beta_{2e})3/2$, $\Omega_m^2 = 3(1-\sqrt{1 + \text{sign}(\beta_{2e})8P/3})$, $\Omega_f'^2 = 3(1+\sqrt{1 + \text{sign}(\beta_{2e})8P/3})$, $\Omega_{mc}^2 = 3(1-\sqrt{1 + \text{sign}(\beta_{2e})4P/3})$, and $\Omega_{fc}^2 = 3(1 + \sqrt{1 + \text{sign}(\beta_{2e})4P/3})$, respectively. Notice that Ω and P are now the only free parameters to change. The peak growth rate versus power is displayed in Fig. 3-5 by using $G_{\text{max}} = P$ and $G_{\text{max}} = \sqrt{-(3/2 - 2P)^2 + (2P)^2}/2$ [from Eq. (3.29)] for the ranges of $P \leq 3/4$ and $P > 3/4$, respectively. Notice that the peak growth rate increases more slowly for higher power because of the incomplete compensation of the linear and nonlinear phase-mismatches. Figure 3-6 displays the gain curves at different powers from Eqs. (3.40) and (3.41).

3.3.2 $\beta_{2e} > 0$ case

While it is true that most dispersion-flattened fibers have $\beta_{2e} < 0$, it is interesting to consider the case in which β_{2e} is a positive number since our analysis can be used to analyze dispersion curves with any shape. This situation corresponds to a pump propagating in the normal dispersion region bounded by anomalous dispersion regions in frequency space. Following the procedure developed above, we display the instability analysis based on $\Delta_l(\omega)$ in Fig. 3-7.

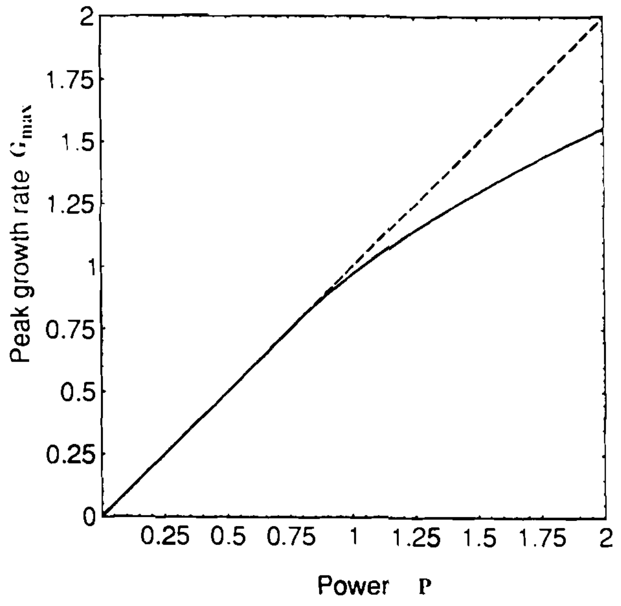

Figure 3-5: Peak growth rate $G_{\max}$ versus power P. The point where the deviation from the straight line occurs corresponds to the bifurcation point on the dashed line in Fig. 3-4. $G_{\max}$ increases with P more slowly after this point because there is not enough linear wave-number mismatch to compensate the nonlinear part.

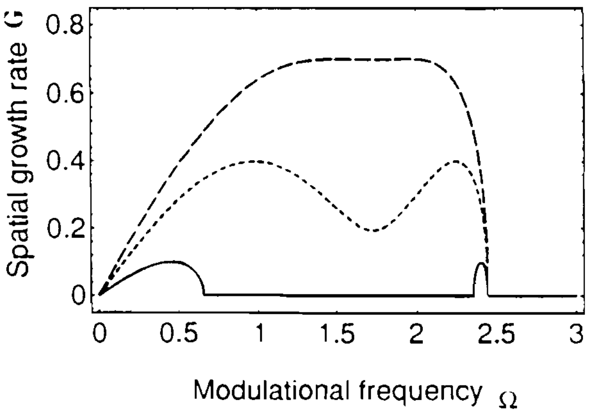

Figure 3-6: Growth rate G versus frequency Ω for different powers. The long dashed line, short dashed line, and solid line correspond to $P = 0.7$, 0.4, and 0.1, respectively. For low power, the instability is a superposition of a conventional MI instability (left portion of the solid line) and a conventional FWM instability (right portion of the solid line).

Its two zero points are at $\omega = 0$ and ω_f given by Eq. (3.33). Again, the zero of linear mismatch at nonzero ω indicates the possible presence of FWM instability. This is true as shown in Fig. 3-7 since ω_f', the intersection point with the horizontal line of $4\gamma|A_0|^2$, always exists and is also given by Eqs. (3.35) and (3.37) for $\beta_{2e} > 0$.

Unlike in the previous case, the instability corresponding to the ordinary MI does not exist due to the normal dispersion at the pump frequency. The existing instability reduces to the conventional FWM instability at small input power. As the power increases, the peak growth rate is always $\gamma|A_0|^2$ because of complete linear and nonlinear wave-number compensation. The instability region, between ω_f and ω_f' given by Eqs. (3.33) and (3.37), keeps increasing with increasing power. The instability region based on these equations and growth rate versus frequency

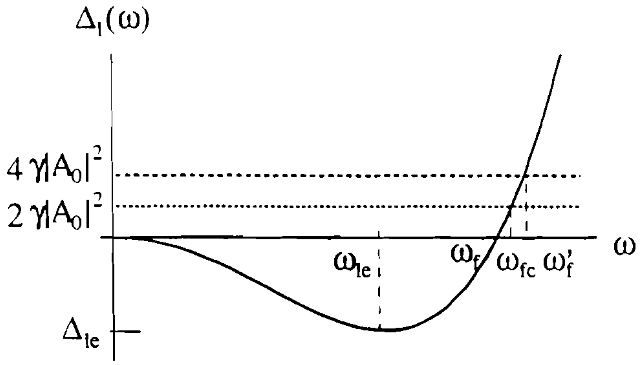
$\Delta_l(\omega)$
$4\gamma|A_0|^2$
$2\gamma|A_0|^2$
ω_{le}
ω_f
ω_{fc}
ω_f'
ω
Δ_{le}

Figure 3-7: The instability analysis using $\Delta_l(\omega)$ for $\beta_{2e} > 0$. The upper and lower dashed horizontal lines are $4\gamma|A_0|^2$ and $2\gamma|A_0|^2$, respectively. The frequency range of instability corresponds to the section of the $\Delta_l(\omega)$ curve between the horizontal axis and the upper dashed horizontal line, i.e., (ω_f, ω_f'). The intersection of the curve with the lower dashed horizontal line at ω_{fc} indicates the frequency of maximal growth rate $\gamma|A_0|^2$. As power increases, both horizontal lines go up.

by Eq. (3.27) are shown in Figs. 3-8 and 3-9.

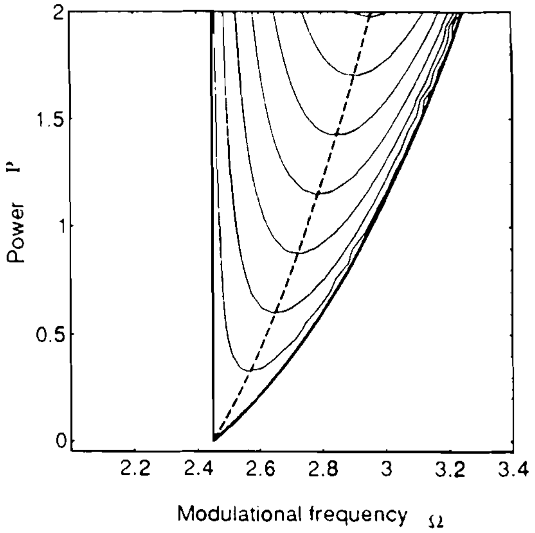

Figure 3-8: Same as Fig. 3-4 except for the sign of β_{2e}. The thick lines enclose the instability region. Within the region, the dashed line is the position of the peak-growth frequency for varying power. The peak growth rate is always P. The background curves are the contour plots of the growth rate from Eq. (3.41).

Although we have found instability with the pump in the normal dispersion region, it can be proved that at least one of the unstable sidebands is located in the anomalous dispersion region on the $\beta_2(\omega')$ curve.

In summary, the instability behavior in the weak power limit is determined by the analytical properties of $\Delta_l(\omega)$ near the frequencies for which it equals zero. If its first derivative is a nonzero value at such a frequency, which leads to a finite group velocity difference between the linearly phase-matched sidebands, then we have a conventional FWM instability close to that frequency. If the first derivative is also zero, which means equal group velocity for the linear phase-matched

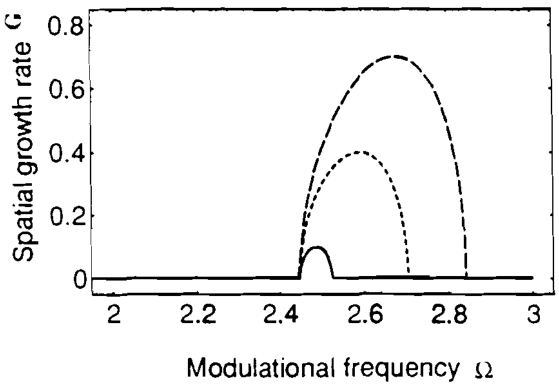

Figure 3-9: Same as Fig. 6 except for the sign of β_{2e}. For low power, it is a conventional FWM instability.

sidebands, then we have stability or conventional MI (close to that frequency) depending on whether its second derivative is negative or positive, respectively.

We now briefly consider a fiber with many alternating dispersion regions (in frequency space). Based upon the above analysis, it is easy to predict instabilities for such a fiber: usually, more instability regions corresponding to FWM will be added to the above pictures because of the oscillating behavior of $\Delta_l(\omega)$. These regions can merge at high pump power. Thus the scheme can produce continuum generation with a wide bandwidth.

3.3.3 Frequency-dependent nonlinearity

In the above analysis we neglected the dependence of γ on the modulational frequency and took it to be a real quantity. At large ω, the Raman effects come into play, and this assumption is invalid. In order to describe the dependence of the nonlinear coefficients on the modulational frequency, a standard model is to assume the nonlinearity comes from an instantaneous electronic response which does not depend on the modulational frequency, plus a retarded nonlinearity that can be described by the simple Lorentzian model for the Raman effect. Thus we can write,

$$\chi^{(3)}(\omega_1, \omega_2, \omega_3) = \chi_I^{(3)} + \chi_R^{(3)}(\omega_1, \omega_2, \omega_3). \tag{3.42}$$

According to the Lorentzian model,[11] the Raman part takes the familiar forms

$$\chi_R^{(3)}[\omega_0, -\omega_0, (\omega_0 \pm \omega)] = (1/2)[\chi_{R0}^{(3)}/(1 - \omega^2/\omega_R^2 \mp i2\nu_R\omega/\omega_R^2) + \chi_{R0}^{(3)}] \tag{3.43}$$

$$\chi_R^{(3)}[\omega_0, \omega_0, -(\omega_0 \pm \omega)] = \chi_{R0}^{(3)}/(1 - \omega^2/\omega_R^2 \pm i2\nu_R\omega/\omega_R^2), \tag{3.44}$$

$$\chi_R^{(3)}[\omega_0, -\omega_0, \omega_0] = \chi_{R0}^{(3)}. \tag{3.45}$$

where ω_R and ν_R are the Raman peak frequency and dissipation rate, respectively. $\chi_I^{(3)}$ and $\chi_{R0}^{(3)}$ are parameters for the magnitude of the instantaneous and retarded nonlinearity, respectively. Note that $\chi^{(3)}(\omega_0, -\omega_0, \omega_0) = \chi_I^{(3)} + \chi_{R0}^{(3)}$.

From Eq. (3.9), we have

$$\gamma[\omega_0, -\omega_0, (\omega_0 \pm \omega)] \simeq 6\pi\omega_0\chi^{(3)}[\omega_0, -\omega_0, (\omega_0 \pm \omega)]/[cn(\omega_0)A_{\text{eff}}], \tag{3.46}$$

$$\gamma[\omega_0, \omega_0, -(\omega_0 \pm \omega)] \simeq 6\pi\omega_0\chi^{(3)}[\omega_0, \omega_0, -(\omega_0 \pm \omega)]/[cn(\omega_0)A_{\text{eff}}],. \tag{3.47}$$

where we have kept the ω dependence only in $\chi^{(3)}$ since $(\omega_0 \pm \omega)/n(\omega_0 \pm \omega) \simeq \omega_0/n(\omega_0)$ in the range of the modulational frequency under consideration.

When combined with Eqs. (3.46) and (3.47), equations (3.42)-(3.45) allow us to find $\gamma_{x\pm}$ and $\gamma_{f\pm}$ from their definitions in Eqs. (3.14)-(3.17):

$$\gamma_{x\pm} = \gamma_{f\pm} = \gamma_I + \gamma_{R0}/(1 - \omega^2/\omega_R^2 \mp i2\nu_R\omega/\omega_R^2), \tag{3.48}$$

where $\gamma_{R0} = 6\pi\omega_0\chi_{R0}^{(3)}/[cn(\omega_0)A_{\text{eff}}]$ and $\gamma_I = 6\pi\omega_0\chi_I^{(3)}/[cn(\omega_0)A_{\text{eff}}]$. Note the nonlinear coefficient for zero modulational frequency is $\gamma(\omega_0, -\omega_0, \omega_0) = \gamma_I + \gamma_{R0}$, which is a real number and will be denoted by γ. By using Eq. (3.21), the dispersion relation including Raman effect is,

$$\begin{aligned} k_\pm &= (1/2)[\beta(\omega_0 + \omega) - \beta(\omega_0 - \omega) \pm \\ &\sqrt{(\Delta_l - 2\gamma_{x+}|A_0|^2)^2 - (2\gamma_{x+}|A_0|^2)^2}], \end{aligned} \tag{3.49}$$

where γ_{x+} is given by Eq. (3.48). It is easy to show that for very small modulational frequency, $\gamma_{x+} \simeq \gamma$, thus the result for instantaneous nonlinearity is recovered.

As a numerical example, let us suppose that the two points of zero dispersion of the dispersion-flattened fiber are 150 nm apart and the pump frequency is 50 nm from the extreme-dispersion frequency. This corresponds to $\omega_z/(2\pi) \sim 22.5$ THz and $\omega_p/(2\pi) \sim 15$ THz. The FWM frequency will be $\omega_f/(2\pi) \sim 41$ THz, according to Eq. (3.33). Assuming that the extremum of the second-order dispersion $\beta_{2e} \sim -1$ ps^2/km, and $\gamma \sim 10$ W^{-1}km^{-1}, then the power for the merging of conventional MI and FWM is $|A_0|^2 = \Delta_{le}/(4\gamma) \sim 231$ W. This power is greatly reduced if the dispersion-flattened range is narrower or the magnitude of the second-order dispersion is smaller. The Raman frequency is about $\omega_R \sim 2\pi \times 13$ THz. As representative values, $\nu_R \sim 2\pi \times 5$ THz, $\gamma_I \sim 0.6\gamma$, and $\gamma_{R0} \sim 0.4\gamma$. Figure 3-10 shows the Raman effect on the gain curve obtained from Eq. (3.49) for the above parameters. By the normalization scheme used before, the frequency Ω, the growth rate G, and the power P have been normalized to $2\pi \times 16.7$ THz (the normalized Raman frequency is thus 0.78), 6.16 m^{-1} and 616 W, respectively.

Another aspect of the Raman effect can be revealed by a computation of

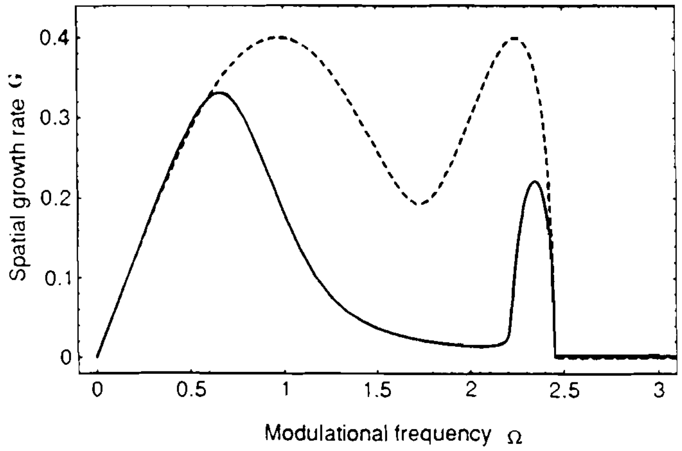

Figure 3-10: Growth rate G versus frequency Ω for a fixed power $P = 0.4$. The Raman parameters are $\gamma_{R0} = 0.4\gamma$, $\gamma_I = 0.6\gamma$ and $\nu_R = 0.38\omega_R$. The normalized Raman frequency is $\omega_R/[\omega_z(1 - \omega_p^2/\omega_z^2)^{1/2}] = 0.78$. The dashed line corresponds to the instantaneous nonlinearity.

$|r_+(\omega)|^{-1}$ from Eq. (3.19), resulting in a value smaller than unity (Fig. 3-11). This means that in the presence of Raman effect, the amplitude of the Stokes wave is larger than that of the anti-Stokes for the unstable mode, which is expected since the Raman gain tends to amplify the Stokes sideband while decreasing the anti-Stokes sideband.

3.4 Conclusions

In conclusion, we studied MI by linearization around a nonlinear steady-state solution of the (nonlinear) Maxwell equation system. This steady-state solution corresponds to a cw pump. Specifically, the resulting linear partial differential equation is solved by harmonic analysis. In essence, the solution to this linear partial differential equation is a multiscale approximation in which the small parameter is

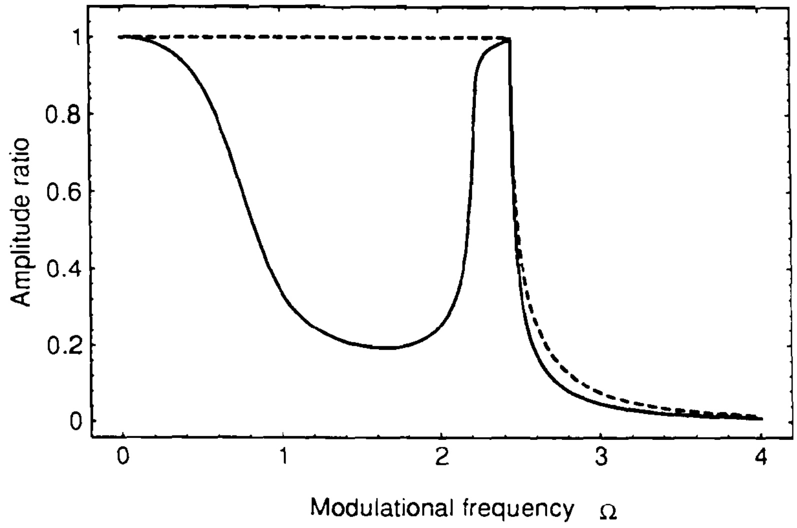

Figure 3-11: The amplitude ratio $|r_-|^{-1}$ of the anti-Stokes and the Stokes wave for the growing mode. The parameters are the same as those of Fig. 7. The dashed line indicates that in the absence of the Raman effect, the ratio is unity in the instability region.

the pump amplitude. Thus, unlike the traditional NSE-type of methods, which involve Taylor expansions in frequency space, our result can be uniformly applied in any frequency range. Nonlinear dispersion and non-parametric effects such as Raman gain are formally included. We applied our results to various dispersion-flattened fibers to study the effects of the shape of the modal dispersion curve on MI. We found that when the fiber is flattened in the anomalous dispersion region, the instability is the superposition of a conventional MI and FWM at low pump power. These instability regions in frequency space merge at large power. Instability also occurs even when the pump is in the normal dispersion region if this region of the dispersion curve is flattened. At low pump powers the instability reduces to the conventional FWM instability. The frequency positions, the bandwidth, the maximum growth rate of the instability for various pump powers, etc., were characterized analytically. The Raman effect on these parametric instabilities was also studied. It changes the growth rate of the instability and makes the Stokes sideband stronger than the anti-Stokes sideband.

Chapter 4

Instability from Cross-Phase Modulation in the Normal Dispersion Region

4.1 Introduction

The propagation of two intense light waves that have different frequencies. in a single-mode optical fiber. in usually studied within the framework of coupled nonlinear Schrodinger equations (NSE's). These equations have been used to predict several interesting phenomena.[12] including the cross-phase-induced modulational instability in the normal-dispersion regime.[9,41,42] Although such an instability has been observed when cross-phase modulation occurs between the two polarization components of a single wave, no such instability has ever been observed by using two pump waves that have the same polarization, but different frequencies. Two assumptions made in the derivation of the coupled NSE's are that the waves have narrow spectra centered on their respective carrier frequencies and that the coherent FWM interaction between two incident waves can be neglected.[43,44] The self-consistency of the predicted phenomena and these assumptions must always be checked.

An alternative approach to nonlinear wave interactions has been developed by Zakharov.[46,47] This approch does not require the wave spectra to be narrow or the nonlinear coupling to be independent of frequency. It has been to the study of several instabilities in the fluids and plasmas,[46,47,58,63] and is well suited to the study of the aforementioned optical interaction. Such an analysis shows that cross-phase modulation is not a sufficient condition for the existence of instability in the normal-dispersion regime. Specifically, the importance of the effects of cross-phase modulation depends on the form of the dispersion curve and the incident-wave frequencies.

Let us consider a single mode fiber with linear dispersion relationship $\beta(\omega)$. The mode-coupling, or Zakharov, equation[46,47] takes the form

$$\begin{aligned}\partial_z A(\omega,z) - i\beta(\omega)A(\omega,z) = i\int\int\int \gamma(\omega,\omega',\omega'',\omega''')\\ A^*(\omega',z)A(\omega'',z)A(\omega''',z)\delta(\omega+\omega'-\omega''-\omega''')d\omega' d\omega'' d\omega''',\end{aligned} \tag{4.1}$$

where $\beta(\omega)$ is the linear wavenumber corresponding to the frequency ω. To within a factor of order unity that depends on the transverse mode structure, the nonlinear coupling coefficient is given, in electrostatic units, by

$$\gamma(\omega;\omega',\omega'',\omega''') = \frac{2\pi\omega\chi^{(3)}(\omega;\omega',\omega'',\omega''')}{cn(\omega)A_{\text{eff}}} \tag{4.2}$$

where $n(\omega)$ is the refractive index of the fiber and A_{eff} is its core area.[12] In the limit of narrow bandwidth, the Zakharov equation 4.1 reduces to the NSE. Both equations require nonlinearity to be weak and to produce spatial variation of the

Fourier amplitudes on a scale long compared to an optical wavelength.

4.2 Harmonic analysis

Suppose that the input field is given by

$$\begin{aligned} A(\omega,0) &= \sqrt{P_1}[\delta(\omega-\omega_1)+\delta(\omega+\omega_1)] \\ &+ \sqrt{P_2}[\delta(\omega-\omega_2)+\delta(\omega+\omega_2)], \end{aligned} \tag{4.3}$$

corresponding to two pump waves of peak "power" $2P_1$ and $2P_2$. Without loss of generality, $\omega_1 < \omega_2$. The evolution of A with distance is determined by the Zakharov equation (1.1). Because the input Fourier spectrum is discrete, the integrations in the Zakharov equation reduce to summations. A simple analysis of this equation shows that the nonlinear terms on the right-hand side are of two types: incoherent self- and cross-phase modulation terms, which produce nonlinear wavenumber shifts at the input frequencies, and coherent coupling terms, which transfer energy to other frequencies, such as $3\omega_2$, $2\omega_2+\omega_1$ and $2\omega_2-\omega_1$.

Since the generated waves all require a considerable distance to grow to finite amplitude, the initial evolution of the input field can be determined by retaining in the Zakharov equation only those Fourier components associated with the two pump frequencies. At the frequency ω_1, the Zakharov equation reduces to

$$[d_z - i\beta(\omega_1)]A(\omega_1,z) = i\gamma(P_1+2P_2)A(\omega_1,z), \tag{4.4}$$

where a degeneracy factor of 3 has been included in definition (4.2) and $\gamma(\omega_1;\omega_1,\omega_2,-\omega_2)$ has been assumed comparable to $\gamma(\omega_1;\omega_1,\omega_1,-\omega_1)$. Throughout this chapter, γ will be assumed to depend only weakly on frequency and its arguments will be omitted for simplicity of notation. Should the need arise, it is not difficult to extend the analysis of this paper to include the frequency dependence of γ as was done for one pump wave in Chapter 3. The solution of Eq. (4.4) is

$$\begin{aligned} A(\omega_1, z) &= \sqrt{P_1}\exp\left[i\phi_1(z)\right], \\ \phi_1(z) &= \beta(\omega_1)z + \gamma(P_1 + 2P_2)z \end{aligned} \tag{4.5}$$

A similar analysis shows that

$$\begin{aligned} A(\omega_2, z) &= \sqrt{P_2}\exp[i\phi_2(z)], \\ \phi_2(z) &= \beta(\omega_2)z + \gamma(2P_1 + P_2)z \end{aligned} \tag{4.6}$$

Solutions (4.5) and (4.6) represent two pump waves with nonlinear wavenumber shifts and are valid near the entrance to the fiber. When the amount of energy transferred to the generated waves is small, they are also globally-valid equilibrium solutions of the Zakharov equation. Due to the frequency dependence of the refractive index, this condition is usually satisfied for third-harmonic and sum-frequency generation. However, the generation of light at the difference frequency $2\omega_2 - \omega_1$, which is close to ω_2 if the incident frequencies are not too dissimilar, warrants further investigation. From the Zakharov equation,

$$\begin{aligned} [d_z - i\beta(2\omega_2 - \omega_1)]A(2\omega_2 - \omega_1, z) &= i\gamma P_2\sqrt{P_1}\exp\left[i2\phi_2(z) - i\phi_1(z)\right] \\ &+ i2\gamma(P_1 + P_2)A(2\omega_2 - \omega_1, z) \end{aligned} \tag{4.7}$$

In the undepleted pump-wave approximation, the solution of Eq. (4.7) is facilitated by writing

$$A(2\omega_2 - \omega_1, z) = B(z)\exp\left[i\beta(2\omega_2 - \omega_1)z + i2\gamma(P_1 + P_2)z\right] \tag{4.8}$$

It follows immediately that

$$B(z) = (\gamma P_2\sqrt{P_1}/\delta\beta)[\exp(i\delta\beta z) - 1], \tag{4.9}$$

where

$$\delta\beta = 2\beta(\omega_2) - \beta(\omega_1) - \beta(2\omega_2 - \omega_1) - \gamma(2P_2 - P_1) \tag{4.10}$$

is the total (linear plus nonlinear) wavenumber mismatch of this particular generation process. Thus, the energy transfer due to pump-pump FWM will be minimal provided that

$$\left|\frac{2\gamma P_2}{2\beta(\omega_2) - \beta(\omega_1) - \beta(2\omega_2 - \omega_1) - \gamma(2P_2 - P_1)}\right| \ll 1. \tag{4.11}$$

Inequality (4.11) requires the wavenumber-mismatch (4.10) to be much larger than the nonlinear coupling term in Eq. (4.7) to suppress difference-frequency generation. When this condition is satisfied, the nonlinear term can be omitted from the denominator of inequality (4.11). A similar inequality follows from the consideration of light generation at the difference frequency $2\omega_1 - \omega_2$.

Suppose that inequality (4.11) is satisfied and, hence, that Eqs. (4.5) and (4.6) describe an equilibrium solution of the Zakharov equation. To study the stability of this equilibrium, one should linearize the Maxwell and polarization equations underlying the Zakharov equation around the equilibrium solution. To the order of accuracy of the Zakharov equation, this procedure is equivalent to linearizing the Zakharov equation itself. However, one can avoid a formal linearization of the Zakharov equation by using harmonic analysis: Due to the intrinsic linearity of the stability analysis, any perturbation of the equilibrium can be decomposed into small-amplitude waves at various frequencies. Consequently, one only needs to study the evolution of each group of small-amplitude waves. These waves are referred to as "sidebands" of the pump waves because the frequencies of any unstable group are close to the pump frequencies, as will be demonstrated.

Consider the evolution of a probe wave of frequency $\omega_1 + \omega$. Suppose first that $\omega \gg \omega_2 - \omega_1$. In this case, the interaction of the probe and pump waves produces harmonics whose amplitudes are much smaller than the probe amplitude. Although the probe wave is subject to a nonlinear wavenumber shift, its energy is essentially undepleted. This harmonic generation is similar to that described above, except that the probe wave contributes one of the driving components on the right-hand side of the Zakharov equation.

Conversely, suppose that $\omega \sim \omega_2 - \omega_1$. In this case, some of the generated waves can be nearly phase matched. One example is the wave generated at the frequency $\omega_1 + \omega_2 - (\omega_1 + \omega) = \omega_2 - \omega \approx \omega_2$. For these waves, the wavenumber-mismatch terms are comparable to, or smaller than, the nonlinear coupling terms. Hence, they can be driven to amplitudes as large as the probe amplitude. In turn, these generated waves modify the probe wave. Consequently, the evolution of the entire group of waves must be determined self-consistently. Notice that this scenario automatically includes the previous scenario as a special case.

The second scenario is now considered in detail. Suppose that the probe wave has frequency $\omega_1 + \omega$, where $|\omega| < (\omega_2 - \omega_1)/2$. Only those sidebands at the frequencies $\omega_1 - \omega$, $\omega_2 + \omega$ and $\omega_2 - \omega$ can be driven near-resonantly, unless special arrangements are made to allow other FWM processes to occur. This situation is illustrated in Fig. 4-1.

When $(\omega_2 - \omega_1)/2 < |\omega| < 3(\omega_2 - \omega_1)/2$, the interaction is identical to the preceding interaction. To see this, suppose that $\omega > (\omega_2 - \omega_1)/2$ and define $\omega' = (\omega_2 - \omega_1) - \omega$. Then $\omega_1 + \omega = \omega_2 - \omega'$, with $|\omega'| < (\omega_2 - \omega_1)/2$, and the

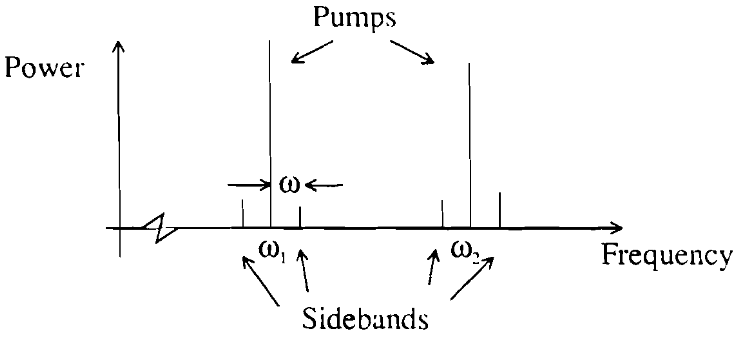

Figure 4-1: Fourier spectrum of the electric field. The large peaks represent the two pump waves, whereas the four small peaks represent the four sidebands whose evolution is coupled by the nonlinearities in the Zakharov equation (4.1).

probe wave should be regarded as a sideband of the higher-frequency pump wave (unless, of course, the pump waves are orthogonally polarized). However, the physics of the interaction is unaltered, as stated. When $|\omega| > 3(\omega_2 - \omega_1)/2$, the other sidebands are usually driven nonresonantly and, hence, the interaction is usually stable. Consequently, in the following analysis, the frequency difference between the probe and the lower-frequency pump wave is assumed to satisfy the inequality

$$|\omega| < (\omega_2 - \omega_1)/2. \tag{4.12}$$

The derivation of the sideband evolution equations from the Zakharov equation is straightforward. Just as the pump waves are subject to nonlinear wavenumber shifts, so also are the sidebands. In anticipation of these wavenumber shifts, it is convenient to define

$$
\begin{aligned}
A(\omega_1+\omega, z) &= B_{1+}\exp\left[ikz+i\phi_1(z)\right],\\
A(\omega_1-\omega, z) &= B_{1-}\exp\left[-ik^*z+i\phi_1(z)\right],\\
A(\omega_2+\omega, z) &= B_{2+}\exp\left[ikz+i\phi_2(z)\right],\\
A(\omega_2-\omega, z) &= B_{2-}\exp\left[-ik^*z+i\phi_2(z)\right].
\end{aligned}
\tag{4.13}
$$

The sideband equations then take the form

$$
\begin{aligned}
D_{1+}(\omega, k)B_{1+} &= \gamma P_1(B_{1+}+B^*_{1-})+2\gamma\sqrt{P_1P_2}(B_{2+}+B^*_{2-}),\\
D_{1-}(\omega, k)B^*_{1-} &= -\gamma P_1(B_{1-}+B^*_{1-})-2\gamma\sqrt{P_1P_2}(B_{2+}+B^*_{2-}),\\
D_{2+}(\omega, k)B_{2+} &= \gamma P_1(B_{2+}+B^*_{2-})+2\gamma\sqrt{P_1P_2}(B_{1+}+B^*_{1-}),\\
D_{2-}(\omega, k)B^*_{2-} &= -\gamma P_1(B_{2+}+B^*_{2-})-2\gamma\sqrt{P_1P_2}(B_{1+}+B^*_{1-})
\end{aligned}
\tag{4.14}
$$

where the dispersion functions

$$
\begin{aligned}
&D_{1+}(\omega, k) = k-\beta(\omega_1+\omega)+\beta(\omega_1),\\
&D_{1-}(\omega, k) = k+\beta(\omega_1-\omega)-\beta(\omega_1),\\
&D_{2+}(\omega, k) = k-\beta(\omega_2+\omega)+\beta(\omega_2),\\
&D_{2-}(\omega, k) = k+\beta(\omega_2-\omega)-\beta(\omega_2).
\end{aligned}
\tag{4.15}
$$

The physical significance of these equations can be seen as follows: Suppose that the nonlinear terms in Eqs. (4.5) and (4.14) are absent. Then, from the second of Eqs. (4.5) and the first of Eqs. (4.13) - (4.15),

$$
A(\omega_1+\omega, z) = B_{1+}\exp[i\beta(\omega_1)z+ikz]
\tag{4.16}
$$

where

$$
k = \beta(\omega_1+\omega)-\beta(\omega_1)
\tag{4.17}
$$

and the probe wave propagates with its natural wavenumber. Thus, the term $\beta(\omega_1 + \omega) - \beta(\omega_1)$ is the linear mismatch between the natural wavenumber of the probe wave and the wavenumber at which it is driven by the terms on the right-hand side of the mode-coupling equation, when they are present. The four-sideband interaction described by Eqs. (4.14) and (4.15) can be unstable. The spatial growth rate of this instability depends on the nonlinear coupling between the sidebands, which tends to be destabilizing, and the intrinsic linear and nonlinear wavenumber shifts of each sideband, which tend to be stabilizing.

By combining Eqs. (4.14), one can show that

$$\begin{aligned}&[D_{1+}D_{1-} + \gamma P_1(D_{1+} - D_{1-})][D_{2+}D_{2-} + \gamma P_2(D_{2+} - D_{2-})] = \\ &\quad 4\gamma^2 P_1 P_2 (D_{1+} - D_{1-})(D_{2+} - D_{2-}).\end{aligned} \tag{4.18}$$

The solutions of this instability dispersion equation depend on the shape of the fiber dispersion curve and, in general, must be determined numerically. The relative amplitudes of the sidebands then follow from Eqs. (4.14) and (4.15). For the limit in which $\omega \ll \omega_2 - \omega_1$, Eq. (4.18) reduces to the usual dispersion equation that is derived from coupled NSE's.[9,41,42]

4.3 Results and discussion

Three different cases are illustrated in Fig. 4-2. Consider first Figs. 4-2(a) and 4-2(b), for which both pump frequencies are in the normal or anomalous dispersion regime of a conventional single-mode fiber and are not too close to the zero dispersion point. Suppose that the dispersion curve can be approximated by a parabola over the frequency range $[\omega_1 - (\omega_2 - \omega_1)/2, \omega_2 + (\omega_2 - \omega_1)/2]$. Such

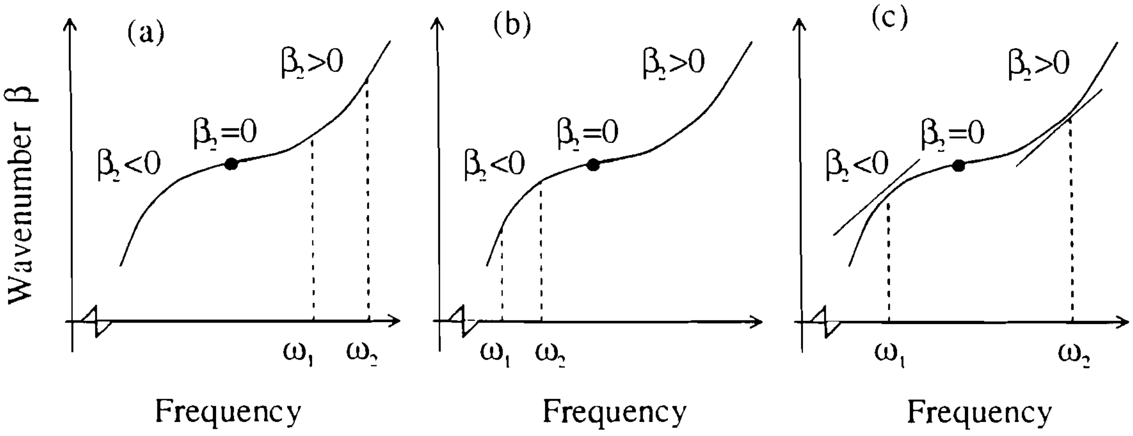

Figure 4-2: Dispersion curve of a conventional fiber. (a) Both pump frequencies are in the normal dispersion regime. (b) Both pump frequencies are in the anomalous dispersion regime. (c) One pump frequency is in the normal dispersion regime and the other pump frequency is in the anomalous dispersion regime. Notice that the pump frequencies can be chosen in such a way that the pump-wave group velocities are equal.

a parabola can be characterized by its first derivative $d\beta/d\omega = \beta_1$ and second derivative $d^2\beta/d\omega^2 = \beta_2$ evaluated at ω_1. Although this parabolic approximation cannot be made for all dispersion curves, it serves to illustrate the physics of the interaction. For equal pump powers. the dispersion equation (4.18) becomes

$$\begin{aligned}&\{[k-\beta_1\omega]^2-(\beta_2\omega^2/2)[2\gamma P+(\beta_2\omega^2/2)]\}\\&\{[k-\beta_1\omega-(\omega_2-\omega_1)\beta_2\omega]^2-(\beta_2\omega^2/2)[2\gamma P+(\beta_2\omega^2/2)]\}\\&=(4\gamma P)^2(\beta_2\omega^2/2)^2,\end{aligned}\tag{4.19}$$

while condition (4.11) for the absence of pump-pump FWM becomes

$$\left|\frac{2\gamma P}{(\omega_2-\omega_1)^2\beta_2}\right| \ll 1. \tag{4.20}$$

Analysis of Eq. (4.19) is facilitated by the change of variables

$$K = \frac{k - \beta_1 \omega}{\gamma P}, \; C = \operatorname{sign}(\beta_2), \; S = \left|\frac{(\omega_2 - \omega_1)^2 \beta_2}{2\gamma P}\right|^{1/2}, \; \Omega = \left|\frac{\beta_2 \omega^2}{2\gamma P}\right|^{1/2} > 0. \quad (4.21)$$

The parameter C is equal to 1 or -1, according to whether the pump frequencies are in the normal or anomalous dispersion regime, respectively. The other three variables have the form of wavenumber shifts divided by the nonlinear wavenumber shift imposed on each sideband by the appropriate pump wave. In terms of these dimensionless variables, Eq. (4.19) becomes

$$[K^2 - C\Omega^2(2 + C\Omega^2)][(K - 2CS\Omega)^2 - C\Omega^2(2 + C\Omega^2)] = (4\Omega^2)^2 \quad (4.22)$$

Condition (4.20) requires that $S \gg 1$ and condition (4.12) requires that $\Omega < S/2$. First, suppose that $K \sim \Omega \sim 1$. Then the second group of terms in Eq. (4.22) is of order S^2 and the modulational interactions of the two pump waves decouple. For the lower-frequency pump wave, the reduced dispersion relation is

$$K = \pm[C\Omega^2(2 + C\Omega^2)]^{1/2} \quad (4.23)$$

When $C = 1$, corresponding to normal dispersion, the lower-frequency pump wave is stable. When $C = -1$, corresponding to anomalous dispersion, the lower-frequency pump wave is modulationally unstable by itself; the effects of cross-phase modulation are insignificant. Similar results apply to the higher-frequency pump wave. The approximation used in deriving Eq. (4.23) is self-consistent whenever

$$\left|\frac{4\Omega^2}{S^2 \pm S(2C + \Omega^2)^{1/2}}\right| \ll \left|\Omega^2(2C + \Omega^2)\right|. \quad (4.24)$$

Since condition (4.24) is satisfied for all $\Omega \leq S/2$, no cross-phase-induced instability can exist. Although this result was proved for a parabolic dispersion curve, the key ingredient is that the curvature of the dispersion curve not change sign in the aforementioned frequency range. Thus, we expect the stated result to be true for conventional fibers in general. When $S \sim 1$, the preceding analysis is not valid because pump-pump FWM occurs and Eqs. (4.5) and (4.6) do not describe an equilibrium solution of the Zakharov equation. However, the wave evolution for this case has been studied numerically by Rothenberg.[45] No evidence of modulational instability was found.

Figure 4-2(c) illustrates the case in which ω_1 is in the anomalous dispersion regime and ω_2 is in the normal dispersion regime. As shown in the figure, it is always possible to find pump frequencies for which the pump-wave group velocities are equal. This situation is similar to the one analyzed by Inoue.[64] In the spirit of the cases analyzed previously, suppose that the dispersion curve is parabolic in the vicinities of both pump frequencies. Then the dispersion equation (4.18) becomes

$$[K^2 - C_1\Omega^2(2 + C_1\Omega^2)][K^2 - C_2\Omega^2(2 + C_2\Omega^2)] = (4C_1\Omega^2)(4C_2\Omega^2), \qquad (4.25)$$

where K and Ω are as defined in Eqs. (4.21) and

$$C_1 = \mathrm{sign}[\beta_2(\omega_1)] = -1, \; C_2 = \beta_2(\omega_2)/|\beta_2(\omega_1)| > 0. \qquad (4.26)$$

Since the pump frequencies are well separated, there is no reason to assume that the magnitudes of C_1 and C_2 are equal, as they were in the previous two cases.

The solutions of Eq. (4.25) can be written in the form

$$\begin{aligned} 2K^2 &= [C_1\Omega^2(2 + C_1\Omega^2) + C_2\Omega^2(2 + C_2\Omega^2)] \pm \\ &\{[C_1\Omega^2(2 + C_1\Omega^2) - C_2\Omega^2(2 + C_2\Omega^2)]^2 + 4(4C_1\Omega^2)(4C_2\Omega^2)\}^{1/2}. \end{aligned} \tag{4.27}$$

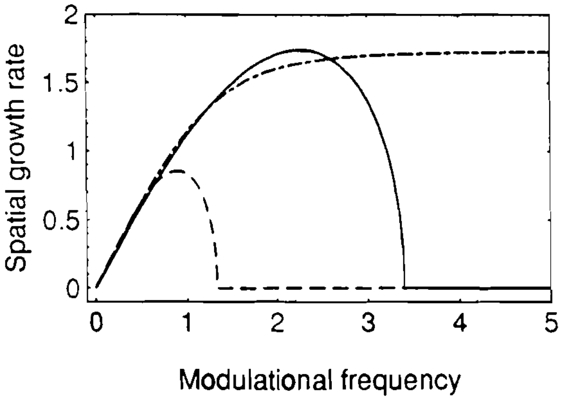

Figure 4-3: Spatial growth rate plotted as a function of the modulational frequency for the case in which one pump frequency is in the normal dispersion regime and the other pump frequency is in the anomalous dispersion regime, and the pump-wave group velocities are equal. The normalizations of the spatial growth rate and the modulational frequency are given in Eqs. (4.21). The broken line corresponds to $C_2 = 2$, the dot-dashed line corresponds to $C_2 = 1$ and the solid line corresponds to $C_2 = 0.5$.

The most unstable branch of Eq. (4.27) is displayed in Fig. 4-3, for three values of C_2. The curve corresponding to $C_2 = 1$ is particularly interesting, because it seems to imply that instability exists for arbitrary values of the modulational frequency Ω. For future reference, notice that Eq. (4.27) reduces to $K \approx \pm(\Omega^2 \pm i\sqrt{3})$ when $C_2 = 1$ and $\Omega^2 \gg 1$. To understand this result, recall that the coupled modulational instability of two pump waves, which involves four sidebands, is comprised of three distinct two-sideband interactions. The modulational instability of the lower-frequency pump wave involves B_{1+} and B_{1-}, and is characterized by the wavenumber mismatch

$$\begin{aligned}\Delta(1-,1+) &= 2\beta(\omega_1) - \beta(\omega_1+\omega) - \beta(\omega_1-\omega) \\ &\approx -\beta_2(\omega_1)\omega^2. \end{aligned} \tag{4.28}$$

A similar expression exists for the mismatch of the modulational instability of the higher-frequncy pump wave. Forward FWM involves B_{1-} and B_{2-}, and is characterized by the mismatch

$$\begin{aligned}\Delta(2-,1+) &= \beta(\omega_1) + \beta(\omega_2) - \beta(\omega_1+\omega) - \beta(\omega_2-\omega) \\ &\approx [\beta_1(\omega_2) - \beta_1(\omega_1)]\omega - [\beta_2(\omega_2) + \beta_2(\omega_1)]\omega^2/2. \end{aligned} \tag{4.29}$$

This interaction can be unstable. Bragg reflection involves B_{1+} and B_{2+}, is characterized by the mismatch

$$\begin{aligned}\Delta(2+,1+) &= \beta(\omega_2) + \beta(\omega_1+\omega) - \beta(\omega_1) - \beta(\omega_2+\omega) \\ &\approx -[\beta_1(\omega_2) - \beta_1(\omega_1)]\omega - [\beta_2(\omega_2) - \beta_2(\omega_1)]\omega^2/2 \end{aligned} \tag{4.30}$$

and is intrinsically stable. For the case under discussion, only forward FWM is (linearly) phase matched when $\Omega^2 \gg 1$ and must be responsible for the predicted instability. The associated matching condition (4.29) is illustrated by Fig. 4-4.

This argument can be quantified: If one retains only B_{1+} and B_{2-} in Eqs.

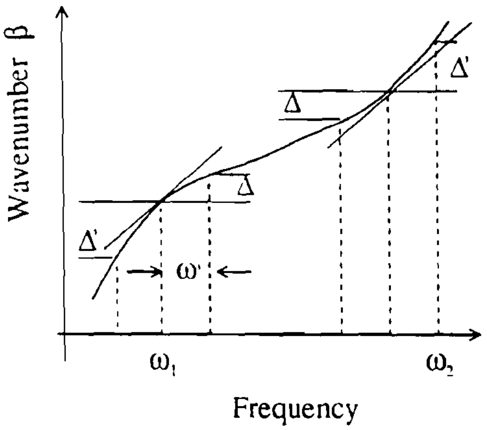

Figure 4-4: Wavenumber matching condition illustrated for the case in which one pump frequency is in the normal dispersion regime and the other pump frequency is in the anomalous dispersion regime. The pump-wave group velocities are equal and $C_2 = 1$.

(4.14), one obtains the dispersion equation

$$[K - (1 + C_1\Omega^2)][K + (1 + C_2\Omega^2)] = -4, \tag{4.31}$$

which has the solution

$$K = (C_1 - C_2)\Omega^2/2 \pm i\{4 - [1 + (C_1 + C_2)\Omega^2/2]^2\}^{1/2}. \tag{4.32}$$

When $C_2 = 1$, $K = -\Omega^2 \pm i\sqrt{3}$ in agreement with the corresponding limit of Eq. (4.27). Having analyzed this two-sideband interaction quantitatively, one can now understand the stated result physically: When $C_2 = 1$, the dispersion curvatures associated with the frequencies $\omega_1 + \omega$ and $\omega_2 - \omega$ are equal and opposite, and the (linear) wavenumber mismatch is identically zero for all values of ω. This degeneracy can be removed by retaining ω^3 terms in the matching condition (4.29). The other two curves in Fig. 4-3 correspond to coupled modulational instabilities. To see this, simply observe that neither curve has the precise shape required by Eq. (4.32), or by Eq. (4.23). [For the case in which $C_2 = 0.5$, the spatial growth rate predicted by Eq. (4.32) is a reasonable approximation to the exact growth rate in the range $\Omega > 3$.] Even though Eq. (4.32) does not predict these two curves accurately, one can still use it to gain some insight into the difference between them: When $C_2 = 2.0$, the linear and nonlinear mismatch terms in Eq. (4.32) reinforce one another, whereas, when $C_2 = 0.5$, they oppose one another over a limited range of modulational frequencies. This observation is consistent with the fact that the range of modulational frequencies corresponding to instability is larger for the latter case than for the former. For cases in which $0 < |C_1| - C_2 \ll 1$, the linear mismatch term cancels the nonlinear mismatch term when the modulational frequency is large: Eq. (4.32) is relevant and the peak spatial growth rate of the instability is 2, rather than $\sqrt{3}$.

Now suppose that the pump-wave group velocities are unequal. Then the four-sideband interaction is governed by

$$\begin{aligned}[K^2 - C_1\Omega^2(2 + C_1\Omega^2)][(K - 2S\Omega)^2 - C_2\Omega^2(2 + C_2\Omega^2)]& \\ = (4C_1\Omega^2)(4C_2\Omega^2),& \qquad (4.33)\end{aligned}$$

where

$$S = \frac{\beta_1(\omega_2) - \beta_1(\omega_1)}{|2\gamma P \beta_2(\omega_1)|^{1/2}} \qquad (4.34)$$

characterizes the difference between the pump-wave group velocities. Forward FWM is described by Eq. (4.31), with $C_2\Omega^2$ replaced by $-2S\Omega + C_2\Omega^2$. Correspondingly, Eq. (4.32) becomes

$$K = S\Omega + (C_1 - C_2)\Omega^2/2 \pm i\{4 - [1 - S\Omega + (C_1 + C_2)\Omega^2/2]^2\}^{1/2} \tag{4.35}$$

It is evident from Eq. (4.33) that the modulational interactions of the two pump waves decouple when $|S| \gg 1$ and $\Omega^2 \sim 1$: the lower-frequency pump wave is modulationally unstable by itself, whereas the higher-frequency pump wave is modulationally stable. Since Eq. (4.33) is not biquadratic in K, it has no simple solutions to facilitate study of the regime in which $\Omega \gg 1$. However, it is clear from Eqs. (4.28) - (4.30) that the modulational instabilities of each pump wave are not (linearly) phase matched, and that forward FWM and Bragg reflection cannot be (linearly) phase matched simultaneously. Thus, only a forward FWM instability can exist, subject to the requirement that the dispersion coefficients have different magnitudes. Notice that the wavenumber matching condition (4.29) requires the modulational frequency to have a definite sign; symmetric Stokes and anti-Stokes emission cannot occur. This conclusion also follows from Eq. (4.35). When Ω is positive, Eq. (4.35) corresponds to the interaction of B_{1+} and B_{2-}, as stated previously. When Ω is negative, Eq. (4.35) corresponds to the interaction of B_{1-} and B_{2+}. It has already been demonstrated that cross-phase-induced instability exists when $S = 0$. By continuity, we expect that cross-phase-induced instability can exist when $S \sim 1$, over a limited range of Ω. However, Eq. (4.33) must be solved numerically to obtain quantitative results.

In related work, Schadt and Jaskorzynska[65] considered the interaction of a strong pump pulse, propagating in the normal dispersion regime, and a weak continuous signal wave, propagating in the anomalous dispersion regime with a group velocity comparable to that of the pump pulse. By numerically solving a pair of

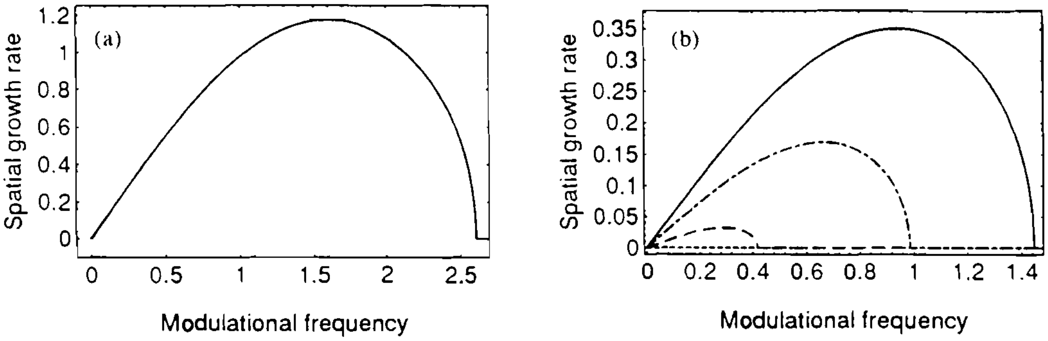

Figure 4-5: Spatial growth rate plotted as a function of the modulational frequency for the case in which one pump frequency is in the normal dispersion regime and the other pump frequency is in the anomalous dispersion regime. The normalizations of the spatial growth rate and the modulational frequency are given in Eqs. (4.39). The pump-wave group velocities are equal and $C_2/C_1 = -1.4$. (*a*) The power ratio of the lower-frequency to the higher-frequency pump wave $R = 1$. (*b*) The solid line corresponds to $R = 0.25$, the upper dot–dashed line corresponds to $R = 0.16$, the broken line corresponds to $R = 0.11$ and the lower dot–dashed line corresponds to $R = 0.09$.

coupled NS equations, they showed that the cross-phase modulation imposed by the pump pulse on the signal wave induced the formation of a short signal pulse, even though the pump pulse had an intrinsic tendancy to broaden and the signal wave was too weak to be modulationally unstable by itself. This effect has been demonstrated experimentally by Greer *et al.*[20] The most unstable branch of Eq. (4.27) is displayed in Fig. 4-5(a), for $C_2/C_1 = -1.4$, the ratio used by Schadt and Jaskorzynska in their numerical simulations. Since the peak spatial growth rate of the instability and the range of modulational frequencies corresponding to instability are both larger than those of the modulational instability of the lower-frequency pump wave by itself [see Eq. (4.23)], the results of this paper are similar to those of Schadt and Jaskorzynska. However, a fairer comparison of the results requires a study of the cross-phase-induced instabilities for the case in which the lower-frequency pump wave is much weaker than the higher-frequency pump wave. The details of such an analysis are given in the Appendix. The main results are twofold: When instability exists, the peak growth rate of the cross-phase-induced instability is larger than that of the modulational instability of the lower-frequency pump wave by itself, for most values of the pump-wave intensity ratio. However, no instability exists when the pump-wave intensity ratio is less than a certain critical value. These results are illustrated by Fig. 4-5(b). The latter result differentiates the physics of the instabilities of two continuous waves and the interaction of a continuous wave and a short pulse.

The frequency dependence of the natural wavenumber in a dispersion-flattened fiber[12] is shown in Fig. 4-6. There are two frequency domains in which the fiber exibits normal dispersion, separated by a domain in which the fiber exhibits anomalous dispersion. The analysis of the cases in which one pump frequency is in the domain of anomalous dispersion and the other pump frequency is in either

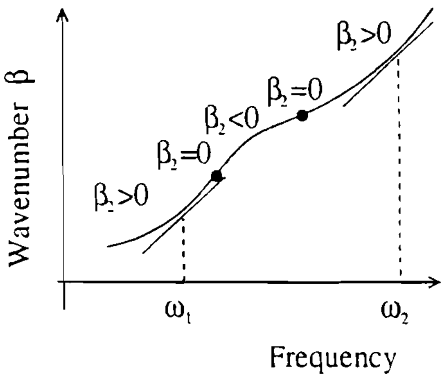

Figure 4-6: Dispersion curve of a dispersion-flattened fiber. The two pump frequencies are in separate normal dispersion regimes. Notice that the pump frequencies can be chosen in such a way that the pump-wave group velocities are equal.

of the two domains of normal dispersion is identical to the corresponding analysis for light-wave propagation in a conventional fiber. Hence, it need not be discussed further. Figure 4-6 illustrates the case in which the pump frequencies are in separate domains of normal dispersion. It is clear from the figure that the pump frequencies can be chosen in such a way that the pump-wave group velocities are equal. The dispersion equation for this situation is Eq. (4.25), with $C_1 = 1$ and $C_2 > 0$. For the special case in which $C_2 = 1$, a cross-phase-induced modulational instability is known to occur.[41,42] However, since the pump frequencies are well separated, there is no reason to assume that the dispersion coefficients are equal. The spatial growth rate of the coupled modulational instability is displayed in Fig. 4-7, for three values of C_2. Varying C_2 alters the peak growth rate of the instability and the range of frequencies corresponding to instability. The latter effect can be understood qualitatively by regarding $(C_1+C_2)/2$ as the effective dispersion coefficient; increasing the effective dispersion coefficient reduces the range of unstable wavenumbers, whereas reducing the effective dispersion coefficient increases the range of unstable wavenumbers, as is the case for a single modulationally unstable wave. However, the coupled modulational instability is less sensitive to the value of C_2 than are the instabilities associated with Fig. 4-2(c). In particular, there is no distinct forward FWM instability when $C_2 = 1$. This result also follows from Eq. (4.29).

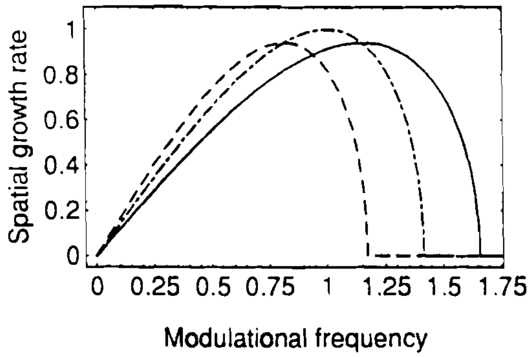

Figure 4-7: Spatial growth rate plotted as a function of the modulational frequency for the case in which the two pump frequencies are in separate normal dispersion regimes and the pump-wave group velocities are equal. The normalizations of the spatial growth rate and the modulational frequency are given in Eqs. (4.3). The solid line corresponds to $C_2 = 0.5$, the dot-dashed line corresponds to $C_2 = 1.0$ and the broken line corresponds to $C_2 = 2.0$.

Now suppose that the pump-wave group velocities are unequal. Then the four-sideband interaction is governed by Eq. (4.33), with S as defined in Eq. (4.34), $C_1 = 1$ and $C_2 > 0$. The interaction of B_{1+} and B_{2-} is governed by Eq. (4.35). Suppose, temporarily, that $C_2 = 1$. The dispersion equation for this case is mathematically equivalent to Eq. (4.22). It follows immediately that, when $|S| \gg 1$ and $\Omega \sim 1$, the modulational interactions of the two pump waves decouple and both pump waves are modulationally stable. When $\Omega \gg 1$, further analysis is required. Fortunately, the dispersion equation has the exact solution

$$\begin{aligned}(K - S\Omega)^2 &= \Omega^2(2C + \Omega^2) + (S\Omega)^2 \\ &\pm\{(4\Omega^2)^2 + 4(S\Omega)^2[\Omega^2(2C + \Omega^2)]\}^{1/2}\end{aligned} \tag{4.36}$$

from which it follows that the condition

$$S^2 - 2C - 4 < \Omega^2 < S^2 - 2C + 4 \tag{4.37}$$

must be satisfied for instability to exist. From the discussion following Eq. (4.35), it follows that this instability is forward FWM. The agreement between the predictions of Eqs. (4.35) and (4.36) is evident in Fig. 4-8 and confirms the preceding assertion. In the present case, solutions (4.35) and (4.36) are meaningful because B_{1+} and B_{2-} are physically distinct from the two pump waves. One need only check that the modulational frequency is not so large that the Taylor expansion of the natural wavenumber, used in the derivation of Eqs. (4.22) and (4.33), is invalid. Previously, Ω was assumed to be positive. No generality was lost in this assumption due to the symmetry of the frequencies of the four interacting sidebands. When S is positive, the mismatch terms in Eq. (4.35) cancel for $\Omega \approx S$. This cancellation results in a peak spatial growth rate of 2, as shown in Fig. 4-8(a). (In contrast, when $C_2 = -1$ such a cancellation does not occur and the peak spatial growth rate is $\sqrt{3}$.) When S is negative, the mismatch terms do not cancel, and the interaction of B_{1+} and B_{2-} is not phase matched. However, by changing the sign of the modulational frequency in Eq. (4.29), one can show that the interaction of B_{1-} and B_{2+} is phase matched. This change is equivalent to changing the sign of Ω in Eq. (4.35) and also results in a peak spatial growth rate of 2, as shown in Fig. 4-8(b). When $C_2 \neq 1$, solution (4.36) is no longer relevant. However, the decoupling of the two modulational interactions when $\Omega \sim 1$ is not sensitive to the value of C_2 and still occurs. The forward FWM instability is still governed by Eq. (4.35).

In other types of dispersive media, it is possible for the pump frequencies to be in separate anomalous dispersion regimes. In this case, both pump waves are modulationally unstable by themselves. Cross-phase modulation couples the single-pump instabilities to produce a two-pump instability that has a larger spatial growth rate than either of the single-pump instabilities.[41,42] The analysis of this case is similar to that described in the preceding two paragraphs, as are the conclusions.

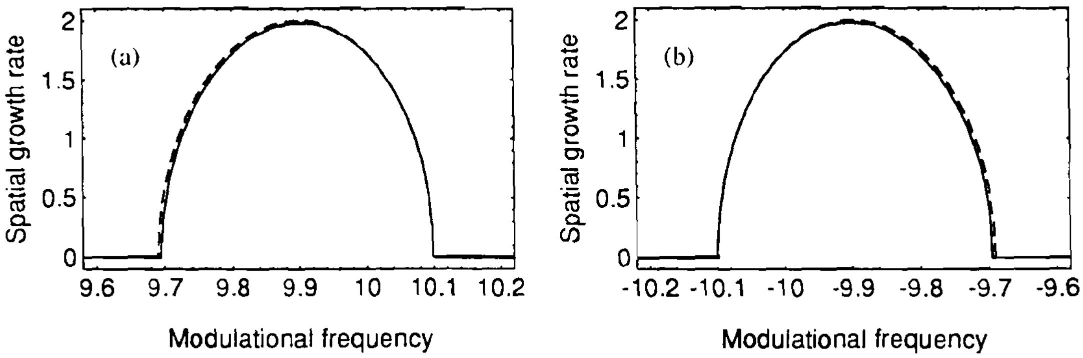

Figure 4-8: Spatial growth rate plotted as a function of the modulational frequency for the case in which the two pump frequencies are in separate normal dispersion regimes and the pump-wave group velocities are unequal. The normalizations of the spatial growth rate and the modulational frequency are given in Eqs. (4.3). The solid line corresponds to the exact result (4.36), whereas the broken line corresponds to the approximate result (4.35). (*a*) $S = 10$. (*b*) $S = -10$.

4.4 Conclusions

The method of Zakharov was used to study instabilities induced by cross-phase modulation in a single-mode fiber. This method is valid for differences between the pump and sideband frequencies that are larger than those allowed in the usual NS analysis. Contrary to the predictions of coupled NS equations, the existence of cross-phase modulation does not guarantee the existence of instability.

If both pump frequencies are in the normal dispersion regime of a conventional fiber, there is no instability. If both pump frequencies are in the anomalous dispersion regime, the pump waves are modulationally unstable by themselves, but do not cooperate to produce a coupled MI. For dispersive media in general, a sufficient condition for the existence of a (four-sideband) coupled MI is that the difference between the pump-wave group velocities can be made small without producing pump-pump FWM. This situation can arise in a conventional fiber when the two pump frequencies are in different dispersion regimes (normal and anomalous).

The dispersion curve associated with a dispersion-flattened fiber has two regions in which dispersion is normal, separated by a region in which dispersion is anomalous. Coupled MI can also occur in a dispersion-flattened fiber when the two pump frequencies are in different normal dispersion regimes and the pump-wave group velocities are comparable.

In each type of fiber, the coupled MI is suppressed by the presence of a large difference in the pump-wave group velocities. However, cross-phase modulation can still induce a (two-sideband) FWM instability.

The central theme of this chapter is how dispersion controls which of the three constituent two-sideband interactions are phase matched for a particular value of the modulational frequency. With dispersive effects replaced by geometric (diffractive) effects, this theme is also relevant to transverse instabilities of two copropagating light waves. These instabilities are analyzed in detail in[41, 42] and.[66–68]

4.5 Appendix: Unequal pump-wave powers

It follows from Eq. (4.18) and the assumption that the dispersion curve is parabolic in the neighborhoods of the pump frequencies, that the dispersion equation for the four-sideband instability is

$$[K^2 - C_1\Omega^2(2R + C_1\Omega^2)][K^2 - C_2\Omega^2(2 + C_2\Omega^2)] = R(4C_1\Omega^2)(4C_2\Omega^2) \quad (4.38)$$

where

$$\begin{aligned} &K = \tfrac{k-\beta_1\omega}{\gamma P_2}, \Omega = |\tfrac{\omega^2\beta_2(\omega_2)}{2\gamma P_2}|^{1/2} > 0, R = \tfrac{P_1}{P_2}, \\ &C_2 = \mathrm{sign}[\beta_2(\omega_2)], C_1 = \beta_2(\omega_1)/|\beta_2(\omega_2)|. \end{aligned} \quad (4.39)$$

All quantities in Eq. (4.38) were normalized relative to those associated with the higher-frequency pump wave, because the comparison of this instability analysis with the work of Schadt and Jaskorzynska[65] is facilitated by holding P_2 fixed while P_1 is varied. The solution of Eq. (4.38) is

$$\begin{aligned} 2K^2 = &[C_1\Omega^2(2R + C_1\Omega^2) + C_2\Omega^2(2 + C_2\Omega^2)] \\ &\pm\{[C_1\Omega^2(2R + C_1\Omega^2) - C_2\Omega^2(2 + C_2\Omega^2)]^2 + 4R(4C_1\Omega^2)(4C_2\Omega^2)\}^{1/2} \end{aligned} \quad (4.40)$$

As mentioned in the Summary, there are many similarities between modulational instabilities in which the linear wavenumber mismatches (4.28) – (4.30) are due to dispersion and those in which the linear wavenumber mismatches are due to diffraction. In particular, the dependence of the spatial growth rate of the coupled modulational instability on the pump-wave power ratio was studied in Refs.,[41,66,68] for the analogs of the cases in which both pump frequencies are in the normal or anomalous dispersion regime. The dependence of the spatial growth rate of the FWM instability on the pump-wave power ratio was studied in Refs.[9,66,68] Consequently, these cases need not be discussed herein.

For the case in which $C_2 = 1$ and $C_1 < 0$, it was determined empirically that instability occurs when the term in braces in Eq. (4.40) is negative. A necessary and sufficient condition for this to happen is that

$$7 + 4\sqrt{3} > |C_1 R| > 7 - 4\sqrt{3}. \tag{4.41}$$

For Fig. 4-5, $C_1 = -0.714$. Correspondingly, the second of inequalities (4.41) predicts that instability will occur when the pump-wave power ratio exceeds 0.100, in agreement with the figure. Further analysis of Eq. (4.40) shows that the second of inequalities (4.41) is a sufficient condition for instability, for all negative values of C_1.

Chapter 5

Modulational Instabilities of Counterpropagating Waves in a Finite Dispersive Kerr Medium

5.1 Introduction

The nonlinear interaction between counterpropagating waves in a finite Kerr medium has been been studied extensively[11,49,69-71] because of its relevance to many practical optical devices such as optical gyroscopes, lasers, fiber interferometers, and various bistable switches. Such an interaction exhibits rich nonlinear dynamics ranging from bistability to optical chaos since the Kerr nonlinearity tends to destabilize the steady-state propagation of the counterpropagating pump waves.

Instabilities are classified into two categories known as convective and absolute. Even for a Kerr medium without group-velocity dispersion (GVD), an absolute temporal instability of the counterpropagating pump waves can occur in the presence of boundary reflections, which effectively form a Fabry-Perot (FP) cavity.[69] This instability has been shown to be an FP-cavity version of Ikeda instability that was first found in a ring cavity for a unidirectional pump wave[72] and can be explained in terms of the amplification of the sidebands of the pump wave due to four-wave mixing (FWM). Of course, dispersive effects will come into play at higher temporal frequencies of the perturbation. In recent years, considerable attention has been paid to studying the effects of GVD on optical instabilities occurring in Kerr media. It is well known that the spectral sidebands of a unidirectional pump wave can be amplified by the convective temporal modulational instability (MI) due to the combined effect of FWM and anomalous dispersion.[12] This MI can become absolute inside a ring cavity because of the feedback provided by the cavity.[73-76] In fact, MI lasers have been proposed and demonstrated[22-25] for the ring-cavity configuration. Like the temporal GVD effects, the spatial diffractive effects have also been considered for the ring cavity.[77,78]

Compared with the case of a ring cavity with a unidirectional pump wave, the inclusion of GVD effects in a finite medium with counterpropagating pump waves is more difficult, mainly because the nonlinear interaction involves two pairs of sidebands (one pair for each pump wave). Such an interaction is induced by GVD, self-phase modulation (SPM) and cross-phase modulation (XPM). Previous work has found that even when the boundary reflections are neglected, the counterpropagating pump waves in a finite medium can become absolutely unstable.[49,70,71] However, the treatment was quite involved mathematically and did not provide physical insight since an eigenvalue problem in a four-dimensional vector space had to be solved numerically. Consequently, the studies were limited to the special case of identical pump waves with only small differences in power. It is thus desirable to establish a simpler model that gives a clear physical picture and, at the same time, provide analytical result for the more general case of unequal pump powers. Moreover, it is not clear how the instability would be affected by the weak boundary reflections that always exist in practice. The nonlinear dynamics can become more intriguing in such a case since the boundary reflections provide additional coupling between the two pair of sidebands.

This chapter is a comprehensive analytical study of the combined effects of four-sideband coupling, GVD, and boundary reflections in a counterpropagating system. Although a silica fiber is used as an example, the results are applicable to any dispersive Kerr medium. A new perturbation method applied to this problem results in a physically transparent model in terms of a doubly-resonant parametric oscillator for a photon-pair that allows simplification and characterization of the complex system in a familiar language. The general result can be interpreted in analogy to a detuned distributed-feedback waveguide subject to boundary reflections. Analytical expression for the instability threshold and growth rate are obtained naturally. In the special case of antireflecting boundaries and equal counterpropagating pump powers, our results agree with the previous numerical results. However, the effects of boundary reflections are shown to be important. In the low-frequency limit in which dispersion effects are negligible, our results reduce to those for the Ikeda instability. At high frequencies, dispersive effects lead to new instabilities both in the normal and anomalous regions. In particular, it is shown that the absolute modulational instability dominates in the anomalous dispersion regime.

The chapter is organized as follows. In Sec. 5.2, we carry out a linear stability analysis of the coupled nonlinear Schrödinger equations (NSE's) that describe the propagation of the counterpropagating pump waves in a dispersive Kerr medium. The theoretical model is completed in Sec. 5.3 when the boundary conditions are incorporated and the parameter regions are classified. The results are used in Sec. 5.4 to discuss the instability for the case of weak or anti-reflection boundaries. Sections 5.5 and 5.6 are devoted to the strong reflection case, above the instability threshold and below it, respectively. The main results are summarized in Sec. 5.7.

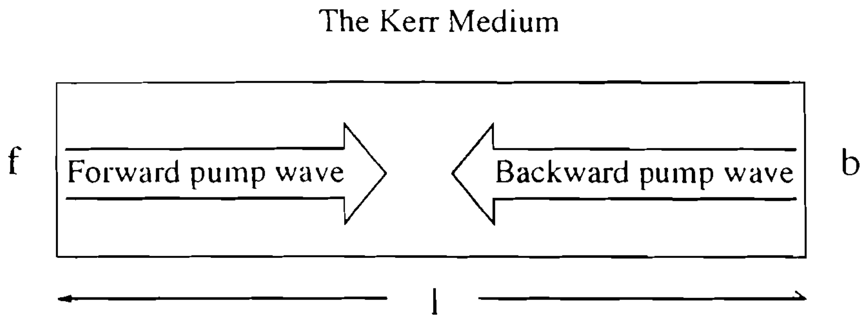

Figure 5-1: Schematic illustration of a finite dispersive Kerr medium of length l and the two counterpropagating pump waves. The front and back surface are labeled as f and b, respectively.

5.2 General solution

The system under investigation is illustrated Fig. 5-1, where two counterpropagating pump waves exist in a dispersive Kerr medium of length l with front (left) boundary "f" and back (right) boundary "b". In the scalar wave approximation, the nonlinear interaction of two counterpropagating optical waves in a dispersive Kerr medium is described by the coupled NSE's[12]

$$
\begin{aligned}
i\partial_z A_1 &= -i\beta_1\partial_t A_1 + \frac{1}{2}\beta_2\partial_{tt}^2 A_1 - \gamma(|A_1|^2 + 2|A_2|^2)A_1, && (5.1)\\
-i\partial_z A_2 &= -i\beta_1\partial_t A_2 + \frac{1}{2}\beta_2\partial_{tt}^2 A_2 - \gamma(|A_2|^2 + 2|A_1|^2)A_2, && (5.2)
\end{aligned}
$$

where z and t are the spatial and temporal coordinates, and β_1^{-1}, β_2 and γ are the group velocity, GVD coefficient, and nonlinear coefficient, respectively. $A_1(t,z)$ and $A_2(t,z)$ are the complex envelopes of the forward and backward propagating waves and are related to the corresponding phasors of the fields by

$$E_1(t,z) = A_1(t,z)e^{ik_0 z}, \tag{5.3}$$

$$E_2(t,z) = A_2(t,z)e^{ik_0(l-z)}, \tag{5.4}$$

where the subscripts 1 and 2 refer to forward and backward propagating waves, respectively. k_0 is the linear wavenumber of the counterpropagating waves, and l is the length of the Kerr medium. The constant phase phase factor $\exp(ik_0 l)$ has been factored out for later convenience, and the fields have been normalized so that $|A_1|^2$ and $|A_2|^2$ represent the powers of the two beams.

The counterpropagating cw pump fields in the medium correspond to the steady-state solution of Eqs. (5.1) and (5.2) given by

$$A_{1s}(t,z) = A_{10}e^{i\gamma(|A_{10}|^2+2|A_{20}|^2)z}, \tag{5.5}$$

$$A_{2s}(t,z) = A_{20}e^{i\gamma(|A_{20}|^2+2|A_{10}|^2)(l-z)}, \tag{5.6}$$

where the constants $A_{10} = |A_{10}|\exp(i\phi_{10})$ and $A_{20} = |A_{20}|\exp(i\phi_{20})$ contain both the amplitude and phase information for the two counterpropagating waves in the medium. However, only their phase difference $\phi_{20} - \phi_{10}$ is of significance because we can always assume without loss of generality that one of the phases is zero.

We study the stability of the steady-state solution by performing a standard linear stability analysis. For this purpose, we perturb the steady state slightly and write the respective perturbations for the two pump waves as

$$\delta A_1(t, z) = \overline{\delta A_1}(t, z) e^{i\gamma(|A_{10}|^2 + 2|A_{20}|^2) z}, \tag{5.7}$$

$$\delta A_2(t, z) = \overline{\delta A_2}(t, z) e^{i\gamma(|A_{20}|^2 + 2|A_{10}|^2)(l - z)}. \tag{5.8}$$

By inserting $A_1 = A_{1s} + \delta A_1$ and $A_2 = A_{2s} + \delta A_2$ into Eqs. (5.1) and (5.2), the linearized equations for $\overline{\delta A_1}(t, z)$ and $\overline{\delta A_2}(t, z)$, written in the frequency domain, are

$$\begin{aligned}
&(i\partial_z + \beta_1\omega + \beta_2\omega^2/2 + \gamma|A_{10}|^2)\delta A_1(\omega, z) \\
&+\gamma[A_{10}^2 \delta A_1^*(-\omega, z) + 2A_{10}A_{20}^* \delta A_2(\omega, z) + 2A_{10}A_{20}\delta A_2^*(-\omega, z)] = 0, &(5.9)\\
&(-i\partial_z - \beta_1\omega + \beta_2\omega^2/2 + \gamma|A_{10}|^2)\delta A_1^*(-\omega, z) \\
&+\gamma[A_{10}^{*2} \delta A_1(\omega, z) + 2A_{10}^* A_{20}\delta A_2^*(-\omega, z) + 2A_{10}^* A_{20}^* \delta A_2(\omega, z)] = 0, &(5.10)\\
&(-i\partial_z + \beta_1\omega + \beta_2\omega^2/2 + \gamma|A_{20}|^2)\delta A_2(\omega, z) \\
&+\gamma[A_{20}^2 \delta A_2^*(-\omega, z) + 2A_{20}A_{10}^* \delta A_1(\omega, z) + 2A_{20}A_{10}\delta A_1^*(-\omega, z)] = 0, &(5.11)\\
&(i\partial_z - \beta_1\omega + \beta_2\omega^2/2 + \gamma|A_{20}|^2)\delta A_2^*(-\omega, z) \\
&+\gamma[A_{20}^{*2} \delta A_2(\omega, z) + 2A_{20}^* A_{10}\delta A_1^*(-\omega, z) + 2A_{20}^* A_{10}^* \delta A_1(\omega, z)] = 0. &(5.12)
\end{aligned}$$

where $\delta A_1(\omega, z)$ and $\delta A_2(\omega, z)$ are the Fourier transforms of $\overline{\delta A_1}(t, z)$ and $\overline{\delta A_2}(t, z)$, respectively.

The standard technique used to solve linear equations leads to the following general form of solution for $\delta A_1(\omega, z)$, $\delta A_1^*(-\omega, z)$, $\delta A_2(\omega, z)$ and $\delta A_2^*(-\omega, z)$ in Eqs.

(5.9)-(5.12):

$$\begin{pmatrix} \delta A_1(\omega, z) \\ \delta A_1^*(-\omega, z) \\ \delta A_2(\omega, z) \\ \delta A_2^*(-\omega, z) \end{pmatrix} = e^{ik_{1+}z} \begin{pmatrix} 1 \\ r_{1+} \\ e_{1++} \\ e_{1+-} \end{pmatrix} c_1 + e^{ik_{1-}z} \begin{pmatrix} r_{1-} \\ 1 \\ e_{1-+} \\ e_{1--} \end{pmatrix} c_2$$
$$+ e^{ik_{2+}(l-z)} \begin{pmatrix} e_{2++} \\ e_{2+-} \\ 1 \\ r_{2+} \end{pmatrix} c_3 + e^{ik_{2-}(l-z)} \begin{pmatrix} e_{2-+} \\ e_{2--} \\ r_{2-} \\ 1 \end{pmatrix} c_4. \tag{5.13}$$

where the arbitrary constants c_1, c_2, c_3 and c_4 represent the magnitudes of the four independent eigenmodes of the solution while the rest of the coefficients are functions of the modulational frequency ω. The k's are the propagation constants determined by the dispersion relations for the eigenmodes, and the coupling coefficients r's and e's are the relative amplitudes of the four sidebands [$\delta A_1(\omega, z)$, $\delta A_1^*(-\omega, z)$, $\delta A_2(\omega, z)$, and $\delta A_2^*(-\omega, z)$] for the corresponding eigenmodes.

It is generally difficult to get the exact analytical expression for the dispersion relations and other coefficients in Eq. (5.13). For this reason, numerical studies have been performed in the past.[49,70,71] However, we show in the following that approximate analytical expressions can be obtained with sufficiently high precision.

Before writing down the approximate analytical expressions, we introduce several characteristic lengths and frequencies. The walkoff length and the GVD length at a given modulation frequency ω are defined as $l_W = (\beta_1\omega)^{-1}$ and $l_D = (\beta_2\omega^2)^{-1}$. Note that the walkoff length for two counterpropagating waves is simply the spatial scale of envelope variation of the fields. Without loss of generality, we assume the power ratio $S \equiv |A_{20}|^2/|A_{10}|^2 \leq 1$ (i.e. the power of the backward pump wave is equal to or less than the forward one). The nonlinear length at a given power of the forward pump wave, $P = |A_{10}|^2$, is defined as $l_N = (\gamma|A_{10}|^2)^{-1}$. We further define $\omega_W = \gamma P/\beta_1$ and $\omega_D = \sqrt{\gamma P/\beta_2}$ to represent the required modulational frequencies at which the walkoff length and the dispersion length are equal to the nonlinear length, respectively. For modulational frequencies below ω_W and ω_D, the effects of walkoff and GVD are not important, respectively.

The ratio $\epsilon = \omega_W/\omega_D = \sqrt{|\beta_2|\gamma P/\beta_1^2}$ is a small quantity if the power and the GVD coefficient are not too large. Even for materials with relatively large GVD coefficients and at relatively high powers, this ratio is still quite small since, in practice, the GVD effect is simply negligible when the walkoff length is comparable to the nonlinear length. In this paper, the dispersive nonlinear effects are of primary concern, thus the normalized modulational frequency $\Omega = \omega/\omega_D$ and normalized length $L = l/l_N$ are often used. This means that the GVD effects are negligible when $\Omega \ll 1$, in which case the Kerr medium can be treated as dispersionless ($\beta_2 = 0$). Another ratio, $\epsilon_\Omega = l_W/l_D = \Omega\epsilon$, represents the relative importance of GVD and the walkoff at a given modulational frequency. This is also a small quantity since $\Omega \ll 1/\epsilon$ is usually satisfied.

Using silica fiber as an illustrative example,[12] we assume a forward-pump power of $P = 1$ kW, a nonlinear coefficient of $\gamma = 10$ W^{-1}km^{-1}, a group velocity of $1/\beta_1 = 0.2$ mm/ps, and a GVD coefficient of $|\beta_2| = 20$ ps^2/km. Then, $l_N \sim 10$ cm. Although we have chosen a case of high power with large nonlinear coefficient as the example, ϵ is only 10^{-4}. ω_W and ω_D are ~ 2 ns^{-1} (320 MHz) and ~ 20 ps^{-1} (3.2 THz), respectively. Even for a large modulational frequency of ~ 40 ps^{-1} (6.4 THz), ϵ_Ω is only $\sim 10^{-3}$.

By treating ϵ and ϵ_Ω as small parameters, we obtain the following analytical expressions for the coefficients in Eq. (5.13). The dispersion relations can be written as

$$k_{1\pm}(\omega) \approx \beta_1\omega \pm Y_1(\omega), \tag{5.14}$$

$$k_{2\pm}(\omega) \approx \beta_1\omega \pm Y_2(\omega), \tag{5.15}$$

with

$$Y_1(\omega) = \sqrt{(\beta_2\omega^2/2 + \gamma|A_{10}|^2)^2 - (\gamma|A_{10}|^2)^2}, \tag{5.16}$$

$$Y_2(\omega) = (A_{10} \rightarrow A_{20}). \tag{5.17}$$

The other coefficients are given by

$$r_{1+}(\omega) \approx (Y_1 - \beta_2\omega^2/2 - \gamma|A_{10}|^2)/(\gamma A_{10}^2), \tag{5.18}$$

$$r_{1-}(\omega) \approx (Y_1 - \beta_2\omega^2/2 - \gamma|A_{10}|^2)/(\gamma A_{10}^{*2}), \tag{5.19}$$

$$r_{2\pm}(\omega) \approx (A_{10}, Y_1 \rightarrow A_{20}, Y_2), \tag{5.20}$$

$$e_{1++}(\omega) \approx -(Y_1 - \beta_2\omega^2/2)A_{20}/(\beta_1\omega A_{10}), \tag{5.21}$$

$$e_{1+-}(\omega) \approx (Y_1 - \beta_2\omega^2/2)A_{20}^*/(\beta_1\omega A_{10}), \tag{5.22}$$

$$e_{1-+}(\omega) \approx -(Y_1 - \beta_2\omega^2/2)A_{20}/(\beta_1\omega A_{10}^*), \tag{5.23}$$

$$e_{1--}(\omega) \approx (Y_1 - \beta_2\omega^2/2)A_{20}^*/(\beta_1\omega A_{10}^*), \tag{5.24}$$

$$e_{2\pm\pm}(\omega) \approx (A_{10}, Y_1 \rightarrow A_{20}, Y_2). \tag{5.25}$$

The procedure leading to the above expressions consists of solving Eqs. (5.9) and (5.10) for $\delta A_1(\omega, z)$ and $\delta A_1^*(-\omega, z)$ by first assuming $\delta A_2(\omega, z) = 0$ and $\delta A_2^*(-\omega, z) = 0$. Thus, the dispersion relation $k_{1\pm}(\omega)$ and coupling coefficients $r_{1\pm}(\omega)$ are obtained. Next, we insert the obtained solutions for $\delta A_1(\omega, z)$ and

$\delta A_1^*(-\omega, z)$ into Eqs. (5.11) and (5.12) to find $\delta A_2(\omega, z)$ and $\delta A_2^*(-\omega, z)$, which are related to the expressions for $e_{1\pm\pm}(\omega)$. The small parameters ϵ and ϵ_Ω have allowed us to use $Y_1 \ll \beta_1\omega$ and $\beta_2\omega^2 \ll \beta_1\omega$ to simplify expressions. Thus the dispersion relations and all the coupling coefficients for the c_1 and c_2 modes in Eq. (5.13) are obtained. The error introduced by this approximation is checked by putting the obtained $\delta A_2(\omega, z)$ and $\delta A_2^*(-\omega, z)$ (which, although very small, are nonzero) back into Eqs. (5.9) and (5.10) and verifying that the percentage error is $O(\epsilon, \epsilon_\Omega)$ and is quite small. A similar procedure is used for the c_3 and c_4 modes in Eq. (5.13) by starting with Eqs. (5.11) and (5.12).

It can be shown from Eqs. (5.16)-(5.25) that the r's can be $O(1)$ while the e's are at most $O(\epsilon)$. The significance of this observation can be seen by referring to Eq. (5.13). For the c_1 and c_2 modes, the coupling between the two forward sidebands is represented by $r_{1\pm}(\omega)$ while the coupling to the two backward sidebands is represented by the $e_{1\pm\pm}(\omega)$'s. Comparing with the case of a single forward pump wave, it is worth noticing that $r_{1\pm}(\omega)$ are not affected by the presence of the backward pump. Also, the dispersion relations $k_{1\pm}(\omega)$ for the c_1 and c_2 modes are the same as if the other pump wave did not exist. In the case of a single forward pump wave, it is well known that the coupling between the the two forward sidebands is caused by FWM between the sidebands and the forward pump.[12] Thus the presence of a counterpropagating pump wave introduces backward coupling into the eigenmodes through the coefficients $e_{1\pm\pm}$. The FWM picture of this coupling was described in.[12] Similar comments apply for the c_3 and c_4 modes with respect to the backward pump wave.

The above discussion indicates that the evolution of sidebands associated with the forward pump wave, $\delta A_1(\omega, z)$ and $\delta A_1^*(-\omega, z)$, is affected only by the relatively weak additive contributions from the distributed feedback (DFB) occurring because of the presence of a backward pump wave, and vice versa. However, note that when Y_1 (or Y_2) is very small, the c_1 and c_2 modes (or c_3 and c_4 modes) become degenerate. This means that Eq. (5.13) is not in a proper form to represent the general solution of Eqs. (5.9)-(5.12) in such a situation. Thus, it is not clear what would be the the magnitude of the backscattering contribution in general.

In order to find a proper general solution that can cover such cases, we transform the four constants c_1 and c_2, and c_3 and c_4, to c_{f+} and c^*_{f-}, and c_{b+} and c^*_{b-}, respectively, by

$$c_{f+} = c_1 + r_{1-}c_2, \qquad c_{b+} = c_3 + r_{2-}c_4, \tag{5.26}$$

$$c^*_{f-} = r_{1+}c_1 + c_2, \qquad c^*_{b-} = r_{2+}c_3 + c_4. \tag{5.27}$$

Basically, we demand that c_{f+} and c^*_{f-} represent the contributions to $\delta A_{1+}(\omega, 0)$ and $\delta A_{1-}(\omega, 0)$ from the c_1 and c_2 modes in Eq. (5.13), and c_{b+} and c^*_{b-} represent the contributions to $\delta A_{2+}(\omega, l)$ and $\delta A_{2-}(\omega, l)$ from c_3 and c_4 modes. The general solution (5.13) can be put in the following form in terms of the new constants c_{f+}, c^*_{f-}, c_{b+} and c^*_{b-}:

$$\vec{\delta A}_1(\omega, z) = e^{i\beta_1\omega z}\boldsymbol{M_f}(\omega, z)\vec{c}_f + e^{i\beta_1\omega(l-z)}\boldsymbol{M_{bf}}(\omega, l-z)\vec{c}_b, \tag{5.28}$$

$$\vec{\delta A}_2(\omega, z) = e^{i\beta_1\omega(l-z)}\boldsymbol{M_b}(\omega, l-z)\vec{c}_b + e^{i\beta_1\omega z}\boldsymbol{M_{fb}}(\omega, z)\vec{c}_f, \tag{5.29}$$

where

$$\begin{aligned}\boldsymbol{M_f}(\omega, z) \;=\; & \frac{1}{1 - r_+r_-} \\ & \begin{pmatrix} 1 & r_{1-} \\ r_{1+} & 1 \end{pmatrix}\begin{pmatrix} e^{iY_1z} & 0 \\ 0 & e^{-iY_1z} \end{pmatrix}\begin{pmatrix} 1 & -r_{1-} \\ -r_{1+} & 1 \end{pmatrix},\end{aligned} \tag{5.30}$$

$$\boldsymbol{M_{fb}}(\omega. z) = \frac{1}{1 - r_+ r_-} \begin{pmatrix} e_{1++} & e_{1-+} \\ e_{1+-} & e_{1--} \end{pmatrix} \begin{pmatrix} e^{iY_1 z} & 0 \\ 0 & e^{-iY_1 z} \end{pmatrix} \begin{pmatrix} 1 & -r_{1-} \\ -r_{1+} & 1 \end{pmatrix} \tag{5.31}$$

and we have adopted the notation, $\vec{\delta A}(\omega, z) = [\delta A(\omega, z), \delta A^*(-\omega. z)]$, and $\vec{c} = [c_+, c_-^*]$. The matrix elements are

$$M_{f11}(\omega. z) = (e^{iY_1 z} - r_{1+} r_{1-} e^{-iY_1 z})/(1 - r_{1+} r_{1-}), \tag{5.32}$$

$$M_{f12}(\omega. z) = r_{1-}(-e^{iY_1 z} + e^{-iY_1 z})/(1 - r_{1+} r_{1-}). \tag{5.33}$$

$$M_{f21}(\omega. z) = r_{1+}(e^{iY_1 z} - e^{-iY_1 z})/(1 - r_{1+} r_{1-}), \tag{5.34}$$

$$M_{f22}(\omega. z) = (-r_{1+} r_{1-} e^{iY_1 z} + e^{-iY_1 z})/(1 - r_{1+} r_{1-}) \tag{5.35}$$

and

$$M_{fb11}(\omega, z) = (e_{1++} e^{iY_1 z} - e_{1-+} r_{1+} e^{-iY_1 z})/(1 - r_{1+} r_{1-}), \tag{5.36}$$

$$M_{fb12}(\omega. z) = (-e_{1++} r_{1-} e^{iY_1 z} + e_{1-+} e^{-iY_1 z})/(1 - r_{1+} r_{1-}), \tag{5.37}$$

$$M_{fb21}(\omega. z) = (e_{1+-} e^{iY_1 z} - e_{1--} r_{1+} e^{-iY_1 z})/(1 - r_{1+} r_{1-}), \tag{5.38}$$

$$M_{fb22}(\omega. z) = (-e_{1+-} r_{1-} e^{iY_1 z} + e_{1--} e^{-iY_1 z})/(1 - r_{1+} r_{1-}). \tag{5.39}$$

The expressions for $\boldsymbol{M_b}$ and $\boldsymbol{M_{bf}}$ are similar to $\boldsymbol{M_f}$ and $\boldsymbol{M_{fb}}$, respectively, because of symmetry. Note that $\boldsymbol{M_f}(\omega, 0) = \mathbf{1}$ and $\boldsymbol{M_b}(\omega, l) = \mathbf{1}$.

The two parts of the general solutions (5.28) and (5.29) have a clear physical meaning. The forward and backward transfer matrices $\boldsymbol{M_f}$ and $\boldsymbol{M_b}$ give the transformation of the sidebands of the forward and the backward pump waves along their respective propagation distance as if the other pump wave did not exist, while the cross matrices $\boldsymbol{M_{bf}}$ and $\boldsymbol{M_{fb}}$ give the contribution to their evolution from the other pump wave due to backscattering (or DFB). Equations (5.28) and (5.29) are the main results of this section since they provide a simple model to describe evolution of the sidebands due to different physical mechanisms.

From Eqs. (5.30) and (5.31), it is easy to see that the relative magnitude of $\boldsymbol{M}_{fb}$ and $\boldsymbol{M}_f$ is normally $O(\epsilon)$ unless the denominator $1 - r_{1+}r_{1-}$ is very small. A careful analysis shows that this only occurs when $|Y_1|/(\gamma|A_{10}|^2) \ll 1$, which is equivalent to either $\Omega \ll 1$ for both normal and anomalous dispersion or $\Omega - 2 \ll 1$ for anomalous dispersion. Under these circumstances, the c_1 and c_2 modes are degenerate. However, because of our choice of the new set of constants, Eqs. (5.28) and (5.29) are still a valid form of the general solution since the matrix elements are finite. In fact, it can be shown that when $\Omega \ll 1$, Eqs. (5.32)-(5.39) reduce to

$$\begin{aligned} M_{f11} &= 1 + i\gamma|A_{10}|^2 z, && (5.40) \\ M_{f12} &= i\gamma A_{10}^2 z, && (5.41) \\ M_{f21} &= -i\gamma A_{10}^{*2} z, && (5.42) \\ M_{f22} &= 1 - i\gamma|A_{10}|^2 z && (5.43) \end{aligned}$$

and

$$\begin{aligned} M_{fb11} &= -\gamma A_{10}^* A_{20}/(\beta_1\omega), && (5.44) \\ M_{fb12} &= -\gamma A_{10} A_{20}/(\beta_1\omega), && (5.45) \\ M_{fb21} &= \gamma A_{10}^* A_{20}^*/(\beta_1\omega), && (5.46) \\ M_{fb22} &= \gamma A_{10} A_{20}^*/(\beta_1\omega). && (5.47) \end{aligned}$$

Similar expressions hold for $\boldsymbol{M}_b$ and $\boldsymbol{M}_{bf}$. It turns out that these solutions exactly satisfy Eqs. (5.9)-(5.12) for $\beta_2 = 0$, which is not surprising because the condition $\Omega \ll 1$ implies that GVD is not important. Thus, our general solution (5.28) and (5.29) includes the dispersionless case. This case has been studied in previous work[69] and is not the main concern here. Eqs. (5.40)-(5.47) show that even in the degenerate case, the magnitude of the cross matrix M_{fb} over that of the transfer matrix M_f is no more than $O(\epsilon/\Omega)$, and the same is true for M_{bf} and M_b. Thus, this conclusion about the relative magnitudes of M_{fb} and M_f, and M_{bf} and M_b, is quite general since it is also true when $\Omega \ll 1$ is not satisfied (including the case $\Omega - 2 \ll 1$ in the anomalous-dispersion regime).

The solution given by Eqs. (5.28) and (5.29) can also be written as

$$\begin{pmatrix} \delta\vec{A}_1(\omega, z) \\ \delta\vec{A}_2(\omega, z) \end{pmatrix} = e^{i\beta_1\omega z} \begin{pmatrix} \boldsymbol{M_f}(\omega, z) \\ \boldsymbol{M_{fb}}(\omega, z) \end{pmatrix} \vec{c}_f + e^{i\beta_1\omega(l-z)} \begin{pmatrix} \boldsymbol{M_{bf}}(\omega, l-z) \\ \boldsymbol{M_b}(\omega, l-z) \end{pmatrix} \vec{c}_b. \tag{5.48}$$

The form of Eq. (5.48) shows that the general solution is the superposition of two "modes" represented by $\vec{c}_f$ and $\vec{c}_b$. In the case $\epsilon/\Omega \ll 1$ or $\omega \gg \omega_W$, the $\vec{c}_f$ "mode" is primarily forward propagating with weak backscattering and the $\vec{c}_b$ "mode" is primarily backward propagating with weak forward scattering. In such a case, Eq. (5.48) is the analog of a similar equation found in DFB waveguides (see, for example[53]) in the limit of large detuning, except that, here the $\boldsymbol{M}$'s are matrices and the $\vec{c}$'s are vectors, whereas the corresponding entities "M" and "c" are scalar quantities for a DFB waveguide. It is well known that in a largely detuned DFB structure, the "c_f" term describes the forward propagation mode with "M_f" and "M_{fb}" indicating the relative amplitudes of the propagating and backreflecting components for a single frequency photon (and similarly for the "c_b" term). Thus

Eq. (5.48) is a generalized DFB formalism to the case of a pair of coupled photons at two different frequencies. A large detuning is known to decrease DFB. Similarly, the large walkoff effect for $\omega \ll \omega_W$ reduces the backscattering.

Note from Eqs. (5.32)-(5.39) that $M^*_{f11}(-\omega, z) = M_{f22}(\omega, z)$, $M^*_{f12}(-\omega, z) = M_{f21}(\omega, z)$, $M^*_{fb11}(-\omega, z) = M_{fb22}(\omega, z)$, and $M^*_{fb12}(-\omega, z) = M_{fb21}(\omega, z)$, as required by the symmetry between ω and $-\omega$. Furthermore, it can be shown that $\boldsymbol{M_f}(-\omega, z) = \boldsymbol{M_f}(\omega, z)$ and $\boldsymbol{M_{fb}}(-\omega, z) = -\boldsymbol{M_{fb}}(\omega, z)$. Similar properties hold for $\boldsymbol{M_b}$ and $\boldsymbol{M_{bf}}$.

Examining the asymptotic behavior of $\boldsymbol{M_f}(\omega, z)$ over a distance l, we notice that besides oscillations, the magnitude of its entries can also increase linearly or exponentially by the order of l/l_N and $\exp[l/l_N]$, respectively. The later case occurs only for the anomalous-dispersion regime when $\Omega \sim \sqrt{2}$, whereas the former happens whenever $|Y_1(\omega)|l \ll 1$, translating into the requirement of $\Omega \ll 1$ (i.e. nondispersive propagation) for both normal and anomalous regimes or $\Omega - 2 \ll 1$ for the anomalous regime. It is easy to see that the exponential growth is due to MI in the anomalous-dispersion regime. Similar properties hold for $\boldsymbol{M_b}$ in the backward direction. The amplifying nature of these transfer matrices are important because they lead to absolute instabilities when the system is subject to feedback. The asymptotic behavior of the cross matrices shows oscillations or exponential dependence on the distance.

5.3 Boundary reflections

Before discussing the instabilities of counterpropagating pump waves, we generalize the analysis of Sec. 5.2 to include the feedback occurring at the two facets of the finite Kerr medium (see Fig. 5-1). The boundary conditions at the front and rear surface of the Kerr medium can be written as

$$\delta\vec{A}_1(\omega,0) = \boldsymbol{R_f}\delta\vec{A}_2(\omega,0), \tag{5.49}$$

$$\delta\vec{A}_2(\omega,l) = \boldsymbol{R_b}\delta\vec{A}_1(\omega,l). \tag{5.50}$$

where

$$\boldsymbol{R_f} = \begin{bmatrix} r_f e^{i\psi_{rf}} & 0 \\ 0 & r_f e^{-i\psi_{rf}} \end{bmatrix}, \boldsymbol{R_b} = (f \to b). \tag{5.51}$$

Here, $\psi_{rf} = \phi_{rf} + \Delta_2$ and $\psi_{rb} = \phi_{rb} + \Delta_1$, where $\Delta_1 = k_0 l + \gamma(|A_{10}|^2 + 2|A_{20}|^2)l$ and $\Delta_2 = k_0 l + \gamma(|A_{20}|^2 + 2|A_{10}|^2)l$ are the linear and nonlinear phases associated with the propagation of the forward and backward pump waves, respectively. Further, $r_f \exp[i\phi_{rf}]$ and $r_b \exp[i\phi_{rb}]$ are the reflection coefficients for the front and rear boundaries, respectively ($0 < r_f < 1$ and $0 < r_b < 1$).

By using Eqs. (5.28) and (5.29), Eqs. (5.49) and (5.50) are transformed into

$$[\boldsymbol{1} - \boldsymbol{R_f M_{fb}}(\omega,0)]\vec{c}_f = e^{i\beta_1\omega l}[\boldsymbol{R_f M_b}(\omega,l) - \boldsymbol{M_{bf}}(\omega,l)]\vec{c}_b, \tag{5.52}$$

$$[\boldsymbol{1} - \boldsymbol{R_b M_{bf}}(\omega,0)]\vec{c}_b = e^{i\beta_1\omega l}[\boldsymbol{R_b M_f}(\omega,l) - \boldsymbol{M_{fb}}(\omega,l)]\vec{c}_f. \tag{5.53}$$

As a standard treatment, the solution of Eqs. (5.52) and (5.53) in the complex domain of ω represents an eigenvalue problem. In fact, such equations can be also found in the treatment of DFB lasers in the limit of large detuning, except that the vectors and matrices in the above are replace by scalar quantities. Thus, the problem can be considered as a doubly-resonant parametric oscillator[79] with the generalized DFB effect. The following algebraic equation for ω has to be satisfied for nontrivial solutions of $(\vec{c}_f, \vec{c}_b)$:

$$D(\omega) = |\mathbf{1} - e^{i2\beta_1\omega l}[\boldsymbol{R_f M_b}(\omega, l) - \boldsymbol{M_{bf}}(\omega, l)][\mathbf{1} - \boldsymbol{R_b M_{bf}}(\omega, 0)]^{-1}$$
$$[\boldsymbol{R_b M_f}(\omega, l) - \boldsymbol{M_{fb}}(\omega, l)][\mathbf{1} - \boldsymbol{R_f M_{fb}}(\omega, 0)]^{-1}| = 0. \qquad (5.54)$$

The multiple solutions ω_n (n is a dummy index) of Eq. (5.54) stand for different longitudinal supermodes. The real part of each solution gives the mode position and the imaginary part gives the growth or damping rate. Absolute instability occurs whenever there is a positive imaginary part to ω_n. By substituting the $\vec{c}_{fn}$ and $\vec{c}_{bn}$ obtained by solving Eq. (5.52) and (5.53) into Eq. (5.48), we can calculate the eigenfields corresponding to each supermode. It is evident that there are generally two counterpropagating pairs of sidebands for each longitudinal mode. Therefore, the eigen fields correspond to pulsing in the spatio-temporal domain.

Equation (5.54) can be simplified by dividing the parameter space into several regions. From the discussion in Sec. 5.2, we know that if $\Omega \ll 1$, this equation will reduce to the dispersionless case which has been studied before.[69] Therefore, we assume $\Omega \gg \epsilon$ so that the magnitude of $\boldsymbol{M_{fb}}(\omega, 0)$ and $\boldsymbol{M_{bf}}(\omega, 0)$ is much less than unity. Then the two inverse matrices in Eq. (5.54) can be approximated by unity, and we obtain,

$$D(\omega) = |\mathbf{1} - e^{i2\beta_1\omega l}[\boldsymbol{R_f M_b}(\omega, l) - \boldsymbol{M_{bf}}(\omega, l)]$$
$$[\boldsymbol{R_b M_f}(\omega, l) - \boldsymbol{M_{fb}}(\omega, l)]| = 0. \qquad (5.55)$$

For very small ϵ, there can be a region, $1 \gg \Omega \gg \epsilon$, overlapped by the cases considered in this paper and in reference.[69] In this region, the frequency is low enough that dispersion is not important, and yet high enough that cross coupling or DFB is weak.

Two cases are associated with Eq. (5.55). If the magnitudes of boundary reflection coefficients are much larger than $O(\epsilon/\Omega)$, the cross-matrix terms in Eq. (5.55) are much smaller than the transfer-matrix term multiplied by the reflection coefficients, and therefore can be neglected. Physically, this means that the localized feedback at the facets is much stronger than the weak DFB so that the latter effect can be ignored. Since ϵ is quite small, even relatively weak reflections from the uncoated air-glass boundary, which has an amplitude reflection coefficients of about 0.2, will fit into this category. The details of this case is discussed separately in Sec. 5.5.[52] In the following section, we discuss the case occurring when the boundary reflection coefficients are comparable to or less than $O(\epsilon/\Omega)$.

5.4 Weakly reflecting and anti-reflecting boundaries

In this case, Eq. (5.55) can be further simplified by using $|1 - \exp(i\beta_1\omega l)\boldsymbol{U}| = 1 - \exp(i2\beta_1\omega l)\mathrm{Tr}\boldsymbol{U} + \exp(i4\beta_1\omega l)|\boldsymbol{U}|$, where
$\boldsymbol{U} = [\boldsymbol{R_f M_b}(\omega, l) - \boldsymbol{M_{bf}}(\omega, l)][\boldsymbol{R_b M_f}(\omega, l) - \boldsymbol{M_{fb}}(\omega, l)]$. Thus, we have,

$$D(\omega) = 1 - e^{i2\beta_1\omega l}g(\omega) = 0, \tag{5.56}$$

where

$$\begin{aligned}
&g(\omega) = \mathrm{Tr}\boldsymbol{U} = \\
&(R_{f11}M_{b11} - M_{bf11})(R_{b11}M_{f11} - M_{fb11}) + \\
&(R_{f11}M_{b12} - M_{bf12})(R^*_{b11}M^*_{f12} + M^*_{fb12}) + \\
&(R^*_{f11}M^*_{b12} + M^*_{bf12})(R_{b11}M_{f12} - M_{fb12}) +
\end{aligned}$$

$$(R^*_{f11} M^*_{b11} + M^*_{bf11})(R^*_{b11} M^*_{f11} + M^*_{fb11}) \tag{5.57}$$

and where we have neglected $|U|$ since, by using Eqs. (5.30) and (5.31), we conclude that its amplitude is independent of l and is at the most $O(\epsilon/\Omega)^4$ (for $|r_f|, |r_b| \sim \epsilon$), which is much smaller than unity. Actually, one can prove that $|U|$ can be neglected as long as $|r_f|, |r_b| \ll 1$. Eq. (5.56) is in a standard form for the laser threshold condition with $g(\omega)$ representing the net gain. Thus $|g(\omega)| > 1$ is required for absolute instability.

From Eq. (5.57), it is evident that for the weak boundary reflection ($|r_f|, |r_b| \sim \epsilon$) under consideration, $|g|$ is at the most $O(\epsilon/\Omega)^2$ when the order of the normalized length $L = l/l_N$ is equal or much less than unity, and the system is below instability threshold. As L increases, $|g|$ can either increase as L^2 for both the normal and anomalous dispersion regime or as $\exp(2L)$ for the anomalous dispersion regime when $\Omega \sim \sqrt{2}$. For the case of quadratic amplification that occurs when GVD is negligible, previous results[69] indicate that the threshold condition requires L to be $O[1/\sqrt{|r_f r_b|}]$. This represents a very high threshold in the case of weak boundary reflections. On the other hand, the exponential amplification in the anomalous region requires L to be $O[\ln(\Omega/\epsilon)]$ to reach threshold, which is much easier to satisfy. Thus we concentrate on the anomalous dispersion case where Ω is $O(1)$. By using Eqs. (5.32)-(5.39), Eq. (5.57) becomes

$$\begin{aligned} g(\omega) \quad &= [e^{-iY_2 l}(r_1 e_2 + e_2 + r_1 r_2 r_f e^{i\theta_f} - r_f e^{-i\theta_f})(r_2 e_1 + e_1 + r_2 r_1 r_b e^{i\theta_b} - r_b e^{-i\theta_b}) \\ &-e^{iY_2 l}(r_1 e_2 + e_2 + r_1 r_f e^{i\theta_f} - r_2 r_f e^{-i\theta_f})(r_2 e_1 + e_1 + r_1 r_b e^{i\theta_b} - r_2 r_b e^{-i\theta_b})] \\ &e^{-iY_1 l}/[(1 - r_1^2)(1 - r_2^2)], \end{aligned} \tag{5.58}$$

with

$$r_1(\omega) = (Y_1 - \beta_2\omega^2/2)/(\gamma|A_{10}|^2) - 1, \tag{5.59}$$

$$r_2(\omega) = (Y_2 - \beta_2\omega^2/2)/(\gamma|A_{20}|^2) - 1, \tag{5.60}$$

$$e_1(\omega) = (r_1 + 1)\gamma|A_{10}A_{20}|/(\beta_1\omega), \tag{5.61}$$

$$e_2(\omega) = (r_2 + 1)\gamma|A_{10}A_{20}|/(\beta_1\omega), \tag{5.62}$$

$$\theta_f = \phi_{rf} + k_0 l + \gamma(|A_{20}|^2 + 2|A_{10}|^2)l + \phi_{20} - \phi_{10}, \tag{5.63}$$

$$\theta_b = \phi_{rb} + k_0 l + \gamma(|A_{10}|^2 + 2|A_{20}|^2)l + \phi_{10} - \phi_{20}, \tag{5.64}$$

where, realizing that $-iY_1(\omega) = |Y_1(\omega)|$, which is the gain curve of MI of the forward pump wave, we have ignored $\exp(-|Y_1|l)$ compared with $\exp(|Y_1|l)$ since $\exp(|Y_1|l) \sim \Omega/\epsilon$ in order to reach threshold. However, $\pm iY_2(\omega)$ can be imaginary within the MI frequency range of the forward pump since we have assumed the power ratio of the backward and forward pump waves satisfies $S \leq 1$.

Equation (5.58) can be further simplified when the boundary reflections can be ignored for $|r_f|, |r_b| \ll \epsilon$. This is the condition when the boundary can be considered as anti-reflecting. The instability gain is then given by

$$g(\omega) = -i\frac{\gamma^2|A_{10}|^2|A_{20}|^2\beta_2^2\omega^2}{2\beta_1^2 Y_1 Y_2}e^{-iY_1 l}\sin(Y_2 l), \tag{5.65}$$

or written in terms of normalized frequency Ω and normalized length L,

$$g(\omega) = \epsilon^2\overline{g}(\Omega, L), \tag{5.66}$$

where

$$\overline{g}(\Omega, L) = -\frac{S\Omega^2 e^{L\sqrt{1-(\Omega^2/2-1)^2}}\sin[L\sqrt{(\Omega^2/2 - S)^2 - S^2}]}{2\sqrt{1-(\Omega^2/2-1)^2}\sqrt{(\Omega^2/2 - S)^2 - S^2}}. \tag{5.67}$$

Equation (5.56) can then be written as

$$1 - \epsilon^2 \exp(i2\Omega L/\epsilon)\overline{g}(\Omega, L) = 0. \tag{5.68}$$

Equation (5.68), which is still in the standard form used to describe the threshold of laser oscillation, can be easily analyzed since ϵ is a small parameter. Different values of Ω for which Eq. (5.68) is satisfied correspond to various longitudinal supermodes mentioned earlier. First, we note that the mode spacing is only $\sim \epsilon/L$ while the gain $\overline{g}(\Omega, L)$ varies on the frequency scale of $1/L$. Thus, the various mode can be considered continuously distributed under the gain curve. For any mode frequency Ω_r, the growth (damping) rate is a small quantity and is given by

$$\Omega_i = \epsilon \ln[\epsilon^2 |\overline{g}(\Omega_r, L)|]/(2L), \tag{5.69}$$

or written in physical units,

$$\omega_i = \ln|g(\omega_r)|/(2l\beta_1). \tag{5.70}$$

Compared to the previous numerical work,[19,70] Eqs. (5.65)-(5.70) not only give analytic results for arbitrary power ratios, but also provides a simple physical characterization of the instability in terms of the familiar language of laser oscillation. By using Eq. (5.69), Fig. 5-2(a) and 5-2(b) show the growth (damping) rate versus frequency for different forward pump powers (or normalized length) for the power ratios $S = 1$ and $S = 0.5$, respectively. The oscillatory behavior in Fig. 5-2(b) occurs when Y_2 is real in the frequency region where the less intense backward pump wave is modulationally stable. In such a region the nonlinear phase shift $Y_2(\omega)l$, which depends on frequency, can cause constructive or destructive interference.

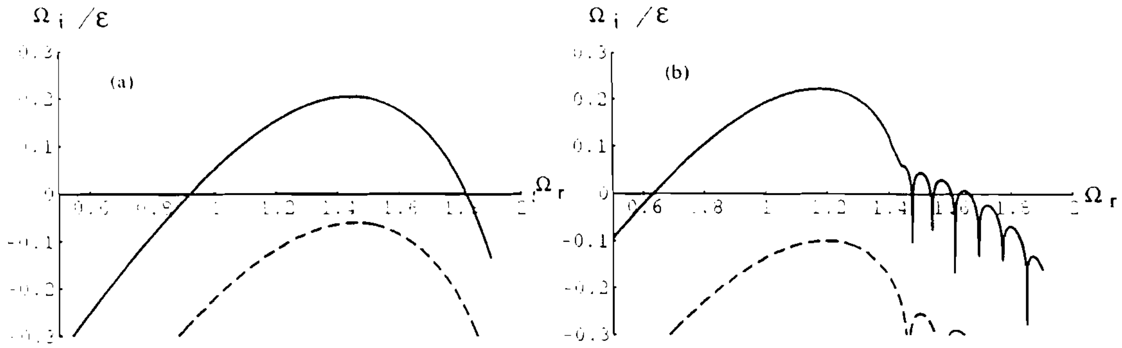

Figure 5-2: Growth (damping) rate written as Ω_i/ϵ versus frequency Ω_r, for $\epsilon = 10^{-4}$. (a) $S = 1$ (equal pump powers), and the forward pump powers correspond to $L = 9$ (dashed) and $L = 12$ (solid). (b) $S = 0.5$ (unequal pump powers), and the forward pump powers correspond to $L = 12$ (dashed) and $L = 20$ (solid).

The instability threshold condition for any frequency is obtained by setting the right side of Eq. (5.69) or (5.70) to zero. Thus, the threshold curve is just the contour $|c^2\overline{g}(\Omega_r, L)| = 1$. Figure 5-3(a) and 5-3(b) shows the threshold curves for different power ratios obtained from Eq. (5.67). The area above the curve indicates the instability region for the corresponding power ratio. As in Fig. 5-2(b), the oscillation in Fig. 5-3(b) is caused due to a similar reason.

For an order of magnitude estimate, let us assume equal pump powers (this is the case that has been numerically investigated previously[49,70]). Then, the threshold contour can be written as

$$L = \frac{\ln[4[1 - (\Omega^2/2 - 1)^2]/(\Omega^2\epsilon^2)]}{2\sqrt{1 - (\Omega^2/2 - 1)^2}}, \tag{5.71}$$

where we used $\sin[L\sqrt{(\Omega^2/2 - S) - S^2}] \approx i\exp[L\sqrt{S^2 - (\Omega^2/2 - S)^2}]/2$ in Eq. (5.67) and assumed $S = 1$. From Eq. (5.71), the minimum L, or the threshold of the system, is achieved at $\Omega = \sqrt{2}$ (which is the frequency for the maximum

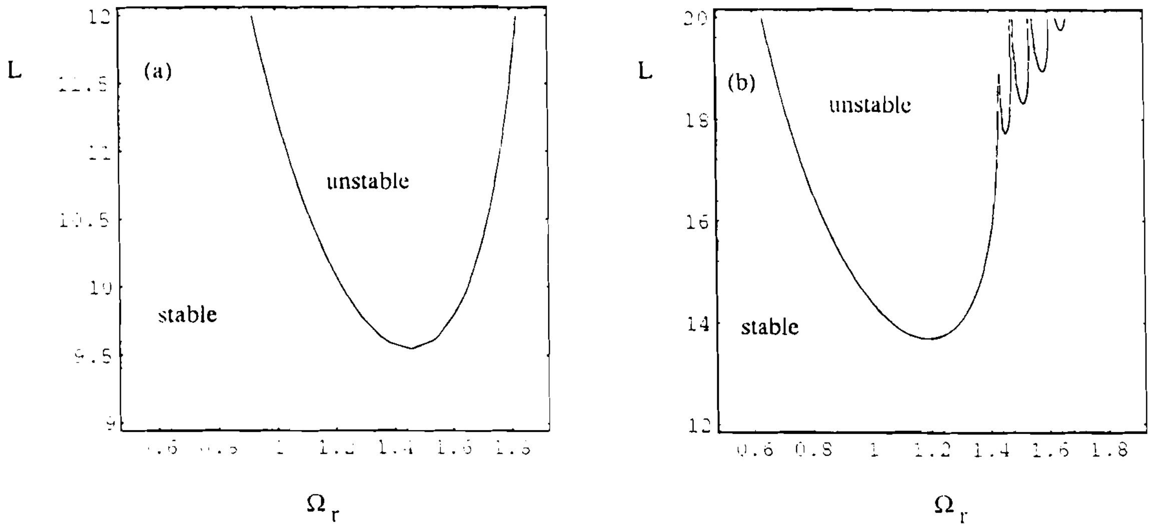

Figure 5-3: Threshold curves in Ω_r-L plane, for $\epsilon = 10^{-4}$. The area above the curve corresponds to instability. (a) $S = 1$ and (b) $S = 0.5$.

MI gain for a given pump power), so that in general, L is approximately $-\ln(\epsilon)$. This is in agreement with the previous work.[49,70,71] For the numerical parameter $\epsilon \sim 10^{-4}$ in our example, $L \sim 9$ or $l \sim 1$ m. In the normalized frequency, the mode spacing is $\sim \epsilon\Omega_D/L$, which is 0.2 ns^{-1} (30 MHz) in our example. The growth (damping) rate is of the same order as the mode spacing according to Eq. (5.69).

Although the above conclusions [including Eq. (5.70)] were drawn for the special case of negligible boundary reflections (or anti-reflection boundary condition), they are valid in general since a similar analysis can be applied. The only difference is that we have to use Eq. (5.58) instead of Eq. (5.65) to include the effects of weak boundary reflections. Figure 5-4(a) shows the effect of boundary reflections on the growth (damping) rate under conditions identical to those of Fig. 5-2(a) except that both facets of the dispersive Kerr medium are assumed to have an amplitude reflection coefficient of 5×10^{-4}. Figure 5-4(b) shows changes in the threshold curve and should be compared with Fig. 5-3(a).

In general, even weak boundary reflections can substantially affect both the instability region and the growth rate as long as the amplitude reflection coefficients are comparable to ϵ (which is $\sim 10^{-4}$ in the example used here). This is because the DFB and the facet feedback can be in phase or out of phase with respect to each other, depending on the modulational frequency.

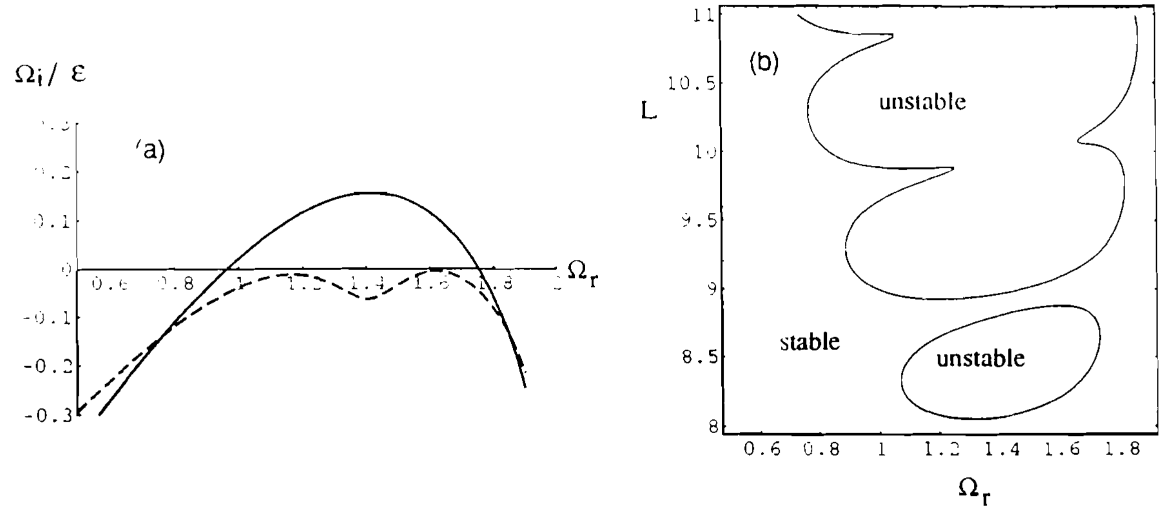

Figure 5-4: Effects of weak boundary reflections, for $\epsilon = 10^{-4}$, $r_f = r_b = 5 \times 10^{-4}$ and $S = 1$. (a) Ω_i/ϵ versus frequency Ω_r for $L = 9$, $\theta_f = \theta_b = \pi/2$ (dashed) and $\theta_f = \theta_b = 0$ (solid). (b) Threshold curves in Ω_r-L plane, for $\phi_{rf} = \phi_{rb} = k_0 l = 0$ and $\phi_{20} = \phi_{10}$.

Unlike the Ikeda instability, which vanishes when the boundary feedback is removed, the above instability exists for weak or even anti-reflection boundaries. While the Ikeda instability draws on the linear or quadratic spatial growth of dispersionless FWM, the instability discussed in this section draws on the exponential spatial growth of MI. (The normal dispersion case with relatively strong boundary reflections will be discussed in Part II.)

The treatment in this section is valid as long as the boundary reflection coefficients are much smaller than one. Furthermore, for relatively strong boundary reflections whose amplitude reflection coefficients are much larger than ϵ, the treatment in Sec. 5.5 can also be applied. In the case of an optical fiber, the illustrative example shows that the strong boundary reflection condition is likely to be satisfied in practice unless high quality anti-reflection coatings (or index matching materials) and very large pump powers are used. In other words, when applied to optical fibers the results of this section show that the previous work[49, 70] for fibers with anti-reflection coatings on both ends is not realistic. We consider the more realistic case in Sec. 5.5. However, the results in this section are quite general for nonlinear dispersive media and can be important when applied to materials with relatively large ϵ (but still much smaller than unity).

5.5 Strongly reflecting boundaries

As discussed in Sec. 5.3, by strong reflection we refer to cases in which $\Omega \gg \epsilon$ (or $\omega \gg \omega_W$) and the amplitude reflection coefficients of the FP cavity are much larger than $O(\epsilon/\Omega)$. When the first condition is satisfied, the forward and backward propagating pairs of sidebands evolve independently as if the counterpropagating pump wave were absent. The role of the counterpropagating pump wave is to induce a weak scattering of the propagating sidebands through XPM in the opposite direction. This scattering can be considered as a weak DFB with a magnitude $O(\epsilon/\Omega)$. Thus it can be neglected when the second condition is satisfied. As a result, the cross matrices $\boldsymbol{M_{fb}}$ and $\boldsymbol{M_{bf}}$ can be ignored in Eq. (5.55) as well as in Eq. (5.48). In such a case, Eq. (5.55) becomes

$$D(\omega) = |1 - e^{i2\beta_1 \omega l} \boldsymbol{R_f M_b R_b M_f}| = 0, \tag{5.72}$$

where $\boldsymbol{M_f}(\omega, l)$ and $\boldsymbol{M_b}(\omega, l)$ were shortened to $\boldsymbol{M_f}$ and $\boldsymbol{M_b}$. Note that this equation is the analog of the FP laser equation, in which the matrices are replaced by scalars. This makes sense since, after we neglect the weak DFB, we have a photon-pair FP laser.

The calculation of $D(\omega)$ from Eq. (5.72) is straightforward. The result is

$$D(\omega) = 1 - r_f r_b e^{i2\beta_1 \omega l} G(\omega) + (r_f r_b e^{i2\beta_1 \omega l})^2 = 0, \tag{5.73}$$

where

$$G(\omega) = M_{f11} M_{b11} e^{i(\psi_{rf} - \psi_{rb})} + M_{f21} M_{b12} e^{i(\psi_{rf} - \psi_{rb})} + c.c. \tag{5.74}$$

Equation (5.73) can be put in the familiar form of the threshold condition for a laser:

$$r_f r_b G_{eff\pm}(\omega) e^{i2\beta_1 \omega l} = 1, \tag{5.75}$$

where the effective gain is

$$G_{eff\pm}(\omega) = (G \pm \sqrt{G^2 - 4})/2. \tag{5.76}$$

Since $G_{eff+} G_{eff-} = 1$, either $G_{eff+} \geq 1$ or $G_{eff-} \geq 1$. For an unstable supermode, the gain should overcome the loss, i.e.

$$|G_{eff\pm}(\omega)| > 1/(r_f r_b). \tag{5.77}$$

For $r_f r_b \ll 1$, $|G_{eff\pm}| \gg 1$ is needed for instability, which, in turn requires $|G| \gg 1$. In this case, Eq. (5.76) simplifies to yield $G_{eff+} \approx G$, while G_{eff-} can be neglected. In the following, we use the convention that the + sign denotes the branch with higher gain. Under such a convention, $\ln|G_{eff+}| = -\ln|G_{eff-}| \geq 0$ and the net gain $g(\omega)$ used in the previous section is simply $r_f r_b G_{eff+}(\omega)$.

In order to gain some physical insight, let us start with the special case of $|A_{10}| = |A_{20}|$ so that $Y_1 = Y_2$, $r_1 = r_2$. By expressing the transfer matrices in terms of Y_1, Y_2 and r_1 r_2 as in previous section, Eq. (5.74) becomes

$$\begin{aligned} G = & [e^{i(2Y_1 l+\psi_{rf}+\psi_{rb})}(1 - r_1^2 e^{-i2(\psi_{rf}+\psi_{rb})}) \\ & + e^{-i(2Y_1 l+\psi_{rf}-\psi_{rb})}(1 - r_1^2 e^{i2(\psi_{rf}-\psi_{rb})})]/(1 - r_1^2) \\ & + 2[\cos(\theta_f - \theta_b) - \cos(\psi_{rf} + \psi_{rb})](\gamma|A_{10}|^2 l)^2 \mathrm{sinc}^2(Y_1 l), \end{aligned} \tag{5.78}$$

where $\theta_f = \psi_{rf} + \phi_{20} - \phi_{10}$, $\theta_b = \psi_{rb} + \phi_{10} - \phi_{20}$ and $\mathrm{sinc}(x) = \sin x/x$. When $\psi_{rf} + \psi_{rb}$ and $\theta_f - \theta_b$ are multiples of 2π, G in Eq. (5.78) is considerably simplified and Eq. (5.76) becomes

$$G_{eff\pm} = e^{\mp i2Y_1 l}. \tag{5.79}$$

This equation has a very simple physical meaning since $-iY_1$ is just the gain from MI in the case of anomalous dispersion, where Y_1 is imaginary with a maximum magnitude of $\gamma|A_{10}|$.[12]

If $\beta_2 \geq 0$, Y_1 is real. Thus, Eq. (5.75) [when combined with Eq. (5.79] does not have solutions with $\mathrm{Im}\omega \geq 0$, and the system is stable. However, for $\beta_2 < 0$, Eq. (5.79) and (5.75) simply mean the MI gain can overcome the reflection loss, and the system can be unstable. This instability does not correspond to the conventional Ikeda instability since it does not exist for a dispersionless medium. Using the normalized frequency Ω and length L, Fig. 5-5(a) shows the gain curves $\ln|G_{eff+}|$ for $\beta_2 < 0$.

The frequencies and growth (damping) rates for different modes are determined

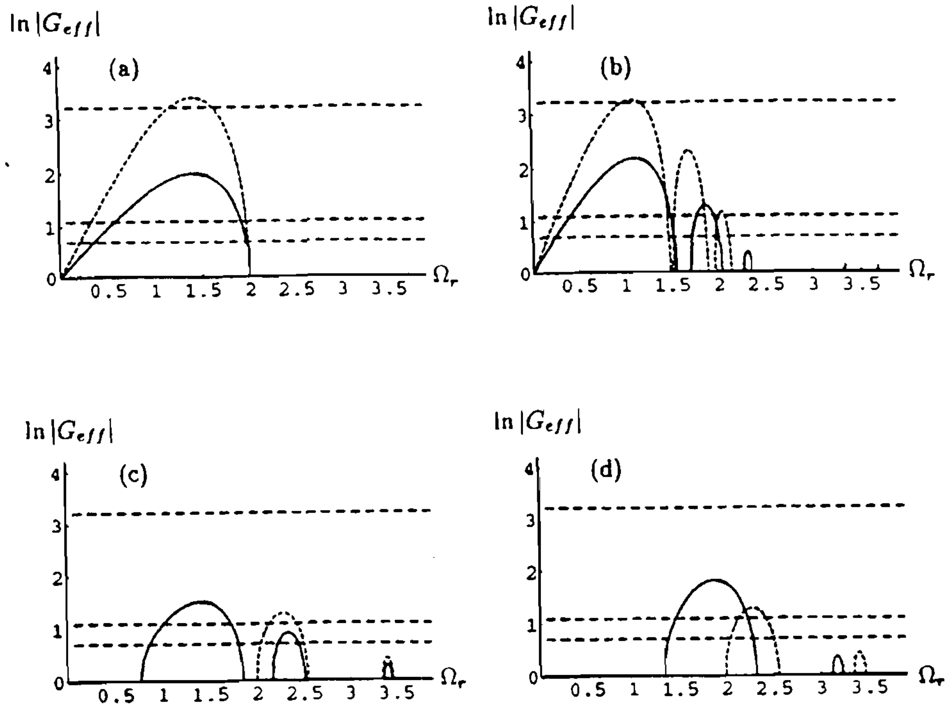

Figure 5-5: Gain curves $\ln|G_{eff}(\Omega_r)|$ for the case of anomalous dispersion. (a) The pump power $|A_{20}|^2 = |A_{10}|^2$, and the phases $\psi_{rf} + \psi_{rb}$, $\phi_{20} - \phi_{10}$ and $\psi_{rf} - \psi_{rb}$ are multiples of 2π. The solid curve is for $L = l/l_N = l\gamma|A_{10}|^2 = 1$ and the dashed curve is for $L = 1.7$. (b) Same as (a), except that $|A_{20}|^2 = |A_{10}|^2/3$, and the solid and dashed curves are for $L = 1.7$ and 2.6, respectively. (c) Same as (a), except that $L = 1$, and the solid and dashed curves are for $\phi_{20} - \phi_{10} = \pi/4$ and $\pi/2$, respectively. (d) Same as (a), except that $L = 1$, and the solid and dashed curves are for $\psi_{rf} + \psi_{rb} = \pi/2$ and π, respectively. In all cases, the three horizontal loss lines represent the loss $-\ln(r_f r_b)$ for $r_f r_b = 4\%$ (upper), 30% and 50% (lower), respectively. The difference between the gain curve and the loss line indicates the growth or damping rate in units of $1/(2l\beta_1) = \omega_W/(2L)$, depending on whether the gain is larger or smaller than the loss.

by substituting Eq. (5.79) in Eq. (5.75) and solving for Ω, i.e.,

$$\exp\{iL[2\Omega/\epsilon \mp \sqrt{(\mathrm{sign}(\beta_2)\Omega^2/2+1)^2-1}]\} = 1/(r_f r_b), \tag{5.80}$$

where $\epsilon = \sqrt{|\beta_2|\gamma|A_{10}|^2/\beta_1^2}$ is the small quantity introduced before. This equation can be solved by treating ϵ as a small parameter. For the typical case in which $1-r_f r_b$ is not a small quantity we come to the conclusion that $\mathrm{Re}[\Omega(n)] \equiv \Omega_r(n)$ is almost continuous under the gain curve (where n is the mode index). The growth (damping) rate Ω_i is a small quantity and is given by

$$\mathrm{Im}\Omega \equiv \Omega_i = \epsilon[\ln|e^{\mp iL\sqrt{\mathrm{sign}(\beta_2)(\Omega_r^2/2+1)^2-1}}| + \ln(r_f r_b)]/(2L)$$

as a function of Ω_r, or written in terms of physical units,

$$\omega_i = [\ln|G_{eff+}(\omega_r)| + \ln(r_f r_b)]/(2l\beta_1). \tag{5.81}$$

Apparently, the mode spacing is $O(\epsilon) \ll 1$ while the scale of variation of the gain curves is $O(1)$ in the normalized frequency.

Although the above conclusions were drawn for the special case of equal pump powers with $\psi_{rf} + \psi_{rb}$ and $\theta_f - \theta_b$ being multiples of 2π, they are valid in general since a similar analysis can be applied. Thus, the gain curves $\ln|G_{eff+}(\omega_r)|$ give almost all the needed information. According to Eq. (5.81), the gain curve has to be higher than the loss line $-\ln(r_f r_b) > 0$ for an unstable system, and their difference determines the growth or damping rate of each supermode. The threshold condition around frequency ω_r is $\ln|G_{eff+}(\omega_r)| \geq -\ln(r_f r_b)$. The other branch of the gain curve $\ln|G_{eff-}|$ is always below threshold (it is actually below zero). The growth rate or damping rate is on a scale of $1/(2l\beta_1)$, which is about 10 $\mu\mathrm{s}^{-1}$ if we use $l = 1/(\gamma P)$ as a typical value, and use the previous values for γ, P and

β_1. For these parameters, the gain curves vary on a scale of 2 ps^{-1} and the mode spacing is on a scale of 10 μs^{-1}. Generally, the mode spacing is on a scale of ω_W while the growth (or damping) rate varies on a scale of ω_D.

Figure 5-5(b)-(d) show the gain curves from Eqs. (5.76) and (5.74) for unequal pump intensities and different values of the phases. Multiple gain regions exist because of the constructive or destructive interference induced by the nonlinear phase shifts.

Figure 5-6 shows the case of normally dispersive ($\beta_2 > 0$) Kerr media. Thus the instabilities can exist even for normal dispersion. From the discussion of Sec. 5.2, it should be noted that these gain curves do not apply around the zero modulational frequency within a bandwidth covering several ω_W. In this region, the results from the dispersionless treatment[69] indicate that the growth or damping rate in the presence of the Ikeda instability can vary on the scale of the mode spacing. However, the high-frequency limit of the dispersionless treatment can still be described by the present method, corresponding to the low frequency end of our gain curve. In fact, the low-frequency limits of the gain curves in Fig. 5-6(b) correspond to the Ikeda instability. The same is true for the highest gain curves in Fig. 5-6(a) and 5-6(c). There is no correspondence to the conventional Ikeda instability for the rest of gain curves shown in Figs. 5-5 and 5-6, where instability is due to dispersion.

Since $G_{eff+} \approx G$ can be used for large gain, Eq. (5.78) indicates that a large pump powers or a long medium (or both) are needed. In such a limit, the MI gain contributes most to the gain curve in the case of the anomalous-dispersion regime, due its exponential dependence on both parameters. In fact, it can be

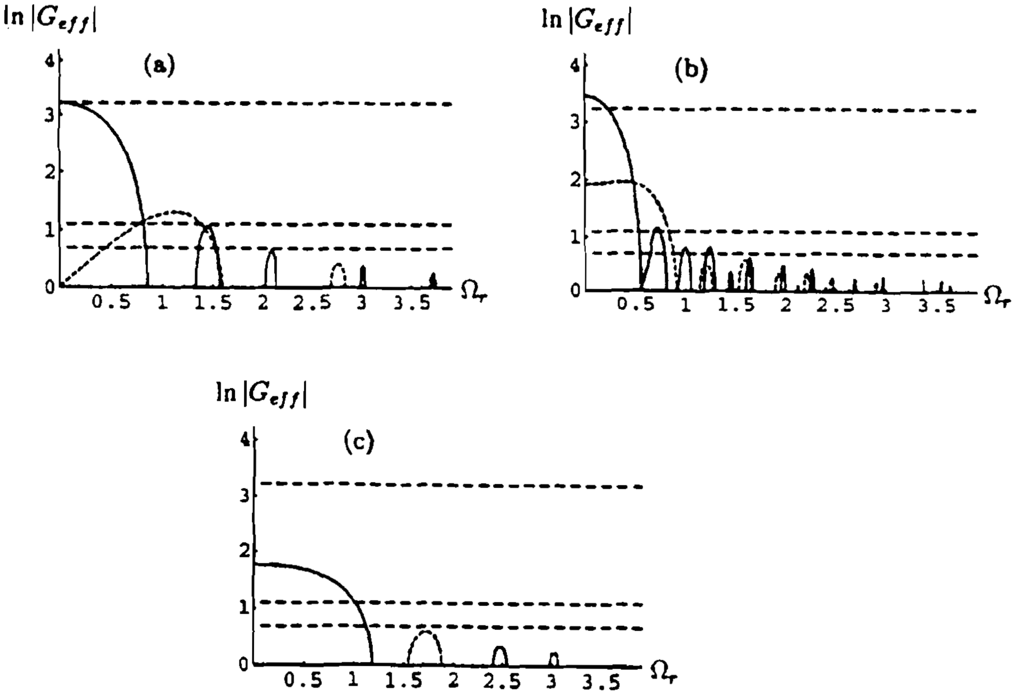

Figure 5-6: Gain curves $\ln|G_{eff}(\Omega_r)|$ for the case of normal dispersion. (a) The pump powers $|A_{20}|^2 = |A_{10}|^2$, and the phases $\psi_{rf} + \psi_{rb}$ and $\psi_{rf} - \psi_{rb}$ are multiples of 2π, $\phi_{20} - \phi_{10} = \pi/2$. The dashed and solid curves are for $L = 1$ and 2.6 respectively. (b) Same as (a), except that $|A_{20}|^2 = |A_{10}|^2/3$, and the dashed and solid curves are for $L = 2.6$ and 5 respectively. (c) Same as (a), except that $L = 1$, $\psi_{rf} + \psi_{rb} = \pi/2$, and the dashed and solid curves are for $\phi_{20} - \phi_{10} = 0$ and $\pi/2$ respectively. In all cases, the three horizontal loss lines are the same as in Fig. 5-5.

shown that near the peak of the gain curve

$$\begin{aligned} G_{eff+} \approx G &= [e^{-iY_2 l}(r_1 r_2 e^{i\theta_f} - e^{-i\theta_f})(r_1 r_2 e^{i\theta_b} - e^{-i\theta_b}) \\ &\quad - e^{iY_2 l}(r_1 e^{i\theta_f} - r_2 e^{-i\theta_f})(r_1 e^{i\theta_b} - r_2 e^{-i\theta_b})] \\ &\quad e^{-iY_1 l}/[(1 - r_1^2)(1 - r_2^2)], \end{aligned} \tag{5.82}$$

where we have neglected $\exp(iY_1 l) = \exp(-|Y_1| l)$ compared with $\exp(-iY_1 l)$. We have kept $\exp(\mp iY_2 l)$ since, with the assumption of $|A_{20}|^2 \leq |A_{10}|^2$, Y_2 can either be imaginary or real within the frequency range $0 < \Omega_r < 2$ where Y_1 is imaginary. For the large gain limit in the normal-dispersion case, however, the low-frequency gain increases at most quadratically (due to the double pass) with both of the parameters, while the higher-frequency gain is bounded.

5.6 Probe transmissivity and reflectivity

The simplification made by neglecting the cross matrices in the presence of strong reflection allows us to include the general case of probe injection in our analytical study.

If the probe fields $\delta A_i(\omega)$ are injected at the left mirror located at $z = 0$, the boundary condition can be written as

$$\delta\vec{A}_1(\omega, 0) = \boldsymbol{T}'_f \delta\vec{A}_i(\omega) + \boldsymbol{R}_f \delta\vec{A}_2(\omega, 0) \tag{5.83}$$

(5.84)

in place of Eq. (5.49), where

$$\boldsymbol{T'_f} = \begin{bmatrix} t'_f \exp(i\phi_{t'f}) & 0 \\ 0 & t'_f \exp(-i\phi_{t'f}) \end{bmatrix}.$$

Here, $t'_f \exp[i\phi_{t'f}]$ is the transmission coefficient into the medium at the left mirror. We also have, by applying Eq. (5.48) with the cross matrices set equal to zero,

$$\delta\vec{A}_1(\omega, l) = e^{i\beta_1\omega l}\boldsymbol{M_f}(\omega, l)\delta\vec{A}_1(\omega, 0), \tag{5.85}$$

$$\delta\vec{A}_2(\omega, 0) = e^{i\beta_1\omega l}\boldsymbol{M_b}(\omega, l)\delta\vec{A}_2(\omega, l). \tag{5.86}$$

Below the absolute instability threshold, the field transmitted from the system is $\delta\vec{A}_t(\omega) = \boldsymbol{T_b}\delta\vec{A}_1(\omega, l)$, whereas the backreflected field is $\delta\vec{A}_r(\omega) = \boldsymbol{T_f}\delta\vec{A}_2(\omega, 0)$, where

$$\boldsymbol{T_f} = \begin{bmatrix} t_f \exp(i\phi_{tf}) & 0 \\ 0 & t_f \exp(-i\phi_{tf}) \end{bmatrix}, \boldsymbol{T_b} = (f \leftrightarrow b),$$

and $t_f \exp(i\phi_{tf})$ and $t_b \exp(i\phi_{tb})$ are the transmission coefficients out of the medium at the front boundary and rear boundary, respectively. By using Eqs. (5.85), (5.86), (5.83) and (5.50), we find that the transmitted and reflected fields are related to the input field by

$$\begin{aligned} \delta\vec{A}_t(\omega) &\equiv \boldsymbol{T}\delta\vec{A}_i(\omega) \\ &= e^{i\beta_1\omega l}\boldsymbol{T_b}\boldsymbol{M_f}(1 - e^{i2\beta_1\omega l}\boldsymbol{R_f}\boldsymbol{M_b}\boldsymbol{R_b}\boldsymbol{M_f})^{-1}\boldsymbol{T'_f}\delta\vec{A}_i(\omega), \qquad (5.87) \\ \delta\vec{A}_r(\omega) &\equiv \boldsymbol{R}\delta\vec{A}_i(\omega) \\ &= e^{i2\beta_1\omega l}\boldsymbol{T_f}\boldsymbol{M_b}\boldsymbol{R_b}\boldsymbol{M_f}(1 - e^{i2\beta_1\omega l}\boldsymbol{R_f}\boldsymbol{M_b}\boldsymbol{R_b}\boldsymbol{F}\boldsymbol{M_f})^{-1}\boldsymbol{T'_f}\delta\vec{A}_i(\omega), \quad (5.88) \end{aligned}$$

where $\boldsymbol{T}$ and $\boldsymbol{R}$ are defined as the transmission and reflection matrices for the nonlinear FP system. They are symmetric between $-\omega$ and ω so that $T_{21} = T_{12}^*$, $T_{22} = T_{11}^*$, $R_{21} = R_{12}^*$, and $R_{22} = R_{11}^*$. Physically T_{11} and T_{12} indicate the transmission coefficients at the input frequency and at the FWM frequency, respectively. Note that Eqs. (5.87) and (5.88) are the coupled-photon version of similar equations for the transmission and reflection of a linear FP cavity.

In pump-probe experiments, an external probe is injected into the cavity together with the counterpropagating pump beams and information about the cavity is gathered by measuring probe transmissivity and reflectivity below the absolute instability threshold of the system. The transmission and reflection matrices can be calculated in a straightforward manner from Eqs (5.87) and (5.88). The results are

$$
\begin{aligned}
T_{11}(\omega) &= e^{i(\beta_1\omega l+\phi_{tb}+\phi_{t'f})} t_b t'_f (M_{f11} - r_f r_b e^{i(2\beta_1\omega l-\psi_{rf}-\psi_{rb})} M_{b22})/D(\omega) \qquad (5.89)\\
T_{12}(\omega) &= e^{i(\beta_1\omega l+\phi_{tb}-\phi_{t'f})} t_b t'_f (M_{f12} + r_f r_b e^{i(2\beta_1\omega l+\psi_{rf}-\psi_{rb})} M_{b12})/D(\omega) \qquad (5.90)\\
R_{11}(\omega) &= e^{i(2\beta_1\omega l+\phi_{tf}+\phi_{t'f})} t_f t'_f r_b (e^{-i\psi_{rb}} M_{f21} M_{b12} + e^{i\psi_{rb}} M_{f11} M_{b11}\\
&\quad - e^{i(2\beta_1\omega l-\psi_{rf})} r_f r_b)/D(\omega), \qquad (5.91)\\
R_{12}(\omega) &= e^{i(2\beta_1\omega l+\phi_{tf}-\phi_{t'f})} t_f t'_f r_b (e^{-i\psi_{rb}} M_{f22} M_{b12} + e^{i\psi_{rb}} M_{f12} M_{b11})\\
&\quad /D(\omega), \qquad (5.92)
\end{aligned}
$$

where $T_{21} = T_{12}^*$, $T_{22} = T_{11}^*$, $R_{21} = R_{12}^*$, and $R_{22} = R_{11}^*$, satisfying the aforementioned symmetry between $-\omega$ and ω.

There are two frequency scales over which the transmission and reflection coefficients vary. In the normalized variables Ω and L, the fast scale of Ω is in the term $\exp(i2\beta_1\omega l) = \exp(i2\Omega L/\epsilon)$, resulting in $O(\epsilon)$-scale oscillations corresponding to mode spacing. The frequency dependence of the other terms in Eqs. (5.89)-(5.92) and (5.73) is on the $O(1)$ scale. The behavior on each scale can be studied independently.

Considerable simplification can be made for the case in which $r_f r_b \ll 1$. In this limit, Eqs. (5.89)-(5.92) become

$$T_{11}(\omega) = e^{i(\beta_1 \omega l + \phi_{tb} + \phi_{t'f})} t_b t'_f M_{f11} / (1 - r_f r_b e^{i2\beta_1 \omega l} G), \tag{5.93}$$

$$T_{12}(\omega) = e^{i(\beta_1 \omega l + \phi_{tb} - \phi_{t'f})} t_b t'_f M_{f12} / (1 - r_f r_b e^{i2\beta_1 \omega l} G), \tag{5.94}$$

$$\begin{aligned} R_{11}(\omega) &= e^{i(2\beta_1 \omega l + \phi_{tf} + \phi_{t'f})} t_f t'_f r_b (e^{-i\psi_{rb}} M_{f21} M_{b12} + e^{i\psi_{rb}} M_{f11} M_{b11}) \\ &\quad / (1 - r_f r_b e^{i2\beta_1 \omega l} G). \end{aligned} \tag{5.95}$$

$$\begin{aligned} R_{12}(\omega) &= e^{i(2\beta_1 \omega l + \phi_{tf} - \phi_{t'f})} t_f t'_f r_b (e^{-i\psi_{rb}} M_{f22} M_{b12} + e^{i\psi_{rb}} M_{f12} M_{b11}) \\ &\quad / (1 - r_f r_b e^{i2\beta_1 \omega l} G). \end{aligned} \tag{5.96}$$

Now it is easy to see that the frequency response of these coefficients consists of fast oscillations at about the mode spacing determined by the term $e^{i2\beta_1 \omega l}$ in the denominator while the upper and lower bounds are determined by setting the denominator equal to $1 \mp r_f r_b |G(\omega)|$, respectively. Figure 5-7 shows the upper and lower bounds of the frequency response of these coefficients by plotting $|T_{11}(\omega)|/(t_b t'_f)$, $|T_{12}(\omega)|/(t_b t'_f)$, $|R_{11}(\omega)|/(t_f t'_f r_b)$ and $|R_{12}(\omega)|/(t_f t'_f r_b)$ for the case in which $r_f r_b = 4\%$. As the instability threshold approaches, the upper-bound goes to infinity, resulting in large amplification of the probe field.

It should be noticed that A_{10} and A_{20} refer to the steady-state fields inside the cavity, which are related to the input pump fields outside the boundaries A_{1i} and A_{2i} by the boundary relations

$$A_{10} = A_{1i} t'_f \exp(i\phi_{t'f}) + A_{20} \exp(il\Delta_2) r_f \exp(i\phi_{rf}), \tag{5.97}$$

$$A_{20} = A_{2i} t'_b \exp(i\phi_{t'b}) + A_{10} \exp(il\Delta_1) r_b \exp(i\phi_{rb}). \tag{5.98}$$

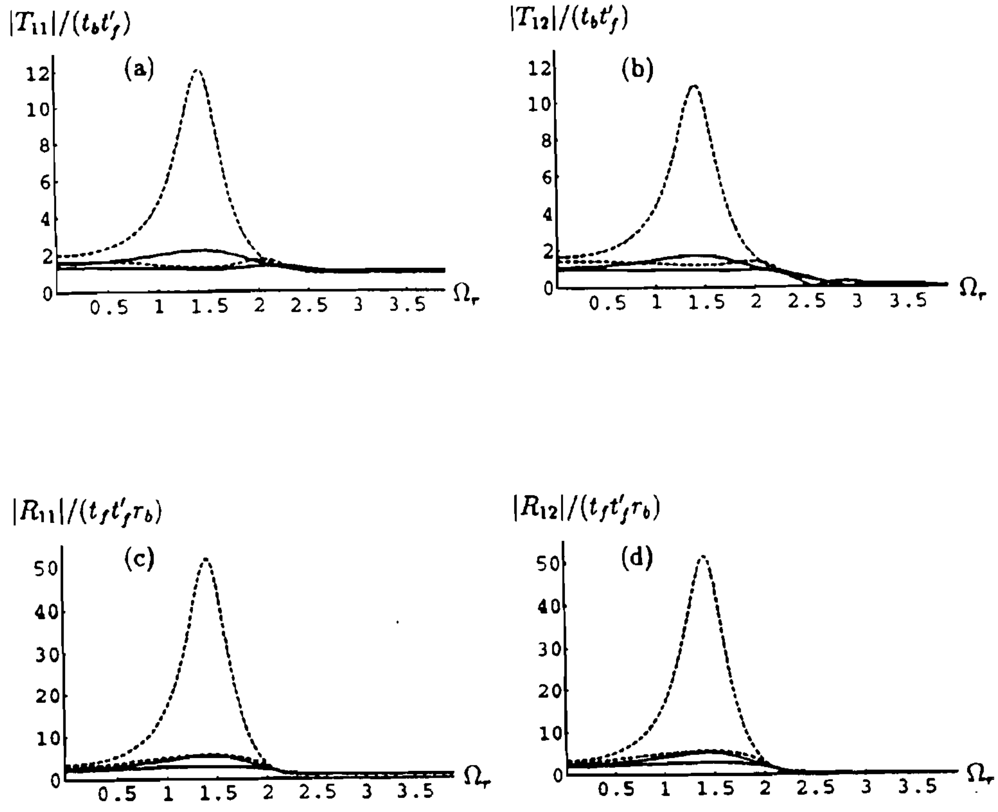

Figure 5-7: The frequency response of the nonlinear dispersive FP cavity. (a) The transmission coefficient at the frequency of the probe. Only the upper and lower envelopes are shown here; the fast oscillations on the scale of the mode spacing are not shown. $r_f r_b = 4\%$. The solid curves are the upper and lower envelopes for $L = 1$, and the dashed curves are for $L = 1.5$. Other parameters are the same as in Fig. 5-5(a). (b) Same as (a), except that the transmission coefficient at the FWM frequency is displayed. (c) Same as (a), except that the reflection coefficient is displayed. (d) Same as (a), except that the reflection coefficient at the FWM frequency is displayed.

These relations can be used to calculated A_{1i} and A_{2i} from A_{10} and A_{20}, or vice versa. The multistable behavior associated with this type of equation has been studied extensively[11,80] and is not the main focus here. When the boundary reflection is relatively weak, we simply have $A_{10} = A_{1i} t'_f \exp(i\phi_{t'f})$ and $A_{20} = A_{2i} t'_b \exp(i\phi_{t'b})$, where we have assumed $|A_{2i}| t'_b r_f \ll |A_{1i}| t'_f$, $|A_{1i}| t'_f r_b \ll |A_{2i}| t'_b$ and $r_f r_b \ll 1$.

5.7 Conclusions

In conclusion, we analytically studied the system of cw counterpropagating pump waves in a finite dispersive Kerr medium. We showed that for small modulational frequencies, such that the walkoff length is less or comparable to the nonlinear length, the system can be considered dispersionless since the dispersion length is normally much longer than the nonlinear length in such cases.

In order to study the effect of GVD, we concentrated on the case in which this condition is not satisfied and found that the coupling between the two counterpropagating pairs of sidebands is very weak. This is because when dispersion is important (i.e. when the dispersion length is comparable to the nonlinear length), the walkoff length is so short that the counterpropagating pairs do not stay together long enough to interact strongly. Consequently, the evolution of each pair of sidebands is basically determined by the corresponding pump wave alone, which provides a coupling between its sidebands through the combined action of SPM and GVD. The effect of the counterpropagating pump wave is to provide a weak backscattered (or DFB) component to the pair's propagation, induced by XPM. The model we developed based on the analysis turned out to be a generalization of the treatment of DFB lasers with a large detuning, to the case of a doubly-resonant parametric oscillator for a pair of coupled photons.

We first concentrated on the case in which the weak boundary reflection is less or comparable to the DFB. We found that for absolute instabilities to occur, anomalous dispersion is needed to provide sufficient gain from MI. Each longitudinal supermode of the absolute instability consists of two counterpropagating pairs of sidebands, corresponding to pulsing in the output field. Analytical results were obtained easily from the simple physical model we constructed. Both the growth rate versus mode frequency and the threshold conditions were given. The mode spacing can be considered continuous under the growth rate curve. In the special case of identical pump waves with no boundary reflections, our results agree with previous numerical work.

We then considered a stronger boundary reflection for which the DFB due to the scattering of the counterpropagating pumps waves were neglected compared to the localized mirror feedback. The system behavior is governed by the coupling of copropagating sidebands and the boundary reflections. This result can be interpreted in terms of a FP doubly-resonant parametric oscillator for a pair of coupled photons. This physically transparent model allows the complicated system to characterized in a simple and familiar language.

For strong boundary reflections, absolute instabilities were found to occur in both the normal and the anomalous dispersion regimes, and were described by gain curves in the modulational frequency domain. As for the weak and anti-reflection cases, the discrete supermode frequencies likely to become unstable are almost continuously distributed under the gain curve. An analytical expression was derived for the growth (damping) rate of the supermodes at different frequencies. For each unstable supermode, there are generally two sidebands due to the photon pair, which beat to cause pulsing in the field intensity. While the instability at low modulational frequencies corresponds to the conventional Ikeda instability, new instability regions were found that owe their existence to finite dispersion. For high pump powers or large medium lengths, the instability driven by the MI gain dominates in the anomalous dispersion regime because of the exponential dependence of the gain on these parameters. For the normal dispersion regime, the contribution of the Kerr or FWM effects to the gain depends at most quadratically on these parameters.

Below threshold, we studied the transmission and reflection characteristics of the system for a weak probe. In addition to their components at the probe frequency, the transmitted and reflected beams have components at the FWM frequency due to the sideband coupling. The transmission and reflection coefficients were obtained analytically. Their frequency response consists of fast oscillations at about the mode spacing of the system with an envelope that varies slowly on the same scale as the gain curve. As the threshold approaches, the upper bound of the envelope increases dramatically, resulting in large amplification.

Chapter 6

Incoherence Aspects of Nonlinear Dispersive Waves

6.1 Introduction

When a partially coherent electromagnetic field propagates through a medium, its coherence properties usually change.[16,17,56,57,59,81,82] More specifically, the output power spectrum and relative intensity noise (RIN) may differ substantially from the input power spectrum and RIN associated with the stationary stochastic field. The transformation between the input and the output power spectra is a basic statistical property for many systems. For a linear system, the spectral transformation is related to the impulse-response function and can be calculated easily by using the Wiener-Khinchin theorem.[83,84] In this chapter, we consider an optical field propagating through a single-mode optical fiber as an example of a nonlinear dispersive medium. The deterministic transformation of the input signal, in this case an optical field, is governed by a nonlinear Schrodinger equation (NSE), which takes into account group velocity dispersion (GVD) and the Kerr-type nonlinearity responsible for self-phase modulation [see Eq. (6.1)].[12,60] Thus, the statistical properties of the output signal, such as the power spectrum and RIN, are determined not only by the statistics of the input signal but also by the dispersive and nonlinear properties of the fiber.[57]

In such systems, there exists an intrinsic frequency for a given average power of propagation that allows a direct comparison between the dispersive and nonlinear terms in the NSE. This frequency corresponds to the peak-gain frequency of the modulational instability (MI) in the anomalous dispersion regime,[12,60] and is also a useful parameter in the normal dispersion regime. Here the power used for calculating this frequency refers to the average power of the stationary stochastic field. If the spectral width is much larger that this intrinsic frequency, the nonlinear term can be neglected and the system can be considered linear to the first order of approximation. It is easy to see that the Wiener-Khinchin theorem predicts no change in the power spectrum in this case. On the other hand, the dispersive term can be neglected if the spectral width is much smaller than this intrinsic frequency. For systems with negligible dispersion, the problem of spectral evolution has been studied for an input field with Gaussian statistics.[56]

Generally, the coexistence of dispersion and self-phase modulation makes the problem of stochastic propagation impossible to study analytically.[57] If, however, the input consists of a continuous-wave (CW) field plus a small noise field whose amplitude is much smaller than that of the CW field, then the problem can be linearized, with the small field treated as perturbation. This case is considered in detail in Sec. 6.2, where analytical expressions for the evolution of the power spectrum and RIN are given and are confirmed by numerical simulation.[54] It should be pointed out that the linearization method was first developed to study squeezing in quantum optics.[85–87] Here, we are concerned with the classical case.

In the spectral domain, the linearizable case corresponds to an input power spectrum that consists of a δ-function portion plus a small part whose area is much smaller than the area of the δ-function portion. In practice, our analysis applies to a laser light with a small component of broad-band background noise. It can also be applied to the case of four-wave mixing (FWM)[12] of a partially coherent (broad-band) signal in the presence of a CW pump. Since, without the small perturbation, the CW pump spectrum is unchanged, the linearization method used here gives only the pump effects on the propagation of a partially coherent field in a nonlinear dispersive medium. It is well known that MI occurs in the anomalous dispersion regime. Thus, our results will provide a statistical description of MI.

Note that not all kinds of incoherence can be decomposed as a combination of a small amplitude noise and a coherent component. Specifically, this is true for the important case in which the pump beam has a finite spectral width. Even for a narrow bandwith, it only means the noise is slow instead of being small. In Sec. 6.3 the evolution of the spectrum of an input pump beam with finite bandwith is studied by numerical simulation of two kinds of noise.[55] The main results of this chapter are summarized in Sec. 6.4.

6.2 Pump-wave effects on the propagation of noisy signals in nonlinear dispersive media

6.2.1 Noise propagation

The governing NSE can be written as[12]

$$\partial_z A = -\frac{i}{2}\beta_2\partial_{tt}^2 A + i\gamma|A|^2 A. \tag{6.1}$$

where A is the complex field amplitude, z is the propagation distance, t is the retarded time measured in a frame moving at the group velocity, β_2 is the GVD coefficient and γ is the nonlinear coefficient. To simplify the notation, we will often use $\beta \equiv \beta_2/2$ in the following. The input field is assumed to be $A(t,0) = A_0 + \delta A(t,0)$, where $|\delta A(t,0)| \ll |A_0|$. To zeroth-order (without noise), we have the solution $A_s(t,z) = A_0\exp(i\gamma|A_0|^2 z)$. Thus, we assume a solution of the form $A(t,z) = A_s + \delta A_s = [A_0 + \delta A(t,z)]\exp(i\gamma|A_0|^2 z)$ and linearize Eq. (6.1) in the small perturbation δA to obtain the linear partial differential equation

$$\partial_z\delta A = -i\beta\partial_{tt}^2\delta A + i\gamma(|A_0|^2\delta A + A_0^2\delta A^*). \tag{6.2}$$

The solution to this equation is easily expressed in Fourier domain. By taking the Fourier transforms of the above equation and its complex conjugate, we have

$$\begin{aligned}
&[d_z - i\beta\omega^2 - i\gamma|A_0|^2]\overline{\delta A}(\omega,z) = i\gamma|A_0|^2 A_0^2\overline{\delta A}^*(-\omega,z)\\
&[d_z + i\beta\omega^2 + i\gamma|A_0|^2]\overline{\delta A}^*(-\omega,z) = -i\gamma|A_0|^2 A_0^2\overline{\delta A}(\omega,z)
\end{aligned} \tag{6.3}$$

where $\overline{\delta A}$ refers to the Fourier transform of δA [i.e. $\overline{\delta A}(\omega) = \int_{-\infty}^{\infty}\delta A\exp(i\omega t)dt$]. These equations show that the basic physics is related to FWM, which causes coupling between the two sidebands $\overline{\delta A}(\omega, z)$ and $\overline{\delta A}^*(-\omega, z)$ located symmetrically around the CW pump frequency.

It is easy to obtain the general solution of the above coupled, linear, first-order, ordinary differential equations. For each ω, there are two independent solutions. Thus, in terms of the two eigenmodes, the general solution is given by

$$\begin{pmatrix} \overline{\delta A}(\omega, z) \\ \overline{\delta A}^*(-\omega, z) \end{pmatrix} = c_1 \begin{pmatrix} 1 \\ r_+ \end{pmatrix} e^{ik_+ z} + c_2 \begin{pmatrix} r_- \\ 1 \end{pmatrix} e^{ik_- z}. \tag{6.4}$$

where c_1 and c_2 are constants, and $k_\pm$ and $r_\pm$ are defined by

$$k_\pm(\omega) = \pm\sqrt{(\gamma|A_0|^2 + \beta\omega^2)^2 - (\gamma|A_0|^2)^2}. \tag{6.5}$$

$$r_+(\omega) = \frac{k_+(\omega) - \beta\omega^2 - \gamma|A_0|^2}{\gamma A_0^2} = -\frac{\gamma A_0^{*2}}{k_+(\omega) + \beta\omega^2 + \gamma|A_0|^2}, \tag{6.6}$$

and

$$r_-(\omega) = \frac{\gamma A_0^2}{k_-(\omega) - \beta\omega^2 - \gamma|A_0|^2} = -\frac{k_-(\omega) + \beta\omega^2 + \gamma|A_0|^2}{\gamma A_0^{*2}}. \tag{6.7}$$

Here $r_\pm(\omega)$ are the relative amplitudes of the sidebands $\overline{\delta A}(\omega, z)$ and $\overline{\delta A}^*(-\omega, z)$ for each eigenmode, and $k_\pm(\omega)$ represents the corresponding dispersion relation.

If the field at the input $z = 0$ is known, Eq. (6.4) can be used to determine the two constants c_1 and c_2, and the field within the fiber can be expressed in terms of the input. After some straightforward algebra, we obtain

$$\begin{pmatrix} \overline{\delta A}(\omega, z) \\ \overline{\delta A}^*(-\omega, z) \end{pmatrix} = \begin{pmatrix} M_{11}(\omega, z) & M_{12}(\omega, z) \\ M_{21}(\omega, z) & M_{22}(\omega, z) \end{pmatrix} \begin{pmatrix} \overline{\delta A}(\omega, 0) \\ \overline{\delta A}^*(-\omega, 0) \end{pmatrix}, \tag{6.8}$$

where

$$\begin{aligned}
M_{11} &= (e^{ik_+z} - r_+r_-e^{ik_-z})/(1 - r_+r_-),\\
M_{12} &= r_-(e^{ik_-z} - e^{ik_+z})/(1 - r_+r_-).\\
M_{21} &= r_+(e^{ik_+z} - e^{ik_-z})/(1 - r_+r_-).\\
M_{22} &= (e^{ik_-z} - r_+r_-e^{ik_+z})/(1 - r_+r_-).
\end{aligned} \tag{6.9}$$

6.2.2 Power spectrum of the field

From the Wiener-Khinchin theorem,[83] the power spectrum $S(\omega, z)$, defined as the Fourier transform of the autocorrelation of the field, can be calculated as

$$\begin{aligned}
&S(\omega, z) = \langle|\overline{A_s} + \overline{\delta A_s}|^2\rangle/T\\
&= \langle|\overline{A_s}|^2\rangle/T + \langle\overline{A_s\delta A_s}^* + \overline{A_s}^*\overline{\delta A_s}\rangle/T + \langle|\overline{\delta A_s}|^2\rangle/T\\
&= |A_0|^2\delta(\omega) + \langle|\overline{\delta A}(\omega, z)|^2\rangle/T,
\end{aligned} \tag{6.10}$$

where the time window T extends to inifinity as the limit. The cross term vanishes after averaging since $\overline{A_s}$ can be moved out of the average and $\langle\delta A_s\rangle = 0$.

Define $\Delta S(\omega, z) \equiv S(\omega, z) - |A_0|^2\delta(\omega)$, i.e. remove the unchanged portion of the spectrum corresponding to the CW signal . Since $\overline{\delta A}(\omega, z)$ can be calculated from Eq. (6.8), we have

$$\begin{aligned}
\Delta S(\omega, z) &= \langle|M_{11}\overline{\delta A}(\omega, 0) + M_{12}\overline{\delta A}^*(-\omega, 0)|^2\rangle/T\\
&= |M_{11}|^2\Delta S(\omega, 0) + |M_{12}|^2\Delta S(-\omega, 0),
\end{aligned} \tag{6.11}$$

where we have assumed $\langle\overline{\delta A}(\omega, 0)\overline{\delta A}(-\omega, 0)\rangle/T = 0$ or, equivalently, $\langle\delta A(t, 0)\delta A(t+\tau, 0)\rangle = 0$, which is true in most cases. The above equation is a linear transformation between the spectrum ΔS at the output and the input. Both sidebands participating in the FWM process contribute to the output.

After further simplification, the output spectrum is given by

$$\Delta S(\omega, z) = \\ \Delta S(\omega, 0) + (\gamma|A_0|^2)^2[\Delta S(\omega, 0) + \Delta S(-\omega, 0)] \sin^2[k(\omega)z]/[k(\omega)]^2, \qquad (6.12)$$

where k is given by Eq. (6.5) regardless of the sign convention. Notice that when k is imaginary, corresponding to MI, $\sin^2[k(\omega)z]/k^2(\omega) = (1/4)[\exp(|k|z) - \exp(-|k|z)]^2/|k|^2$.

Equation (6.12) predicts no spectral change in the limit of weak pump power, consistent with the result for a linear dispersive system. In the limit of zero dispersion, Eq. (6.12) becomes

$$\Delta S(\omega, z) = \Delta S(\omega, 0) + (z\gamma|A_0|^2)^2[\Delta S(\omega, 0) + \Delta S(-\omega, 0)] \qquad (6.13)$$

which is valid as long as z is small enough that the noise power remains much smaller than the pump power.

Figures 6-1 and 6-2 display the output spectrum at different distances for a symmetric input spectrum, for the cases of normal and anomalous dispersion, respectively. Notice that even in the normal dispersion region where MI does not occur, the nonlinear dispersive effects greatly affect the spectral evolution. From Eq. (6.12), the spectral intensity at any frequency oscillates with distance (except at zero frequency where it grows as z^2) due to the factor $\sin^2[k(\omega)z]/[k(\omega)]^2$. The period is $1/k(\omega)$, which is longer for smaller frequencies and goes to infinity at zero frequency. Thus, the frequency components around zero keep growing while fringes are formed on the spectrum. At a fixed distance, the power spectrum

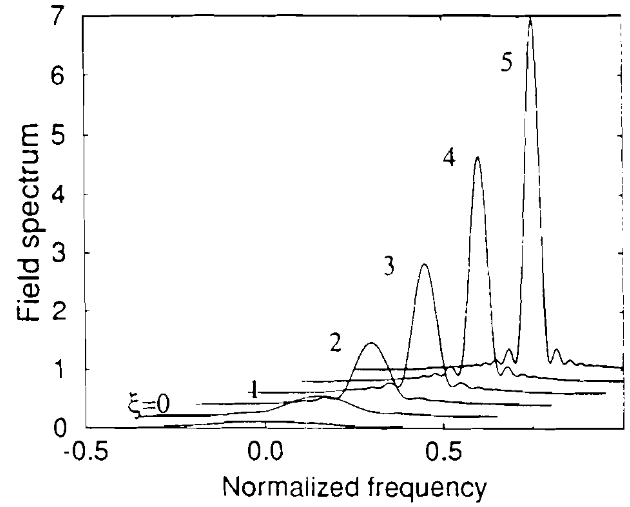

Figure 6-1: The spectral evolution at different distances in the normal-dispersion region for a symmetric input spectrum. FWM causes the quadratic growth and fringe formations. The distance is normalized to $\xi = z\gamma|A_0|^2$ and the frequency is normalized as $\omega\ [|\beta_2|/(\gamma|A_0|^2)]^{1/2}\ /(4\pi)$. The FWHM of the input noise spectrum is 0.4, its average intensity is 3.2×10^{-5} times of the pump intensity. The vertical axis has a relative unit.

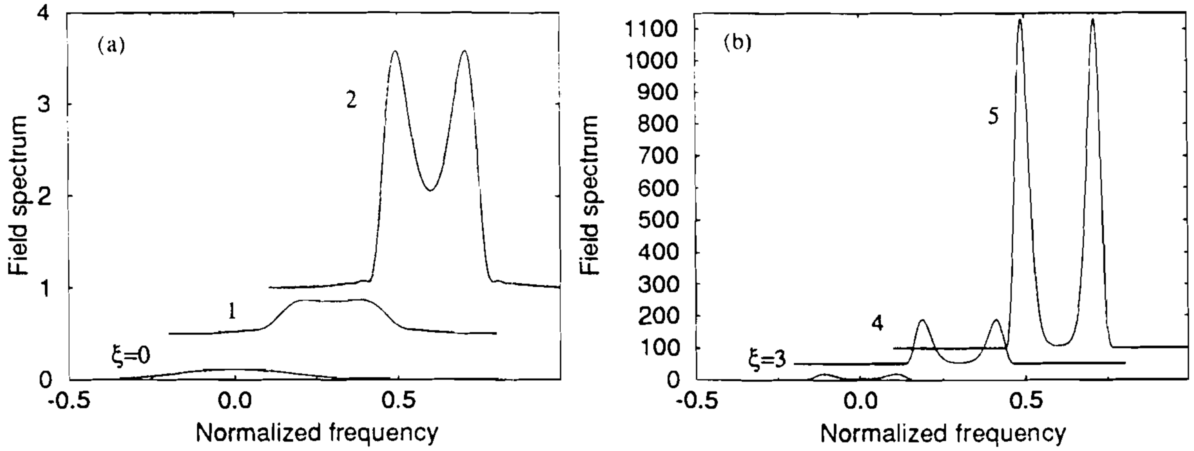

Figure 6-2: Same as Fig. 6-1 except for the sign of the GVD parameter. MI effects dominate at large distance.

is a oscillating function of frequency. The oscillations become faster at larger distances [see Eq. (6.12), and also Fig. 6-9 below]. The formation of the fine fringes indicate a very long correlation time (since the autocorrelation of the field is just the Fourier transform of this spectrum) even if it is short at the input. This is an interesting statistical phenomenon since it seems to indicate that the input field becomes more coherent after propagation because of pump-induced FWM. The quadratic growth of the field spectrum near the zero frequency where the dispersion is negligible can also be explained in terms of self-phase modulation since the total field can then be written as $[A_0+\delta A(t,0)]\exp[i\gamma|A_0+\delta A(t,0)|^2 z] \simeq A_s + \delta A(t,0)\exp[i\gamma|A_0|^2 z] + i\gamma A_0 z[A_0\delta A(t,0)^* + c.c]$ where the term linear in z causes the quadratic power-spectrum growth.

In the anomalous dispersion region and at large distances, the exponential growth due to MI dominates. For this case, Eq. (6.12) can be written as

$$\Delta S(\omega, z) = (\gamma|A_0|^2)^2[\Delta S(\omega, 0) + \Delta S(-\omega, 0)]\exp(2|k|z)/(2|k|)^2 \qquad (6.14)$$

for large z. The output spectrum is symmetric, independent of the symmetry of the input. If the input spectrum is broad enough (as is in Fig. 6-2), the two peaks are at the frequency of the peak gain of MI, which is the maximum of $|k(\omega)|$ at $\omega = \pm\sqrt{\gamma|A_0|^2/\beta}$. The linear approximation will eventually break down when the noise amplitude becomes comparable to the pump amplitude.

In order to confirm of the validity of the linear approximation, we have also performed numerical simulations by assuming Gaussian statistics[84] for the input field. Our numerical model is constructed as follows: For the noise field, two independent Gaussian random number generators are used as the real and the imaginary parts of the input field after going through a filter which determines the shape of spectrum. This is added to the CW field to form the input field. Eq. (6.1) is solved for each preparation of the input. using the split-step Fourier method.[12] In order to avoid complications at the temporal boundaries, a broad Gaussian-pulse carrier is used whose width is much larger than the time scale of fluctuations, and the non-stationary effects introduced by the carrier are eliminated by applying a smaller window (than the pulse width) for calculating the power spectrum and the RIN. The results are averaged over 100 realizations by integrating the NSE 100 times.

Figures 6-3 and 6-4 show the numerically-determined spectral evolutions corresponding to Figs. 6-1 and 6-2. The analytical results agree with the numerical simulations, although deviations begin to occur for large distances in the anomalous case when the amplitude of the noise field becomes comparable to the pump amplitude due to MI. The appearance of additional peaks in the spectrum, which we attribute to higher-order FWM effect, also indicates that our analytical treatment becomes invalid.

6.2.3 Relative intensity noise

Besides the autocorrelation or the power spectrum of the field, another quantity of statistical importance is the RIN. It is defined as the Fourier transform of the autocorrelation of the relative intensity fluctuation $\delta I/\langle I\rangle$ of the field, where $\delta I = I - \langle I\rangle$ and $I = |A|^2$ is the intensity. Thus it is related to the fourth-order moment of the stochastic field. In our case, $I = |A_0 + \delta A(t,z)|^2$. Consistent with the linear approximation, this leads to

$$\delta I(t,z)/\langle I\rangle = [A_0^*\delta A(t,z) + A_0\delta A^*(t,z)]/|A_0|^2. \tag{6.15}$$

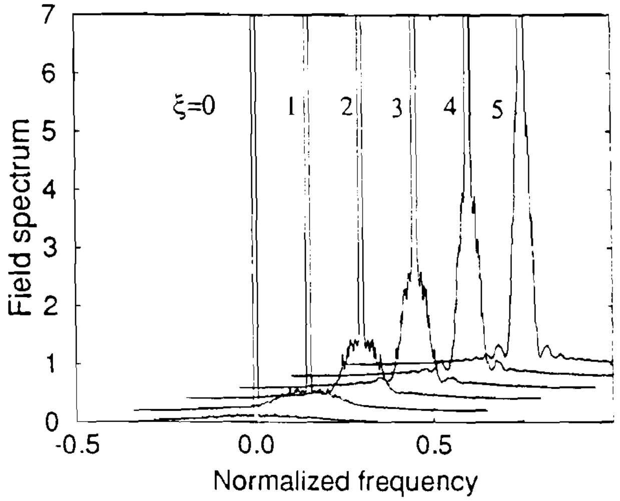

Figure 6-3: Numerical simulations corresponding to Fig. 6-1. The center portion is the CW spectrum, which is subject to finite resolution due to the finite temporal window used to calculate the spectrum. The sign of the GVD parameter is positive

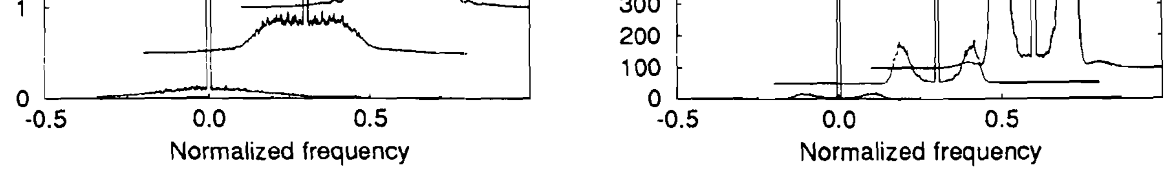

Figure 6-4: Same as Fig. 6-3 except that the sign of the GVD parameter is negative.

By using the Wiener-Khinchin theorem, we find the RIN to be

$$\mathrm{RIN}(\omega, z) = \langle |A_0^* \overline{\delta A}(\omega, z) + A_0 \overline{\delta A}^*(-\omega, z)|^2 \rangle / (T|A_0|^4) \tag{6.16}$$

By using Eq. (6.8), we obtain.

$$\begin{aligned} \mathrm{RIN}(\omega, z) &= |A_0^* M_{11} + A_0 M_{21}|^2 \langle |\overline{\delta A}(\omega, 0)|^2 \rangle / (T|A_0|^4) \\ &\quad + |A_0^* M_{12} + A_0 M_{22}|^2 \langle |\overline{\delta A}(-\omega, 0)|^2 \rangle / (T|A_0|^2) \\ &= |A_0^* M_{11} + A_0 M_{21}|^2 \Delta S(\omega, 0) / |A_0|^4 \\ &\quad + |A_0^* M_{12} + A_0 M_{22}|^2 \Delta S(-\omega, 0) / |A_0|^4. \end{aligned} \tag{6.17}$$

Further simplification gives

$$\mathrm{RIN}(\omega, z) = |A_0|^{-2} [\Delta S(\omega, 0) + \Delta S(-\omega, 0)] \{1 - \frac{2\gamma |A_0|^2 \sin^2 [k(\omega) z]}{2\gamma |A_0|^2 + \beta \omega^2}\}. \tag{6.18}$$

where k is given by Eq. (6.5) regardless of the sign convention. From this equation we have $\mathrm{RIN}(\omega, 0) = |A_0|^{-2}[\Delta S(\omega, 0) + \Delta S(-\omega, 0)]$, indicating that the RIN is always symmetric at the input. The final result is thus,

$$\mathrm{RIN}(\omega, z) = \mathrm{RIN}(\omega, 0) \{1 - \frac{2\gamma |A_0|^2 \sin^2 [k(\omega) z]}{2\gamma |A_0|^2 + \beta \omega^2}\}. \tag{6.19}$$

This is a linear transformation between the RIN of the input and the output. Eq. (6.19) also predicts that without nonlinearity or dispersion (i.e., $|A_0|^2 = 0$ or $\beta_2 = 0$), the RIN will not change (in the linear approximation).

Figures 6-5 and 6-6 show the evolution of the RIN corresponding to the cases of Figs. 6-1 and 6-2, respectively. Figs. 6-7 and 6-8 are the corresponding numerical-simulation results. Like the power spectrum, even in the normal dispersion region where there is no MI, nonlinear dispersive effects change the RIN. Because of

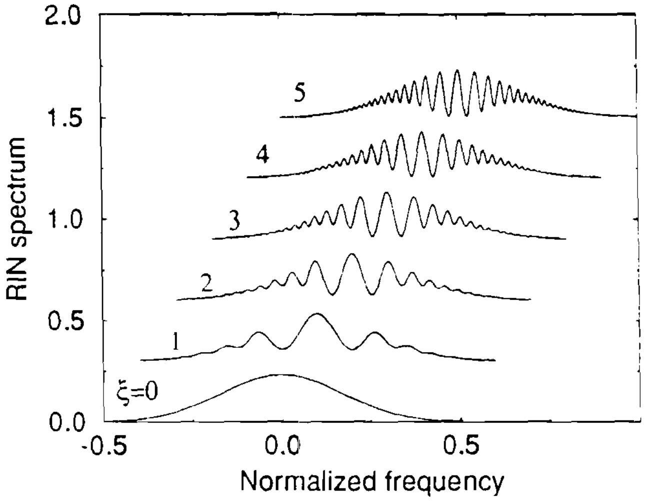

Figure 6-5: Analytic RIN spectra at different distances in the normal dispersion region under conditions identical to Fig. 6-1. FWM causes fringe formation.

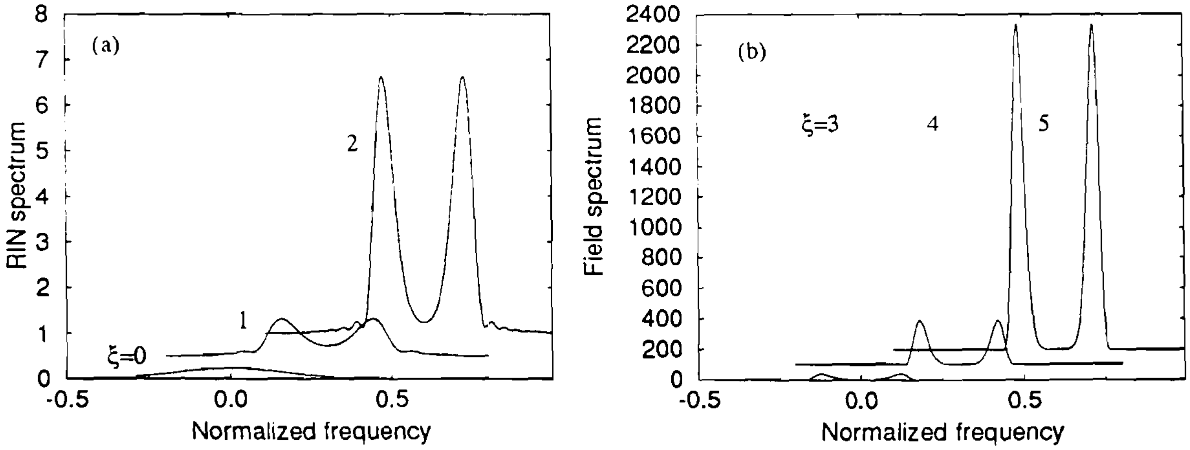

Figure 6-6: Same as Fig. 6-5 except that the dispersion is anomalous. MI effects dominate at large distances.

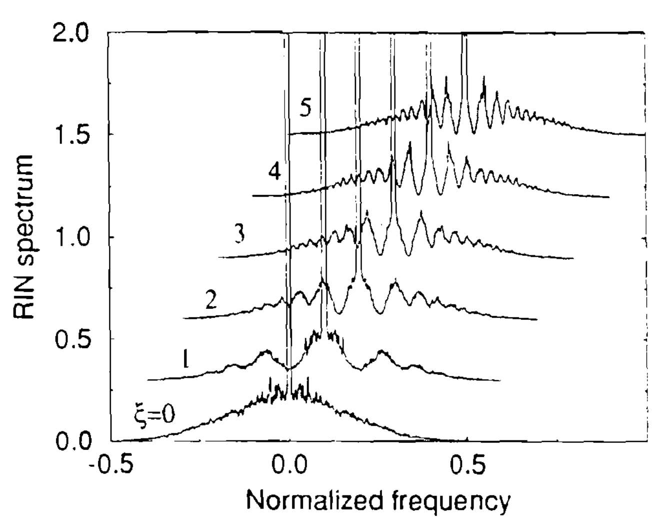

Figure 6-7: Numerical simulation result corresponding to Fig. 6-5. The GVD parameter is positive. The center portions of the specctra are the CW residue.

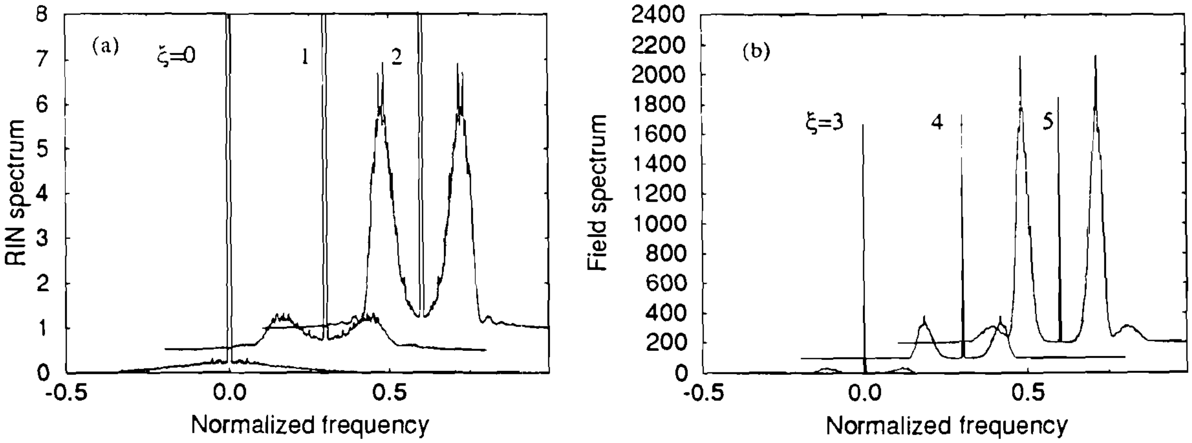

Figure 6-8: Same as Fig. 6-7 except that the sign of GVD parameter is negative.

the factor $\sin^2[k(\omega)z]/(2\gamma|A_0|^2 + \beta\omega^2)$ in Eq. (6.19), the RIN at any frequency is oscillating with distance, except at zero frequency where the RIN is always unchanged . The period $1/k(\omega)$ is longer for smaller frequencies and it goes to infinity at the zero frequency. Thus, the RIN at zero frequency is unchanged while fringes will be formed at other frequencies. For a fixed distance, the power spectrum is a oscillating function of frequency and the oscillation becomes faster at larger distances. The numerical simulation confirms our analysis.

In the anomalous dispersion region and at large distances, the MI will dominate, since for large z, Eq. (6.19) can be written as

$$\mathrm{RIN}(\omega, z) = \mathrm{RIN}(\omega, 0)\frac{\gamma|A_0|^2\exp(2|k|z)}{4\gamma|A_0|^2 + \beta_2\omega^2}, \tag{6.20}$$

indicating an exponential increase due to the MI gain. If the input spectrum is broad enough (as it is in our example), the two peaks are at the frequency of the peak MI gain, $\omega = \pm\sqrt{2\gamma|A_0|^2/\beta_2}$. The linear approximation will eventually break down at extremely large z when the noise amplitude becomes comparable to the pump amplitude. This is evident from the numerical simulations in which the appearance of additional peaks on the RIN occurrs because of higher-order FWM effects.

6.2.4 Noise-induced four-wave mixing

Four-wave mixing occurs when a CW pump wave and a weak signal or probe wave (usually with a different carrier frequency) coexist in a nonlinear medium.[12] It has found many applications, including the use of its phase-conjugation effect to cancel the dispersive spreading of optical pulses in a fiber link for a broad-band communication system.[88-90] In many cases, it is important to understand the statistical properties of the fields after undergoing FWM, such as the shape of the field spectrum and the correlation time. Although it was developed in a different context, our formalism for the propagation of a stochastic field is well suited to describe FWM. In fact, Eq. (6.12) can be applied directly to the case of FWM in which a CW pump and a weak noisy or broad-band probe are present at the input. In our linear approximation, the CW pump is undepleted. Since Eq. (6.12) is a linear transformation between spectrum of the nonpump part at the input and output, we first consider a probe with a narrow spectrum centered on ω' at the input, i.e., $\Delta S(\omega, 0) = I_+(0)\delta(\omega - \omega')$, where $I_+(0)$ is a constant. From Eq. (6.12), we have

$$\Delta S(\omega, z) = I_+(z)\delta(\omega - \omega') + I_-(z)\delta(\omega + \omega'), \tag{6.21}$$

where

$$\begin{aligned} I_+(z) &= I_+(0)[1 + (\gamma|A_0|^2)^2 \sin^2[k(\omega')z]/[k(\omega')]^2], \\ I_-(z) &= I_+(0)(\gamma|A_0|^2)^2 \sin^2[k(\omega')z]/[k(\omega')]^2. \end{aligned} \tag{6.22}$$

This equation describes the FWM generation of the sideband at $-\omega'$ or idler due to the coupling to the sideband at ω'.

Notice that in the weak-pump limit, i.e. $\gamma|A_0|^2 \ll |k(\omega')|$, the sideband at $-\omega'$ is not generated since there is no coupling in this limit. In the case of zero GVD, the coupling behavior also changes, and Eq. (6.12) leads to

$$\begin{aligned} I_+(z) &= I_+(0)[1 + (z\gamma|A_0|^2)^2] \\ I_-(z) &= I_+(0)(z\gamma|A_0|^2)^2. \end{aligned} \tag{6.23}$$

These equations cease to be valid when $I_\pm$ becomes comparable to $|A_0|^2$.

In the normal-dispersion case, I_+ and I_- exhibit in-phase oscillations with the propagation distance, with a period $1/k(\omega')$ that is longer at lower frequencies. In the anomalous dispersion case, $I_+(z) \sim I_-(z) \sim I_+(0)(1/4)(\gamma|A_0|^2)^2 \exp(2|k|z)/|k|^2$ at large distances, with the exponential growth caused by the MI gain.

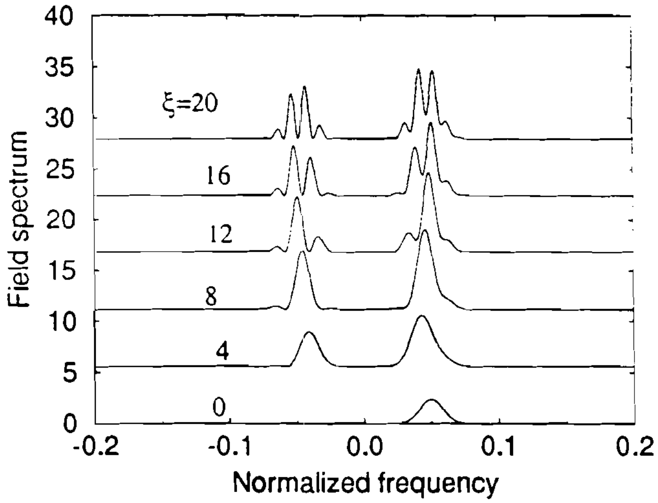

Figure 6-9: Spectral evolution at different distances in the normal dispersion region for an asymmetric input spectrum corresponding to FWM with a noisy probe. The noise spectrum is centered at 0.05 with FWHM=0.02 and the other parameters are identical to those of Fig. 6-1. The GVD is normal

Figures 6-9 and 6-10 show the spectral evolution associated with FWM induced by a probe of finite bandwidth for the cases of normal and anomalous dispersion, respectively. A Gaussian probe spectrum is assumed: $\Delta S(\omega, 0) \propto \exp -[(\omega - \omega')/\Delta\omega]^2$. With above analysis for a narrow-bandwidth probe, the qualitative behavior can be understood easily since the spectrum can be linearly decomposed into many independent narrow-bandwidth probes. In the normal dispersion region, a spectral wing is generated at the frequency that is symmetric to

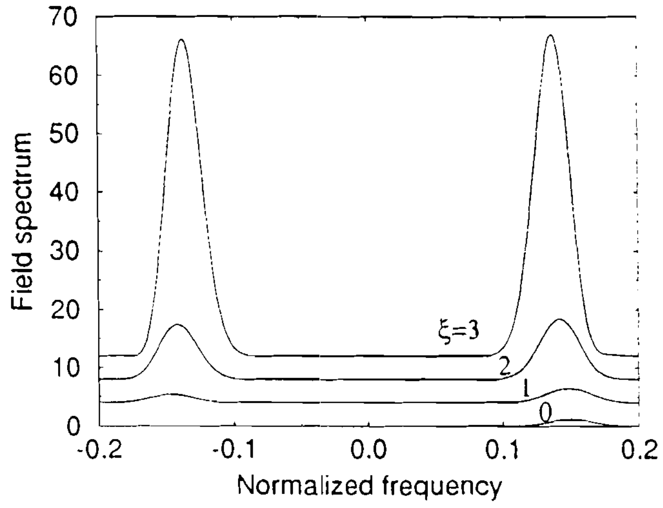

Figure 6-10: Same as Fig. 6-9 except that the noise spectrum is centered at 0.15 with FWHM=0.04 and the GVD is anomalous.

the probe frequency. Initially, the intensity oscillates with propagation distance. Since each frequency component has a different oscillation period and different initial intensity, the wings will be shifted and split to develop fringes. The average oscillation with distance will be saturated as more and more fringes appear, since they are all out of phase with each other. In fact, for large distance the envelope of the two wings settles down at frequencies around $\pm\omega'$, with average intensities that is proportional to $[1 + (\gamma|A_0|^2)^2/k^2(\omega)] \exp -[(\omega - \omega')/\Delta\omega]^2$ and $[(\gamma|A_0|^2)^2/k^2(\omega)] \exp -[(\omega + \omega')/\Delta\omega]^2$, respectively. It is the inverse width of the fringes under the envelope that gives the approximate correlation time. Thus, the coherent time of the noisy signal and idler keep increasing as they propagate. In the anomalous dispersion case, MI will produce symmetric wings at large distances. Because the gain peak is at $\pm\sqrt{2\gamma|A_0|^2/\beta_2}$, the wings will be pulled toward this frequency position as they grow with distance.

Note in both the normal and anomalous dispersion cases, the spectrum of the generated idler is not simply the mirror image of the input spectrum of the signal. This is due to the effect of GVD on the process of FWM. From a practical point of view, this phenomenon implies that midsystem spectral inversion by FWM in a dispersion-shifted fiber, a technique proposed recently for dispersion compensation in fiber-optic communication systems,[88] can be affected by the residual dispersion in the dispersion-shifted fiber. A detailed study from a systems point of view can be found elsewhere.[90]

6.3 Spectral evolution of large-amplitude noise

As was pointed out in Sec. 6.1, the noise that causes the finite bandwidth of the pump beam can not generally be treated as a small amplitude noise. The study of the propagation of a stochastic field in a nonlinear dispersive medium has not only theoretical importance but also practical implications.[56,57,82,91–93] For example, the correlation time of the optical field (which is the inverse of the FWHM of the spectrum) is very critical for short-time-resolution experiments.[94]

Although the governing equation is the well known NSE Eq. (6.1), there is no satisfactory analytical way to predict the evolution of the power spectrum of partially coherent CW light when both dispersion and nonlinearity are important. Thus numerical simulations are generally required. Previous work[57] concerned an optical field with Gaussian statistics propagating in the normal dispersion region. However, the result can not be extrapolated to fields described by other stochastic processes.

To see this, let us simply neglect dispersion and compare two kinds of stochastic field at the input, one with Gaussian statistics and the other with only phase noise.

For the Gaussian field, the previous work[56] led to analytical results showing that the spectrum is broadened on the scale of the nonlinear length L_N.[12] Using a similar approach, we can further show that the field becomes nonGaussian on the same scale.

However, a simple analysis using the NSE without the dispersion term predicts no change of spectrum for the field with only phase noise. In fact, since the intensity is a constant, the Kerr effect, which only respond to intensity, does not change the statistical properties at all during the propagation.

It is worth mentioning that the spectral evolution of a small additive noise to a coherent CW wave in a nonlinear dispersive medium is also on the scale of the nonlinear length.[54]

In this section, we consider input fields with two common statistics, a Gaussian process that corresponds to a thermal field and a diffusing-phase process that corresponds to laser light, and study their propagation in both the normal and anomalous dispersion regions of a fiber, as an example of a nonlinear dispersive medium. The parameter regions of the problem are classified and weak turbulence theory[58] is reviewed. The results from numerical simulations for strong-turbulence parameters are then presented and discussed.

6.3.1 Classification of the parameter regions

The governing NSE which relates the input and output field is shown in Eq. (6.1) Thus, the statistical properties of the output field, such as the power spectrum, are determined not only by the statistics of the input field but also by the dispersive and nonlinear properties of the fiber.

Since the coefficients of the NSE are time independent, it is easy to prove that if the input field is a stationary (CW) process, it will always remain a stationary process with the same average intensity, $\langle |A|^2 \rangle = P$. We define the nonlinear length and dispersion length as $L_N = 1/\gamma P$ and $L_D = 2/[|\beta_2|(\pi\Delta\nu)^2]$, respectively, where $\Delta\nu$ is the FWHM of the power spectrum. Furthermore, we define a frequency $\nu_N = \sqrt{|2\gamma P/\beta_2|}/2\pi$, which corresponds to the peak growth frequency of modulational instability (MI) if a coherent field with same power in the anomalous region were considered. By working in the normalized variables $\overline{t} = \pi\Delta\nu t$, $\overline{z} = z/L_D$ and $\overline{A} = A/\sqrt{P}$, we have the following equation:

$$\partial_{\overline{z}}\overline{A} = -i\mathrm{sign}(\beta_2)\partial^2_{\overline{tt}}\overline{A} + i\frac{L_D}{L_N}|\overline{A}|^2\overline{A}. \tag{6.24}$$

where the magnitude of $\overline{A}$ is the order of unity since $\langle |\overline{A}|^2 \rangle = 1$. The temporal scale of its variation is also the order of unity since we work in the normalized time. The only free parameter now is L_D/L_N.

We define weak turbulence by the condition

$$L_N \gg L_D \quad \text{or} \quad \Delta\nu/2 \gg \nu_N. \tag{6.25}$$

When this condition is satisfied, the nonlinear term can be neglected in the first iteration of a perturbation method. Since the power spectrum is given by $S(\omega, z) = \langle |\tilde{\overline{A}}|^2 \rangle$ according Wiener-Khinchin theorem, where $\tilde{\overline{A}} = 1/(2\pi) \int \overline{A} \exp(-i\omega\overline{t}) dt$ is the Fourier transform of $\overline{A}$, we prefer to work in Fourier space and the solution is simply $\tilde{\overline{A}}^{(0)}(\omega)\exp(i\mathrm{sign}\omega^2 z)$. Continuing the iteration, we have

$$\tilde{\overline{A}}^{(1)} = -\frac{L_D}{L_N}\iiint \tilde{\overline{A}}_1^{(0)*}\tilde{\overline{A}}_2^{(0)}\tilde{\overline{A}}_3^{(0)}\frac{\exp[-i(k_1 - k_2 - k_3)z]}{k + k_1 - k_2 - k_3}$$
$$\times\delta(\omega + \omega_1 - \omega_2 - \omega_3)d\omega_1 d\omega_2 d\omega_3,$$

where $k = \mathrm{sign}(\beta_2)\omega^2$ and $k_i = \mathrm{sign}(\beta_2)\omega_i^2$ $(i = 1, 2, 3)$.

The next iteration, which is of order $(L_D/L_N)^2$, contains a secular driving term which produces large changes in $\tilde{A}^{(0)}$ over a normalized length of order $(L_N/L_D)^2$ (or physical length of order L_N^2/L_D). By similar consideration, Haselman and Benney *et al.*[95,96] derived the equation for the power spectrum of a nonlinear dispersive water wave. In the context of our discussion, the result can be written as

$$\partial_z S = 4\pi(L_D/L_N)^2 \iiint [S_1 S_2 (S_3 + S) - S_3 S (S_1 + S_2)]$$
$$\times \delta(\omega + \omega_1 - \omega_2 - \omega_3)\delta[k + k_1 - k_2 - k_3] d\omega_1 d\omega_2 d\omega_3, \tag{6.26}$$

where $S = S(\omega, z)$ and $S_i = S(\omega_i, z)$ $(i = 1, 2, 3)$.

The physical meaning of this equation has been discussed extensively.[95,96] Here it is enough to see that it describes a stimulated process of four-photon interaction. The first term is due to the induced generation of photons and the second term is due to the induced decay of photons. Indeed, it is easy to see that this equation predicts spectral change on a spatial scale of order L_N^2/L_D, which is much slower than the L_N spatial scale obtained when $\Delta\nu = 0$ (in which case condition (6.25) is not satisfied) in.[56] In fact, the situation is much more complicated when the weak-turbulence condition is not satisfied and the scale dependends on the specific stochastic process and on whether the dispersion is normal or anomalous, as was mentioned in the introduction to this chapter. In the following section, we perform numerical simulations on two kind of input fields, one with Gaussian statistics and the other with a diffusing-phase statistics.

6.3.2 Numerical simulation and discussion

To simulate strong turbulence, it is helpful to use the normalized length $\bar{z} = z/L_N$, and time $\bar{t} = 1/(2\pi\nu_N)$, in which case the governing equation (6.1) becomes

$$\partial_{\bar{z}}\bar{A} = -i\mathrm{sign}(\beta_2)\partial^2_{\bar{t}\bar{t}}\bar{A} + i|\bar{A}|^2\bar{A}, \tag{6.27}$$

where $\langle|\bar{A}|^2\rangle = 1$. The free parameter to change in the numerical simulation is now the spectral width.

For an input field with Gaussian statistics,[84] our numerical results are obtained by a method similar to that used in Sec. 6.2. To summarize, two temporal series, corresponding to the real and imaginary part of a complex field in time, are generated by two independent Gaussian random number generators. The complex temporal field is then put through a digital filter which uses a filter function to perform a convolution on the input field. We change the FWHM of the spectrum of the filtered field (which is also a Gaussian process) by using a filter function of Gaussian shape and varying width. The filtered field is then normalized so that the average intensity is unity and the normalized field is taken to be one realization of the input field. The next realization is obtained by continued use of the Gaussian number generators and aforementioned procedure is repeated. Eq. (6.27) is solved for each realization of the input field, using the split-step Fourier method.[12] The density of grids in time has to be much larger than the maximum spectral width of the field, both at the input and during the evolution within the propagation distance considered.

In order to avoid complications at the temporal boundaries, a broad Gaussian-pulse carrier is used whose width is much larger than the time scale of fluctuations both in the input field and during propagation within the distance considered. The non-stationary effects introduced by the pulsed carrier wave will not show up if we apply a smaller temporal window (than the carrier pulse width) around the peak of the total field when calculating its Fourier transform to get the spectrum. In our case, we used a Gaussian shaped window. This temporal window limits the resolution to approximatelly its inverse width, but we make sure that we get enough resolution by using a large window. This is similar to an experiment in which the laser pulse is long and the resolution of the spectrometer is sufficiently limited that the laser can be considered CW.

According to the Wiener-Khinchin theorem, the power spectrum is obtained by averaging the intensity of the Fourier spectrum calculated for each realization. We averaged over 100 realizations by integrating the NSE 100 times. The relatively wide temporal window, high temporal grid density and large number of realizations all lead to long computation times.

In order to generate the diffusing phase process, we use the fact that the diffusing process is the integration of white noise.[84] White noise can be approximated by broadband Gaussian noise, the generation of which was described above. Then the diffusing-phase process is generated by using the diffusing process multiplied by a constant as the phase of a field of unit amplitude. As this constant effectively changes the magnitude of the white noise, the FWHM of the Lorentzian spectrum of the genearated field can be adjusted by changing the constant. The broadband Gaussian noise can be considered as white noise as long as its bandwidth is much larger than the bandwidth of the Lorentzian spectrum of the diffusing-phase process that is generated. Thus we have approximately obtained a realization of the diffusing-phase process. The remaining considerations such as grid density, carrier pulse, temporal window, and averaging are similar to the case of Gaussian statistics.

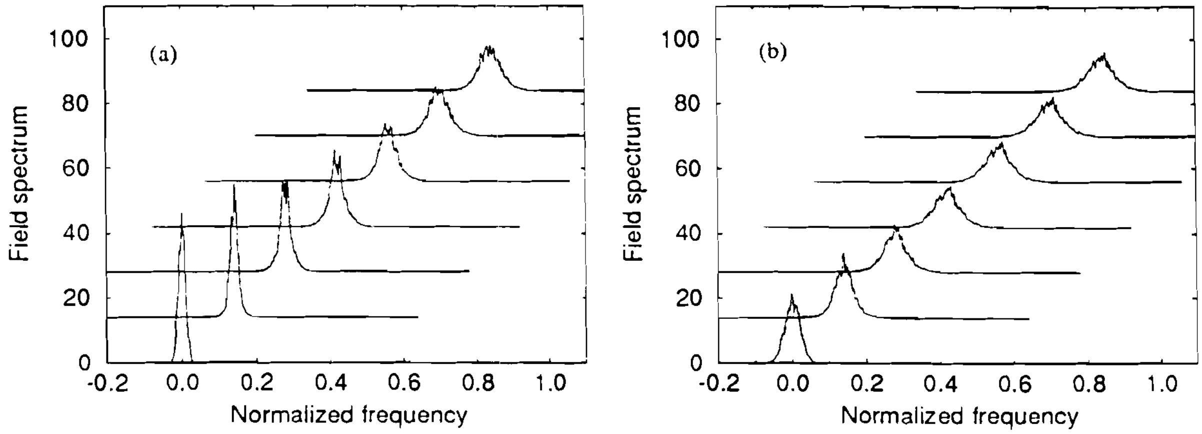

Figure 6-11: Spectral evolutions over 6 nonlinear lengths for two Gaussian processes with different input bandwidths. The dispersion is normal.

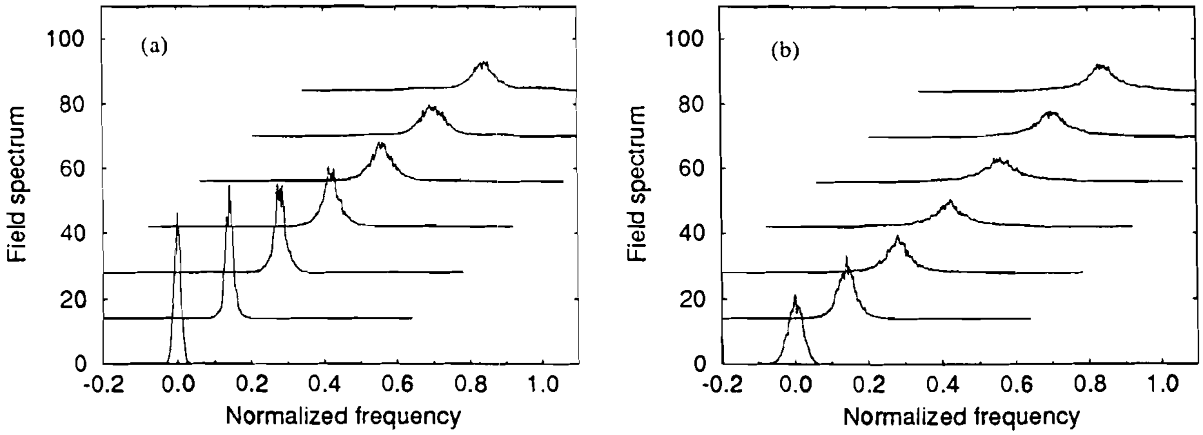

Figure 6-12: Same as Fig. 6-11 except that the dispersion is anomalous.

The numerical results for input Gaussian random processes are shown in Figs. 6-11 and 6-12 for the normal and anomalous dispersion regions, respectively. Two different vales of the FWHM of the initial Gaussian spectrum are considered. In all cases, the area of the spectrum is conserved as the wave propagates, as expected for a constant field intensity.

In both the normal (Fig. 6-11) and anomalous dispersion (Fig. 6-12) cases, the spectra broaden over several nonlinear lengths, and then tend to settle down. This is consistent with our parameter analysis. As the spectra broaden, the dispersion lengths get shorter while the nonlinear length is unchanged. This brings the weak turbulence region closer, where the evolution scale is much longer than the nonlinear length. The figures also show that broader initial spectra (b) reach the saturation stage faster, as expected. The spectral widths at satuation are less different in (a) and (b) than are the input spectral widths. This indicates that the asymptotic behavior of the spectral evolution for Gaussian input fields are determined primarily by the nonlinear dispersive nature of the medium, which is characterized by γP and β_2. The anomalous cases (Fig. 6-12) show more broadening due to the effect of MI. In fact, the feature of spectral wings of MI slightly shows up in the case of the narrow input spectral width [Fig. 6-12 (a)]. However, it is much less dramatic than in the case of a coherent pump with small additive noise.[54]

The corresponding results for input diffusing-phase processes are shown in Figs. 6-13 and 6-14, for the normal and anomalous dispersion regions, and for smaller (a) and larger (b) FWHM at the input, respectively. In contrast to the Gaussian process, the spectra in the normal dispersion cases do not broaden, but narrow slightly as the waves propagate. This is partly due to the fact that phase noise is less effective than the amplitude noise in terms of nonlinear spectrum broadening

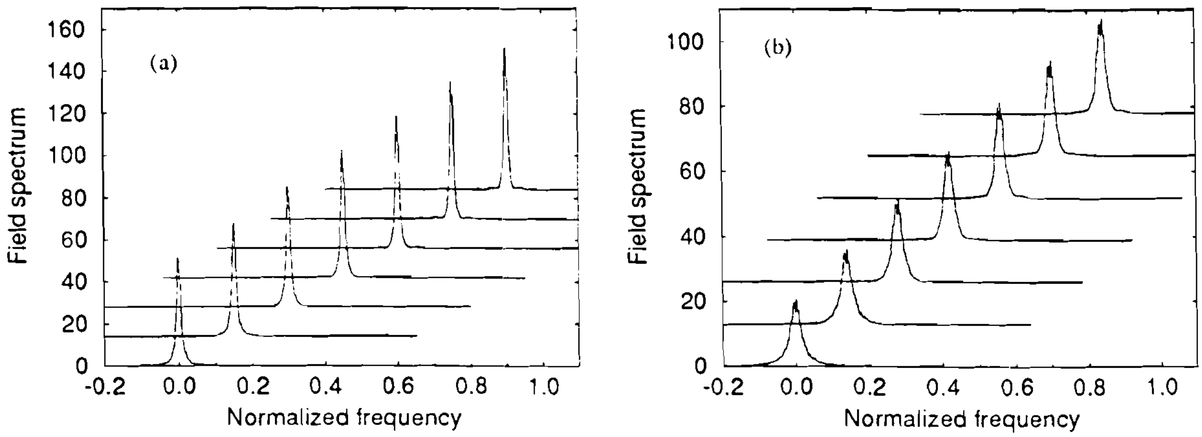

Figure 6-13: Spectral evolutions over 6 nonlinear lengths for two diffusing-phase processes with different bandwidths at the input. The dispersion is normal.

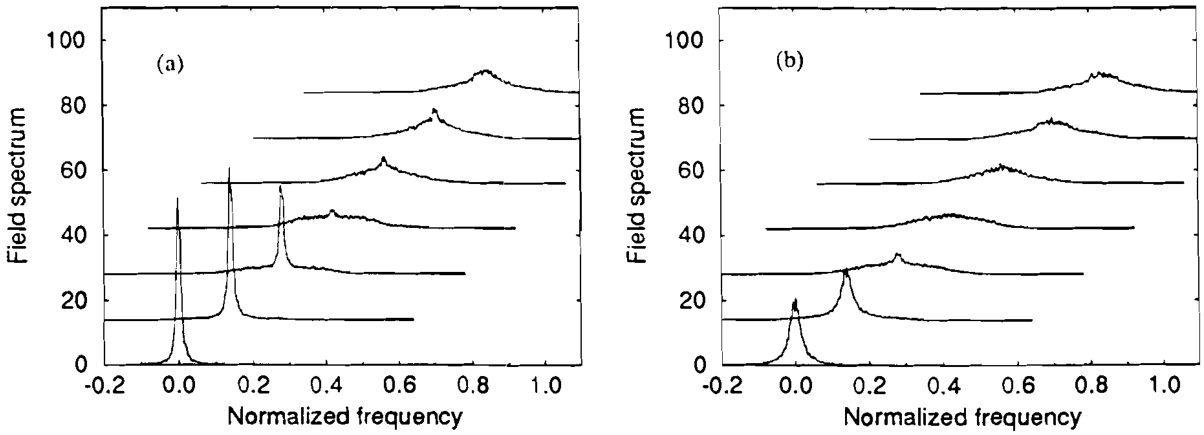

Figure 6-14: Same as Fig. 6-13 except that the dispersion is anomalous.

since the Kerr nonlinearity is only intensity dependent. The slight narrowing may be attributed to the fact that FWM interactions of the spectral components are nearly phase-matched around only the zero frequency and produce destructive interference for other frequencies during propagation over a long distance.[54]

In the anomalous dispersion cases (Fig. 6-14), the spectra still broaden due to the effect of MI, and the wider spectrum [Fig. 6-14 (b)] leads faster to a satuation of the broadening. As in the case of an input Gaussian process, the spectral wing feature of MI is more evident for a narrower input spectrum [Fig. 6-14 (a)], and is much weaker than in the case of a coherent pump. The broadenings are saturated later with spectral width less different in Fig. 6-14 (a) and (b) than they are initially. The implication of this behavior is similar to that given above for Gaussian input fields.

6.4 Conclusions

In this chapter, stochastic aspects of nonlinear dispersive wave propagation were investigated by studying the cases of small-amplitude noise and large-amplitude noise.

For small-amplitude noise, the pump effects on the propagation of a stochastic field in a nonlinear dispersive medium were studied both analytically and numerically. Simple expressions were obtained for the evolution of the power spectrum and the RIN as the propagation distance changes. It was found that in the case of anomalous GVD, MI plays a dominant role at large distances, as expected, where both the power spectrum and the RIN grow exponentially according to the MI gain to achieve symmetric patterns about the pump frequency. Even for normal GVD, the FWM effects are not negligible. Each sideband generates another sideband at the FWM frequency, thus establishing correlations between frequencies symmetrically located about the pump frequency. This causes oscillations of the power spectrum (and the quadratic growth near the pump frequency) and the RIN with propagation distance. Since the oscillations are frequency dependent, fringe formations are found on the power spectrum and the RIN. The results were applied to the case of a symmetric input-spectrum, which corresponds to laser intensity noise, and to the case of an asymmetric input-spectrum, which corresponds to the FWM of a broad-band probe in the presence of a CW pump.

For large-amplitude noise, we studied the spectral transformation of stationary noise propagaing through a nonlinear dispersiove medium. The parameter regions were characterized by comparing the dispersion lenth L_D, which usually changes during propagation, and the nonlinear length L_N, which is constant during propagation. For $L_D \ll L_N$, weak-turbulence theory can be applied and predicts a spectral broadening scale of L_N^2/L_D, which is much longer than the nonlinear length. In strong turbulence case, numerical simulations were carried out in both the normal and anomalous dispersion regions for input Gaussian processes, which correspond to thermal fields, and for diffusing-phase processes, which correspond to laser fields. Due to the effect of MI in the anomalous dispersion region, spectral broadening happens quickly (over two or three nonlinear lengths for the chosen parameters) and then slows down as the weak turbulence region approaches. The initial spectral width determines how fast the satuation happens but has less effect on the value of the satuated spectral width. The spectral-wing feature of MI is more evident for narrow initial spectral widths and is much weaker than in the case of a coherent pump. In the normal dispersion region, the spectrum broadens and evolves towards the weak turbulence region (as in the anomalous region) if the input process is Gaussian. However, for an input difusing-phase process, the spectrum narrows slightly during the propagation. This indicates that different roles are played by phase noise and amplitude noise in the spectral evolution of a wave propagating in a Kerr medium.

Bibliography

[1] A. K. Gailitis, *Izv. Akad. Nauk Latv. SSR* **4**, 13 (1965).

[2] M. J. Lighthill, *J. Inst. Math. Appl.* **1**, 269 (1965).

[3] V. I. Bespalov and V. I. Talanov, *Sov. Phys. JETP Lett.* **3**, 307 (1966).

[4] R. Y. Chiao, P. L. Kelley and E. M. Garmire, *Phys. Rev. Lett.* **17**, 1158 (1966).

[5] L. A. Ostrovskii, *Sov. Phys. JETP* **24**, 797 (1967).

[6] G. B. Whitham, *J. Fluid. Mech.* **27**, 399 (1967).

[7] T. B. Benjamin and J. E. Feir, *J. Fluid. Mech.* **27**, 417 (1967).

[8] A. G. Litvak and V. I. Talanov, *Radiophys. Quantum Electron.* **10**, 296 (1967).

[9] C. J. McKinstrie and G. G. Luther, *Phys. Scr.* **T-30**, 31 (1990). This paper contains a bibliography of early work on coupled modulational instabilities, to which should be added G. J. Roskes, *Stud. Appl. Math.* **55**, 231–238 (1976).

[10] C. E. Max, in *Intéractions Laser-Matière*, edited by R. Balian and J. C. Adam (North-Holland, Amsterdam, 1982), p. 305.

[11] R. W. Boyd, *Nonlinear Optics* (Academic, San Diego, 1992).

[12] G. P. Agrawal, *Nonlinear Fiber Optics*, 2nd ed. (Academic, San Diego, 1995).

[13] R. A. Fisher, editor, *Optical Phase Conjugation* (Academic, San Diego, 1983).

[14] B. Ya. Zel'dovich, N. F. Pilipesky and V. V. Shkunov, *Principles of Optical Phase Conjugation* (Spring-Verlag, Berlin, 1985).

[15] G. P. Agrawal, *Fiber-Optic Communication Systems* (Wiley, New York, 1992).

[16] S. Ryu, *Electron. Lett.* **28**, 2212 (1992).

[17] K. Kikuchi, *IEEE Photon. Tech. Lett.* **5**, 221 (1993).

[18] M. N. Islam, S. P. Dijaili and J. P. Gordon, *Opt. Lett.* **13**, 518 (1988).

[19] S. Trillo and S. Wabnitz, *Opt. Lett.* **16**, 1567 (1991).

[20] E. J. Greer, D. M. Patrick, P. G. J. Wigley and J. R. Taylor, *Opt. Lett.* **15**, 851 (1990).

[21] A. S. Gouveia-Neto, *J. Lightwave Technol.* **10**, 1536 (1992).

[22] M. Nakazawa, K. Suzuki, and H. A. Haus, *IEEE J. Quantum Electron.* **25** 2036 (1989).

[23] M. Nakazawa, K. Suzuki, H. Kubota, and H. A. Haus, *IEEE J. Quantum Electron.* **25** 2045 (1989).

[24] M. Haelterman, S. Trillo, and S. Wabnitz, *Opt. Commun.* **91**, 401 (1992).

[25] M. Haelterman, S. Trillo, and S. Wabnitz, *Opt. Lett.* **17**, 745 (1992).

[26] A. Hasegawa, *Optical Solitons in Fibers*, 2nd ed. (Springer-Verlag, New York, 1990)

[27] B. B. Kadomtsev and V. I. Karpman. *Sov. Phys. Usp.* **14**, 40 (1971).

[28] G. B. Whitham. *Linear and Nonlinear Waves* (Wiley, New York. 1974).

[29] R. J. Briggs. *Electron-Stream Interaction with Plasmas*. (MIT Press. Cambridge. MA. 1964), Chap. 2.

[30] E. M. Lifshitz and L. P. Pitaevskii. *Physical Kinetics* (Oxford, New York, 1981). p. 265.

[31] A. Bers. in *Handbook of Plasma Physics*. edited by M. N. Rosenbluth and R. Z. Sagdeev. *Volume 1: Basic Plasma Physics*, edited by A. A. Galeev and R. N. Sudan (North-Holland, Amsterdam, 1983), p. 451.

[32] P. Huerre, in *Instabilities and Nonequilibrium Structures*, edited by E. Tirapegui and K. Villarroel (Reidel, New York, 1987), p. 141.

[33] M. Yu and C. J. McKinstrie, *Phys. Rev. E* **52**, October issue, (1995)

[34] S. B. Cavalcanti, J. C. Cressoni. H. R. da Cruz, and A. S. Gouveia-Neto, *Phys. Rev. A* **43**, 6161 (1991).

[35] I. M. Uzunov, *Opt. Quantum Electron.* **22**, 529 (1990).

[36] C. J. McKinstrie, private communication (1993).

[37] E. A. Golovchenko and A. N. Pilipetskii, *J. Opt. Soc. Am. B* **11**, 92 (1994).

[38] M. Nakazawa, K. Suzuki, and H. A. Haus, *Phys. Rev. A* **38**, 5193 (1988).

[39] M. Yu, C. J. McKinstrie and G. P. Agrawal, *Phys. Rev. E* **52**, 1072 (1995).

[40] V. A. Bhagavatula, M. S. Spotz, W. F. Love, and D. B. Keck, *Electron. Lett.* **19**, 317 (1983).

[41] C. J. McKinstrie and R.Bingham, *Phys. Fluids B* 1, 230 (1989); **2**, 3215 (1990).

[42] G. P. Agrawal, *Phys. Rev. Lett.* **59**, 880 (1987).

[43] J. E. Rothenberg, *Phys. Rev. Lett.* **64**, 813 (1990).

[44] G. P. Agrawal, *Phys. Rev. Lett.* **64**, 814 (1990).

[45] J. E. Rothenberg, *Phys. Rev. A* **42**, 682 (1990).

[46] V. E. Zakharov, *Sov. Phys. JETP* **24**, 740 (1967).

[47] V. E. Zakharov, *J. Appl. Mech. Tech. Phys.* **9**, 190–194 (1968).

[48] M. Yu, C. J. McKinstrie and G. P. Agrawal, *Phys. Rev. E* **48**, 2178 (1993).

[49] C. T. Law and A. E. Kaplan, *Opt. Lett.* **14**, 734 (1989).

[50] W. J. Firth and C. Penman, in the *OSA Proceedings on Nonlinear Dynamics in Optical Systems, Vol. 7*, edited by N. B. Abraham, E. M. Garmire and P. Mandel (Optical Society of America, Washington, 1991), p. 142.

[51] M. Yu, G. P. Agrawal and C. J. McKinstrie, submitted to *J. Opt. Soc. Am. B.*

[52] M. Yu, G. P. Agrawal and C. J. McKinstrie, submitted to *J. Opt. Soc. Am. B.*

[53] A. Yariv, *Optical Electronics*, 4th edition (Saunders, Chicago, 1991), p. 500.

[54] M. Yu, G. P. Agrawal and C. J. McKinstrie, *J. Opt. Soc. Am. B* **12**, 1126 (1995).

[55] S. B. Cavalcanti, G. P. Agrawal and M. Yu, *Phy. Rev. A*. **51**, 4086 (1995).

[56] J. T. Manassah, *Opt. Lett.* **16**, 1638 (1991).

[57] B. Gross and J. T. Manassah, *Opt. Lett.* **16**, 1835 (1991).

[58] H. C. Yuen and B. M. Lake, in *Advances in Applied Mechanics*, edited by C. S. Yih (Academic, New York, 1982), p. 180.

[59] S. A. Akhmanov, V. A. Vysloukh, and A. S. Chirkin, *Optics of Femtosecond Laser Pulses* (American Institute of Physics, New York, 1992), p. 123.

[60] A. Hasegawa, in *Plasma Instabilities and Nonlinear Effects* (Spring-Verlag, Berlin, 1975).

[61] A. H. Nayfeh, *Introduction to Perturbation Techniques* (Wiley, New York, 1981).

[62] C. J. McKinstrie, X. D. Cao, and J. S. Li, *J. Opt. Soc. Am. B* **10**, 1856 (1993) and references therein.

[63] C. J. McKinstrie and M. V. Goldman, *J. Opt. Soc. Am. B* **9**, 1778 (1992).

[64] Y. Inoue, *J. Phys. Soc. Japan* **43**, 243 (1977).

[65] D. Schadt and B. Jaskorzynska, *Electron. Lett.* **23**, 1091 (1987).

[66] G. G. Luther and C. J. McKinstrie, *J. Opt. Soc. Am. B* **7**, 1125 (1990).

[67] G. P. Agrawal, *J. Opt. Soc. Am. B* **7**, 1072 (1990).

[68] M. Kauranen, A. L. Gaeta and C. J. McKinstrie, *J. Opt. Soc. Am. B* **10**, 2298 (1993).

[69] W. J. Firth. *Opt. Commun.* **39**, 313 (1981).

[70] C. T. Law and A. E. Kaplan. *J. Opt. Soc. Am. B* **8**, 58 (1991).

[71] W. J. Firth and C. Paré, *Opt. Commun.* **94**, 183 (1992).

[72] K. Ikeda. *Opt. Commun.* **30**, 257 (1979).

[73] R. Vallée. *Opt. Commun.* **81**, 119 (1991).

[74] R. Vallée. *Opt. Commun.* **93**, 389 (1992).

[75] M. B. van der Mark, J. M. Schins, and A. Langendijk, *Opt. Commun.* **98**, 120 (1993).

[76] G. Steinmeyer, D. Jaspert, and F. Mitschke, *Opt. Commun.* **104**, 379 (1994).

[77] D. W. McLaughlin, J. V. Moloney, and A. C. Newell, *Phys. Rev. Lett.* **54**, 681 (1985).

[78] M. Haelterman, *Opt. Lett.* **17**, 792 (1992).

[79] Y. R. Shen, *The Principles of Nonlinear Optics*, (Wiley, New York, 1984), Chap. 9.

[80] H. M. Gibbs, *Optical Bistability: Controlling Light with Light* (Academic, Orlando, 1985).

[81] M. T. de Araujo, H. R. da Cruz, and A. S. Gouviea-Neto, *J. Opt. Soc. Am. B* **8**, 2094 (1991).

[82] J. N. Elgin, *Opt. Lett.* **18**, 10 (1992).

[83] J. W. Goodman, *Statistical Optics* (Wiley, New York, 1985).

[84] N. Wax, ed., *Noise and Stochastic Processes* (Dover, New York, 1954).

[85] M. J. Potasek and B. Yurke, *Phys. Rev. A* **35**, 3974 (1987).

[86] S. J. Carter, P. D. Drummond, M. D. Reid, and R. M. Shelby, *Phys. Rev. Lett.* **58**, 1841 (1987).

[87] H. A. Haus and Y. Lai, *J. Opt. Soc. Am. B* **7**, 386 (1990).

[88] A. H. Gnauck, R. M. Jopson, and R. M. Derosier, *IEEE Photon. Technol. Lett.* **5**, 104 (1993).

[89] K. Kikuchi, *IEEE Photon. Technol. Lett.* **6**, 104 (1994).

[90] M. Yu, G. P. Agrawal and C. J. McKinstrie, *IEEE Photon. Technol. Lett.* **7**, 932 (1995).

[91] H. A. Haus, *J. Opt. Soc. Am. B* **8**, 1122 (1991).

[92] Y. S. Kivshar and B. Malomed, *Rev. Mod. Phys.* **61**, 763 (1989).

[93] A. Mecozzi, *J. Opt. Soc. Am. B* **11**, 462 (1994).

[94] R. Beach and S. R. Hartmann, *Phys. Rev. Lett.* **53**, 663 (1984).

[95] K. Hasselmann, *J. Fluid Mech.* **12**, 481 (1962) and **15**, 273 (1963).

[96] D. J. Benney and P. G. Saffman, *Proc. R. Soc. London, Ser. A* **289**, 309 (1966).